THE CATHOLIC UNIVERSITY OF AMERICA

Nanoscale Device Properties of Tellurium-based Chalcogenide Compounds

A DISSERTATION

Submitted to the Faculty of the

Department of Physics

School of Arts and Sciences

Of The Catholic University of America

In Partial Fulfillment of the Requirements

For the Degree

Doctor of Philosophy

By

Bishnu R. Dahal

Washington, D. C.

2017

Nanoscale Device Properties of Tellurium-based Chalcogenide Compounds

Bishnu R. Dahal, Ph.D.

Director: Dr. John Philip

The great progress achieved in miniaturization of microelectronic devices has now reached a distinct bottleneck, as devices are starting to approach the fundamental fabrication and performance limit. Even if a major breakthrough is made in the fabrication process, these scaled down electronic devices will not function properly since the quantum effects can no longer be neglected in the nanoscale regime. Advances in nanotechnology and new materials are driving novel technologies for future device applications. Current microelectronic devices have the smallest feature size, around 10 nm, and the industry is planning to switch away from silicon technology in the near future. The new technology will be fundamentally different. There are several leading technologies based on spintronics, tunneling transistors, and the newly discovered 2-dimensional material systems. All of these technologies are at the research level, and are far from ready for use in making devices in large volumes. This dissertation will focus on a very promising material system, Te-based chalcogenides, which have potential applications in spintronics, thermoelectricity and topological insulators that can lead to low-power-consumption electronics.

Very recently it was predicted and experimentally observed that the spin-orbit interaction in certain materials can lead to a new electronic state called topological insulating phase. The topological insulator, like an ordinary insulator, has a bulk energy gap separating the highest occupied electronic band from the lowest empty band. However, the surface states in the case of a three-dimensional or edge states in a two-dimensional topological insulator allow electrons to conduct

at the surface, due to the topological character of the bulk wavefunctions. These conducting states are protected by time-reversal symmetry, and cannot be eliminated by defects or chemical passivation. The edge/surface states satisfy Dirac dispersion relations, and hence the physics of relativistic Dirac fermions becomes relevant. This results in peculiar quantum oscillations in transport measurements which make it possible to unambiguously identify surface Dirac fermions. In order to lead us towards a better understanding of topological insulators and their applications, it is, however, necessary to develop techniques that will enable high quality materials to be obtained in a routine and reliable way. However, this has been an enormous challenge so far. Since highly volatile components are involved in most topological insulators, whether in bulk single crystal or epitaxial thin films or chemical vapor deposition grown nanoribbons, maintaining near stoichiometry has proven to be very difficult. Observing the predicted transport properties of these systems, particularly surface carriers of high mobility whilst maintaining bulk insulating states, is seriously impeded by the unintentional doping of bulk carriers. Moreover, in thin films and hetrostructures, at the all-important thickness range of a few nanometers, the additional limitation of the film-substrate lattice mismatch and the resulting strain in films is a major concern. In this thesis, we have developed a synthesis technique to obtain high quality SnTe nanoribbons, which is a topological crystalline insulator and its surface states are topologically protected by mirror symmetry of the lattice. The obtained ribbons are nearly stoichiometric and show strong semiconducting behavior with a bandgap of 240 meV. This is the first time high quality SnTe nanoribbons have been synthesized. High quality SnTe nanoribbons form a potential platform to understand the magnetic topological insulating behavior. In this thesis, it is also shown that magnetic behavior can be introduced in SnTe nanoribbons by means of chromium doping. Magnetically doped topological insulators, possessing an energy gap created at the Dirac point are

predicted to exhibit exotic phenomena including the quantized anomalous Hall Effect and a dissipationless transport, which facilitate the development of low-power-consumption devices using electron spins. In addition, this thesis also discusses the growth and transport properties of another Te-based chalcogenide system, CoTe with ferrimagnetic and semiconducting behavior. We have shown that the structural, electrical and magnetic properties can be tuned by controlling the amount of cobalt in the system.

The Dissertation by Bishnu R. Dahal fulfill the dissertation the requirement for the doctoral degree in physics approved by John Philip, PhD, as a director, Ian L. Pegg, PhD, and Biprodas Dutta, PhD, as Readers.

_____
John Philip, PhD, Director

_____
Ian L. Pegg, PhD, Reader

_____
Biprodas Dutta, PhD, Reader

DEDICATON

I dedicate my dissertation work to my mother Ambika Dahal, my late father Khet Raj Dahal, my wife Barsha Dhakal and my little son Ozas R. Dahal

Table of Contents

List of Figures

Acknowledgements

I wish to thank my advisor Dr. John Philip who was very helpful in guiding my research work and supporting me for over the years. I am very thankful to him for his contribution of precious time and expertise during my research.

Many thanks to Prof. Ian L. Pegg and Prof. Biprodas Dutta for all of their guidance through the process. Their feedback, ideas and discussions have been absolutely invaluable to me.

I am thankful to Dr. Sen. Nieh and Dr. Otto Wilson being on my Ph.D. Committee and assisting through the process.

I would like to thank my fellow graduate students, post-doctoral fellows. I am grateful to all of you.

I acknowledge The Vitreous State Laboratory which provided the research facilities and the staff's for their technical support.

I am thankful to the Physics Department, Faculty and staff for their supports and guidance.

I am especially thankful to The Vitreous State Laboratory for the financial support.

Chapter 1: Introduction

1.1 Nanotechnology

Nanotechnology is one of the fastest growing technologies among science and engineering. Foundational to nanotechnology are nanoscale structures, which are about 1 to 100 nanometers in size. Nanoscale structures include (Zero dimensional-0D) nanodots, nanoparticles, (one dimensional-1D) nanowires, nanotubes, nanoribbons and (two dimensional-2D) nanostructured thin films. Compared to bulk compounds, nanostructures have greatly reduced size, higher surface-to-volume ratio, and even demonstrate totally different properties because of quantum confinement. Artificially created nanostructures are the building blocks for the growing nanotechnology industries. These industries produce consumer goods used in our daily life which often go unnoticed. For example, because of nanotechnology, sunscreen is more radiation resistant, cell phone screens are more lightweight, clothing is more stain repellant, synthetic bones are stronger, sports balls are more durable.

Nanotechnology was born with a talk entitled **"There's Plenty of Room at the Bottom"** given by American physicists **Richard Feynman** at an American Physical Society meeting at California Institute of technology on December 29, 1959 [1]. Feynman explained a process in which scientists would be able to manipulate and control individual atoms and molecules. However, Feynman never explicitly used the term "nanotechnology". It was Professor **Norio Taniguchi** who coined the term nanotechnology, in his explorations of ultraprecision machining. Feynman's idea inspired other physicists to put these concepts into action, including **Eric Drexler**. In 1981, Drexler published an article entitled "**Molecular engineering: An approach to the developme**

of general capabilities for molecular manipulations." This publication integrated Feynman's concepts to the modern scientific ideas to explain the idea of molecular manufacturing [2]. It was not until 1981 that nanoscale structures were directly observed, with the invention of Scanning Tunneling Microscope (STM) by Binning and Roher [3].

Although nanotechnology is very young as a scientific discipline, some parts of nanotechnology has a long history. For example, nanoparticles are not the discovery of the modern science, but they were used by artisans in the ninth century in Mesopotamia to add a glittering effect on the surface of pots [3], [4], [5]. The first work on the thinfilms began at the end of the 19th century. Unusual properties of deposits on the walls of glass discharge tubes raised the interest of researchers to analyze the optical and electrical properties of these deposits [6]. The discovery of nanowires and nanotubes is relatively recent compared to nanoparticles and thinfilms. The first report of 1D nanostructures came in 1993 from Ijima *et. al* and ,Bethune *et. al* who found the structures on carbon nanotubes [7], [8]. The first reported nanowires were found in 1990 by Knoelder [9].

1.1.1 Growth of Nanostructures

Although nanostructures are already being utilized at the industrial level to make daily life goods, synthesis and growth control of nanostructures, especially nanowire, nanotube and nanoribbons is still not a trivial job. There are many different synthesis methods used by the research and industrial communities for growing nanostructures. All synthesis techniques can be categorized into two classes: bottom-up and top-down techniques.

1.1.2 Bottom-up Techniques

Bottom-up techniques combine the miniaturization of material components at the atomic level with a further self- assembly process, which leads to the formation of varieties of nanostructures. Physical forces operating at nanoscale are used during the self-assembly to combine basic units into a stable structure. Bottom-up approach methods are cost effective for the nanostructure synthesis. Some of the most common of these bottom-up methods include:

- Hydrothermal & Solvothermal
- Wet- chemical
- Electrospinning
- Molecular beam epitaxy (MBE)
- Chemical Vapor Deposition (CVD)

Hydrothermal and Solvothermal are pure chemistry techniques in which desired solutions are treated at high temperature and pressure in an autoclave. These are mostly used for the synthesis of single crystalline nanowires and nanoparticles. If the treated solution is aqueous, then the synthesis technique is referred to as hydrothermal. For non-aqueous solutions, the synthesis

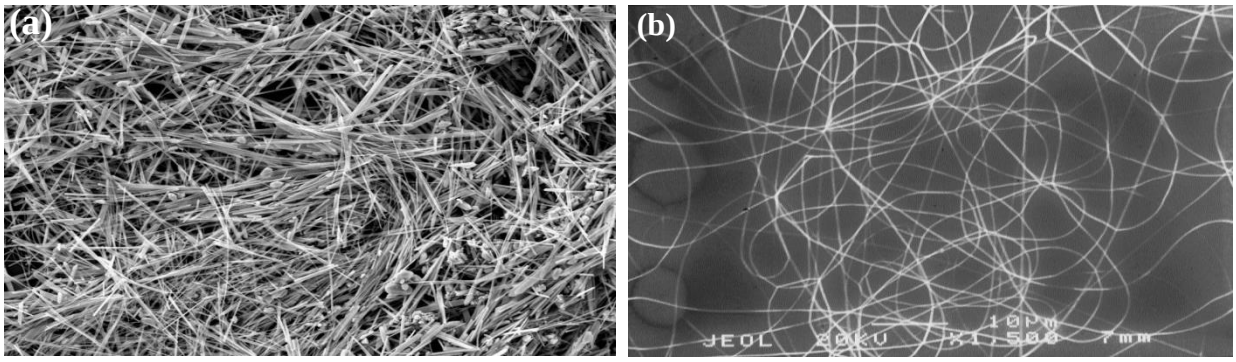

Figure 1.1: SEM image of high quality nanostructures synthesized using bottom-up technique: (a) nanoribbons by solvothermal (b) nanowires by electrospinning.

technique is referred as solvothermal. **Wet- Chemical** is also a pure chemistry technique used for the synthesis of nanostructures at relatively low temperature. Unlike hydrothermal or solvothermal, Wet-chemical synthesis techniques can be performed at low temperature and pressure, and do not require an autoclave. **The electrospinning** technique is useful to grow only nanowires. In this method, viscous aqueous solutions are created by combining different metal salts with polymers like Polyvinyl alcohol (PVA) and Polyvinylpyrrolidone (PVP). Drops of the solution are subjected to a high electric field, which creates micro/nanofibers. These micro/nanofibers need further heat treatment to form nanowires. Electrospinning is mostly used for the synthesis of inter-metallic and some metal-oxide nanowires. In **chemical vapor deposition**, the wafer (substrate) is exposed to one or more volatile precursors, which react and decompose on the substrate surface to produce desired nanostructures. High quality nanowires, nanoparticles and thin films can be synthesized using the CVD technique. Most of the semiconductor industries use CVD for nanostructure growth. **Molecular beam epitaxy** is a method only used to grow high quality thin films. It takes place in high or ultra-high vacuum (10^{-8} – 10^{-12} Torr). This technique was invented at Bell labs in the late 1960's by Arthur *et. al*. They built large structures by precise layers of atoms and molecules [10].

I have used a few bottom-up approaches mentioned above, which I will describe briefly in chapter 3.

1.1.3 Top-down Techniques

Top-down techniques use initial macroscopic structures which can be precisely controlled in processing nanostructures. There are several drawbacks as compared to bottom-up approach. Processings are much slower and much more expensive. These techniques require highly

sophisticated instruments, such as electron beam lithography, photolithography, atomic force microscopy (AFM) to break down the bulk samples into nanoscale structures. Most of the semiconductor industries use top-down lithography to manufacture computer chips and produce structures smaller than 100 nm.

1.2 Quantum size effects in nanostructures

The different physical properties of nanoscale sized compounds compared to the same material in bulk are caused part by the appearance of quantization effects, which arise due to the restrictions on the movement of electrons. This can lead to discrete energy levels, also known as quantization, depending on the size of the structures.

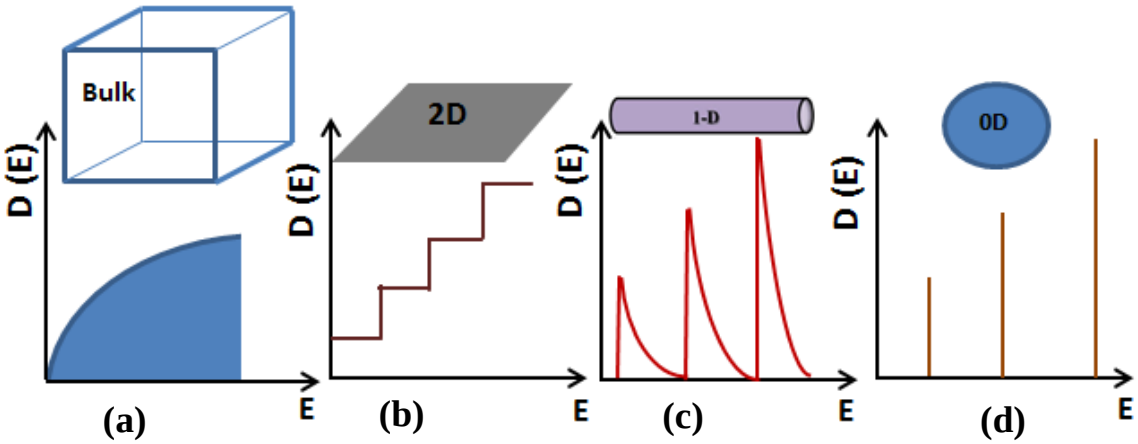

Figure1. 2: Density of states (a) 3D bulk system, (b) 2D nanostructure (thin films), (c) 1D nanostructure (nanowires), & (d) 0D nanostructure (nanoparticles).

These quantum effects lead to a different Density of States (DOS) (number of states per unit volume and energy) than that of the bulk material, which is described in the **figure 1.2**. In 0D nanostructures, the carriers are confined in all three directions, unlike in 1D and 2D nanostructures, where carriers can freely move in one and two dimensions respectively [11]. The

DOS is greatly modified for different types of nanostructures, depending upon the degrees of freedom as described in **figure 1.2**. For the bulk sample, DOS has a square root dependence on energy, and this dependence changes according to the dimensionality of the quantum structures, as shown in **figure 1.2 (a)**. The variation in DOS with dimensionality results in outstanding optical and electrical properties for realizing advanced nanodevices.

1.3 Nanomaterials

1.3.1 Chalcogenide Compounds

A Chalcogenide is a compound consisting of at least one chalcogen anion and one more electropositive element. Technically, all group 16 elements of the periodic table are defined as chalcogenides, but the term chalcogenides usually refer to tellurides, selenides and sulfides but not for oxides. Elements like Te, Se, S have lower electronegativity, and as a result, chalcogenide compounds are often semiconductors, which makes these compounds interesting for different applications. Some unique and prominent applications have been found from these materials.

My thesis will explain the transport properties of tellurium based chalcogenide nanostructures, which I will describe in detail in the corresponding chapters. Here, I am going to categorize the chalcogenide compounds based on their applications.

1.3.2 Applications

I. Spintronics

This field of electronics which does not only rely on charge of the electron, but also uses the spin of electrons is called **Spintronics**. Use of the spin provides additional functionalities with increased speed with low power consumption. The discovery of giant magnetoresistance (GMR) by Baibich *et. al* in 1980's is considered as a first step towards the development of Spintronics [12]. Tellurium based chalcogenide compounds exhibit large magnetoresistance effect.. Xu and his coworkers have shown the large magnetoresistance in Ag_2Te [13]. Zhang *et. al* have described the magnetoresistance in Bi_2Te_3 thin films [14]. The other spin-polarized compounds used in the fields of spintronics are PbTe, CoTe, SnTe, Sb_2Te_3, etc. This thesis will explain transport properties of Te based chalcogenide compounds useful for spintronics applications in chapter 5 and 6.

II. Thermoelectricity

Thermoelectricity is the direct conversion of heat into the electricity and vice versa. Thermoelectric devices create voltage from a temperature gradient and there is reverse effect as well. Thomas Johann Seebeck in 1821 found that a circuit made from two different metals, with the junctions at different temperatures would deflect a compass. He was initially convinced this was due to magnetism induced by temperature difference. However, he quickly realized that a "Thermoelectric Force" induced an electric current [15]. Bismuth Telluride (Bi_2Te_3), Antimony Telluride (Sb_2Te_3), and Lead Telluride (PbTe) are the most promising Te-based chalcogenide compounds used in the thermoelectric applications [16], [17].

III. Topological Insulator

Due to a better understanding of quantum physics, we now able to explain why some materials like diamond is a complete insulator, while the materials like graphite is highly conducting even though they are composed of the same element. In recent years, after a series of theoretical and experimental studies, physicists have realized that insulators can actually be divided into two classes. The first is the ordinary insulator like diamond which has a definite energy gap between the valence band and the conduction band. The second is the topological insulator, in which the energy gap between the conduction band and valence band is not like the ordinary insulator, but modified due to the strong spin-orbit interaction. In topological insulators, spin-orbit interaction is so high that the insulating energy gap is inverted. As a result, the state which has higher energy above the gap appears below. Hence, there is a highly conducting metallic surface state and an insulating state in the bulk. This phenomenon is not noticed in every insulator, but only observed in materials composed of heavy elements such as Bi or Sb. The concept of a topological insulator evolved at early eighties when Thouless and his coworkers predicted the current on the edge of the two dimensional materials in the presence of uniform magnetic field (commonly known as quantization of Hall conductance) [18]. The next study was carried out in 1995 by Gang at Massachusetts Institute of Technology about Fractional Quantum Hall (FQH) effect in liquids contain extremely rich internal structures which represented a whole new kind of ordering called "Topological Orders" [19]. Complete topological insulating behavior was theoretically predicted in HgTe sandwiched between CdTe in 2007 [20], [21]. Interestingly, most of the materials which have shown the topological insulating behaviors so far are chalcogenide type compounds. This thesis will explain the details of theoretical aspects of Topological Insulator in chapter 2.

1.4 Transport Properties of Nanostructures

Reduction of bulk materials into the nanoscale dimensions leads to a dramatic alteration of the overall behaviors of the materials. Physical properties of any material can be defined by some critical lengths, e.g., attenuation length and thermal diffusion length. What makes nanostructures more interesting than their bulk counterparts is their dimensions are smaller than a relevant critical lengths. Some of the critical lengths needed for the theoretical explanations of electrical and magneto-transport properties are described below.

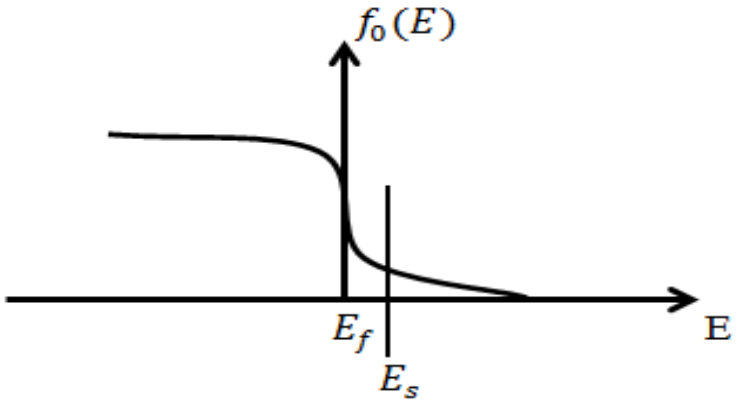

Figure1.3: Non-degenerate case, the Fermi function inside the band approximated by the equation 1.4.2 .

At equilibrium, the available states in a conductor are filled up according to Fermi function f_0 is defined as

$$f_0(E) = \frac{1}{1 + exp[\frac{\mathrm{E} - \mathrm{E_f}}{\mathrm{K_B T}}]} \qquad 1.4.1$$

Where, E_f is the Fermi energy.

There are two limits. One is the high temperature or non-degenerate limit

$(\frac{\exp[E-E_f]}{K_B T} >> 1)$ and equation (1.4.1) becomes

$$f_0(E) \approx \exp[-\frac{E - E_f}{K_B T}] \qquad 1.4.2$$

The other is the low temperature or the degenerate limit $(\frac{\exp[E_s - E_f]}{K_B T} <<< 1)$

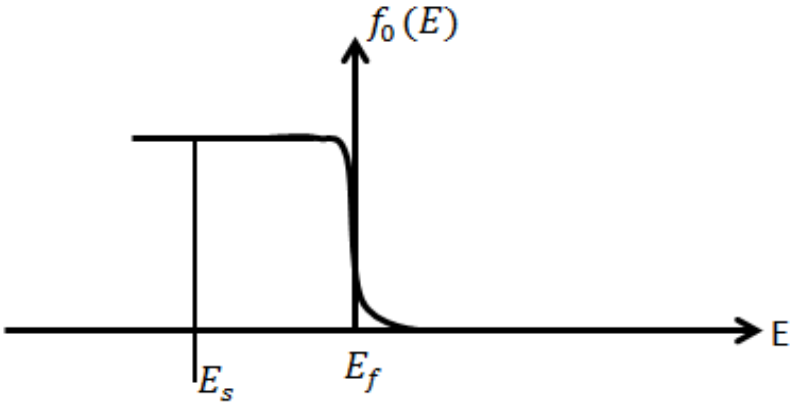

Figure 1.4: Degenerate case corresponding to the equation 1.4.3.

$$f_0(E) \approx \vartheta(E_f - E) \qquad 1.4.3$$

At low temperature the conductance is determined by electrons with energy close to the Fermi energy. The wave number of such electrons referred to the Fermi wavenumber (k_f):

$$E - E_f = \frac{\hbar^2 k_f^2}{2m} \Rightarrow \hbar k_f = \sqrt{2m(E - E_f)} \qquad 1.4.4$$

We can express the Fermi wavenumber in terms of the electron density:

$$k_f = \sqrt{2\pi n_s} \qquad 1.4.5$$

And the Fermi velocity is given by

$$v_f = \frac{\hbar k_f}{m} \qquad 1.4.6$$

1.4.1 Characteristic Lengths

A conductor generally shows ohmic nature if its characteristic lengths are much smaller than its dimensions. Some of the important characteristic lengths have been discussed below

- **de Broglie Wavelength(λ_d):** According to the equation 1.4.5, an electron with wavenumber k is related to de Broglie wavelength with the equation

$$\lambda_d = 2\pi/k = \sqrt{(2\pi/n_s)} \qquad 1.4.7$$

  For an electron density of $5x10^{11}/cm^2$, the Fermi wavelength is about 35 nm, and it is the de Broglie wavelength at the Fermi velocity. At the de Broglie wavelength scale, quantum mechanical phenomena are mostly effective.

- **Mean Free Path (L_m):** Average distance travelled by an electron before its momentum is destroyed by collision is defined as the electron's mean free path. The momentum relaxation time τ_m is related to the collision time τ_c by the expression

$$\frac{1}{\tau_m} \rightarrow \frac{1}{\tau_c}\alpha_m \qquad 1.4.8$$

  Here, α_m denotes the effectiveness and value lies between 0 and 1. For the smaller the value of α_m, electron will be scattered by small angles and there will be very

little momentum will be lost in an individual collision. Mean free path L_m is related to Fermi velocity by the equation

$$L_m = v_f \tau_m \quad (1.4.9)$$

The Fermi velocity is given by

$$v_f = \frac{\hbar k_f}{m} = \frac{\hbar}{m}\sqrt{(2\pi n_s)} \quad (1.4.10)$$

- **Phase - relaxation length (L_φ):** It is the average distance travelled by an electron before its intrinsic phase is lost is defined as phase-relaxation length. This is actually a quantum mechanical relaxation length which has no classical analog. Since electron moves diffusively, a proper way to estimate the relevant length L_φ is as follows:

$$L\varphi = \sqrt{D\tau_\varphi} \quad (1.4.11)$$

Here, τ_φ is the relaxation time during which an electron suffers many elastic collisions and $D = \left(\frac{1}{d}\right) vl$ is the diffusion constant (d is the dimensionality of the electron gas)

- **Spin Relaxation length (λ_s):** It is the average distance travelled by a particular spin within which spin alignments do not die and spin coherence is maintained. It is the distance where spin coherence remains only (1/e)th value of the maximum coherence.
- **Magnetic length (l_B)**: Magnetic length l_B has the physical meaning of the smallest size of a circular orbit in a magnetic field which will allow by the uncertainty principle. In the presence of magnetic induction B, electron energy is quantized in the integer

multiple of $\hbar w_c$, where w_c is the cyclotron frequency. Mathematically, magnetic length is expressed as,

$$l_B = \sqrt{(\frac{\hbar}{eB})} \qquad 1.4.12$$

1.5 Boltzmann Transport Equation

Electron transport through nanostructures can be understood by using Boltzmann Transport equation. In thermodynamic equilibrium, the probability of occupation of an energy level $E(k)$ is given by Fermi-Dirac distribution function

$$f_0(k) = \frac{1}{e^{\frac{[E(k)-\mu)]}{K_B T}+1}} \qquad 1.5.1$$

Here, T is the temperature; μ is the chemical potential & $f_0(k)$ is the shorthand notation for $f_0[E(k)]$.

When the external perturbations are applied; the electron distribution is disturbed from equilibrium Fermi-Dirac function. The distribution function $f(r,k,t)$ in addition to the k, depends on real space coordinate r, and on time t. $f(r,k,t)drdk\ /4\pi^3$ gives the number of electrons at time t, in the element of volume $drdk$ around the point (r,k) of the "Phase space"

According to the semi-classical model, an electron at the point (r,k) and time t evolves towards the point $(r+V_k dt, k+(F/\hbar)dt)$ at the time $t+dt$, where

$$V_k = \frac{1}{\hbar}\frac{\partial E(k)}{\partial k}, \qquad F = \frac{d<\hbar k>}{dt} \qquad 1.5.2$$

F, denotes the external force acting on the carriers.

Using the Liouville theorem, we can write the distribution function

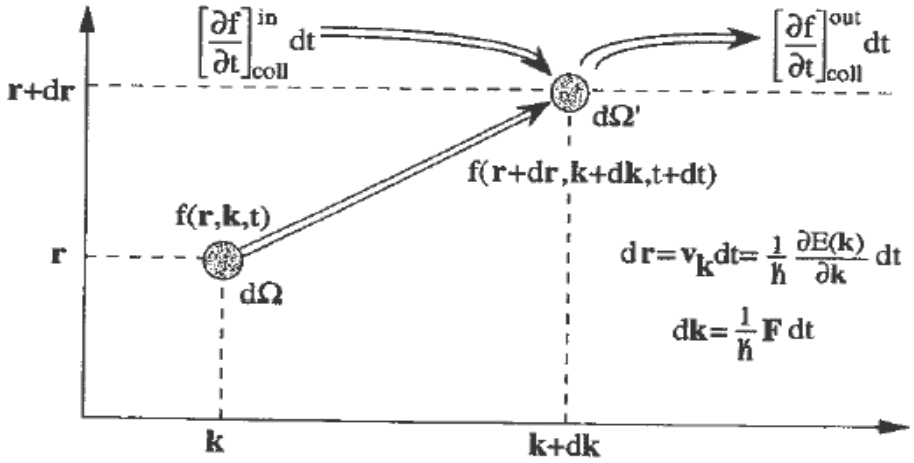

Figure 1.5: Schematic diagram of the conservation of electrons moving in the phase space r,k (Liouville theorem) [22].

$$f(r = Vdt, k + \frac{F}{\hbar}dt, t + dt \equiv f(r,k,t) + \left[\frac{\partial f}{\partial t}\right]_{coll} dt \qquad 1.5.3$$

Where, $\left[\frac{\partial f}{\partial t}\right]_{coll}$ is a net rate of charge due to the collision process in the phase volume $drdk$.

Using the Taylor series up to the first order on the left part of the equation (1.6.3), we will get the Boltzmann transport equation.

$$\frac{\partial f}{\partial r}.V + \frac{\partial f}{\partial k}.\frac{F}{\hbar} + \frac{\partial f}{\partial t} = \left[\frac{\partial f}{\partial t}\right]_{coll} dt \qquad 1.5.4$$

Using the relaxation approximation, equation 1.5.4 becomes

$$\frac{\partial f}{\partial r}.V + \frac{1}{\hbar}.F + \frac{\partial f}{\partial t} = \frac{f - f_0}{\tau} \qquad 1.5.5$$

where, f_0 is the thermal equilibrium distribution function and f is the non-equilibrium distribution function. Transport coefficients can be expressed in terms of current density and energy flux density with the general expression

$$J = \frac{1}{4\pi^3}\int (-e)V_k f dk \qquad 1.5.6$$

$$U = \frac{1}{4\pi^3}\int E_k V_k f dk \qquad 1.5.7$$

where, the factor $2/(2\pi)^3$ comes into the account due to the spin degeneracy and density of allowed points in k space.

The general expression for the current density in a metal in isothermal conditions, with non-uniform carrier concentration is expressed as

$$J = \sigma_0[E + \frac{1}{e}\nabla\mu] \qquad 1.5.8$$

With $\sigma_0 = \frac{ne^2\tau}{m^*}$ is the electrical conductivity, μ is the chemical potential, E is the electric field, n is the carrier concentrations and m^* is the effective mass

Equation 1.5.8 is equally analogous to spin transport phenomenon [23].

1.6 Magnetoresistance (Magnetotransport Properties)

Magnetoresistance (MR) is a change in the resistance of a device upon the application of magnetic fields consisting of metal or semiconducting materials. There are different factors contributing to the MR effect which can be divided into physical and geometric contributions. Physical conditions arise from the magnetic field dependence of carrier mobility, energy-band structure or spin-spin interactions. Giant magnetoresistance (GMR) and tunneling magnetoresistance (TMR) effects are

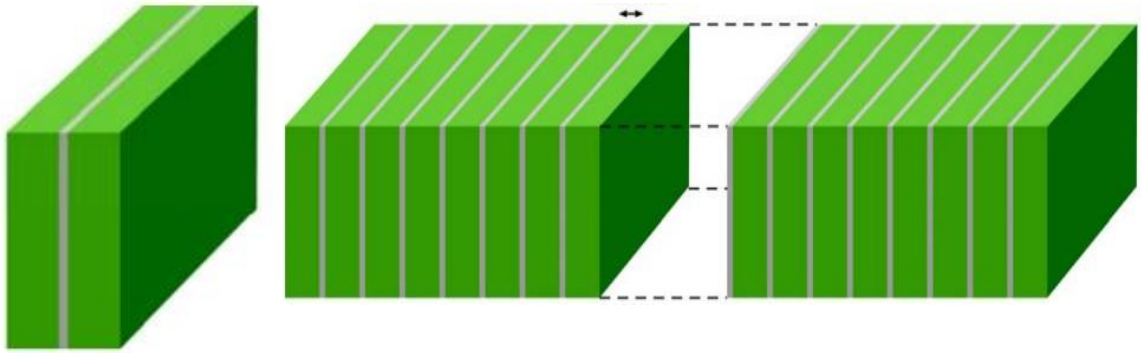

Figure 1.6: Nanometer thick layer of iron (green) and separated by nanometer thick layer of chromium (gray). The left figure illustrates the tri-layer of Fe/Cr/Fe and right figure illustrates the multilayers (Fe/Cr)n.

due to the physical contributions while the extraordinary magnetoresistance (EMR) is because of the geometric effect [23-27]. This thesis will describe the MR based on physical contributions (spin dependence).

For ferromagnetic materials like cobalt, nickel and iron MR will also depend upon the direction of the external applied magnetic field relative to the direction of the current through the magnet. Thomson measured resistance of Ni and Co in presence of magnetic field nearly 150 years ago[28]. He wrote "**I found that iron, when subjected to a magnetic force, acquires an increase of resistance to the conduction of electricity along, and a dimension of resistance to the conduction of electricity across, the lines of magnetization**" This difference in resistance between parallel and perpendicular case is called anisotropic magnetoresistance (AMR) [29-32].

The MR effect has a significant importance in technology. An alloy of iron and nickel $Fe_{20}Ni_{80}$ (permalloy) is the most useful material and is used for magnetic discs and sensors.

It was the year 1988. Two research groups independently discovered materials showing very high magnetoresistance, now known as Giant Magnetoresistance (GMR). They used magnetic

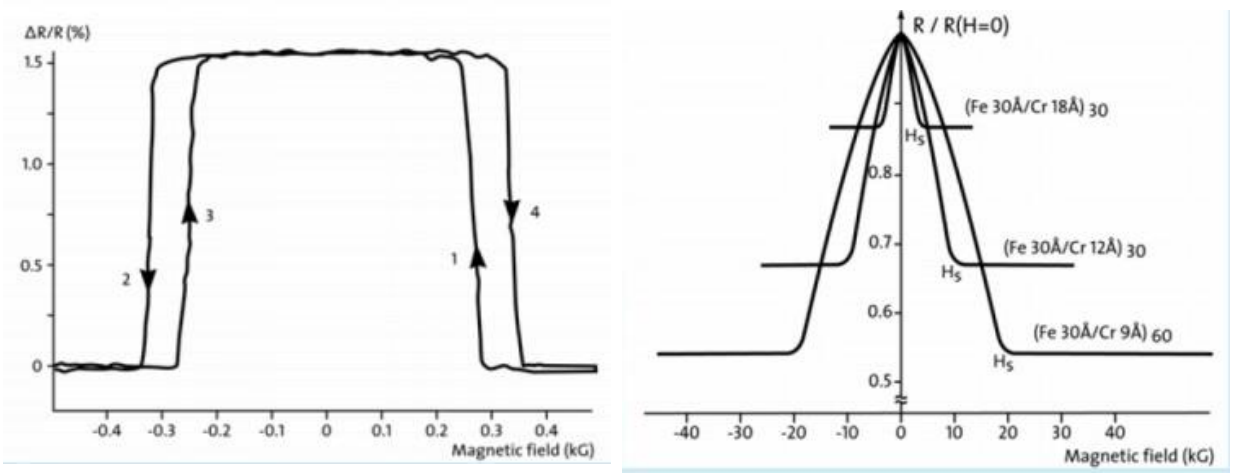

Figure 1 7: MR measurement for tri-layer Fe/Cr/Fe measured by the Grunberg's group at room temperature (left). MR measurement with a multilayers of Fe/Cr/Fe measured by the Fert's group at 4.2 K(right).

multilayers, where layers of ferromagnetic and non -magnetic metals are placed on each other as shown in **figure 1.6 .** The width of individual layers is nanometer thick (only a few atomic levels). The research group lead by Peter Grünberg used a tri-layer of Fe/Cr/Fe while the group lead by Albert Fert used multilayers of $(Fe/Cr)_n$ [24][25]. **Figure 1.6** is the cartoon of the experimental setup performed by the Grunberg group on the right and with those of Fert's group on the left. Both tri-layer and multilayer measurement showed significant results with negative magnetoresistance. The Fert's group observed as high as 50% decrease in resistance with the application of magnetic fields which is much higher than compared to Grunberg's group. The reason for the higher MR effect is not only because of multilayers but Fert's group performed the experiment at 4.2 K, while the Grunberg's group had done the measurement at room temperature. Their results have summarized in **figure 1.7**.

Magnetoresistance (MR) is a spin-dependent phenomenon and MR ratios are calculated by the expression

$$\frac{\Delta R}{R(0)} = \frac{[R(H=0) - R(H)]}{R(H=0)} \quad 1.6.1$$

Here, ΔR is a change in the resistance

MR ratios are equivalently calculated by resistivity ratios as expressed in the equation 1.6.2

$$\frac{\Delta \rho}{\rho(0)} = \frac{[\rho(H=0) - \rho(H)]}{\rho(H=0)} \quad 1.6.2$$

Here, $\Delta \rho$ is the change in resistivity

1.7 Outline

In this thesis, transport properties of different compounds of Te-based chalcogenide nanostructures have been covered in a systematic way.

Chapter 2 will discuss the basic introduction and application of topological insulator materials. The general discussion will follow the historical breakdown, direction of current research and potential applications based on topological insulating materials.

Chapter 3 will discuss experimental procedures and measurement techniques. The general discussion will follow the different techniques we have used for the synthesis of nanostructured materials and all characterization and measurement tools used for measurements.

Chapter 4 will discuss about nanoscale device fabrication techniques and transport property measurement tools. The general discussion will follow all the necessary steps in detail to make single nanostructure nanodevice by using e-beam lithography and measurement techniques we have adopted to analyze transport properties of the nanodevice.

Chapter 5 will discuss the transport based on nearly stoichiometric cobalt telluride CoTe. The general discussion will start from the synthesis and characterization of CoTe nanostructures. Characterization involves complete analyses of morphological, structural, magnetic and optical characterizations. Additionally, we will explain electrical and magneto-transport properties from single CoTe nanostructure nanodevice.

Chapter 6 will discuss the effects of excess Co present in CoTe nanostructures. The general discussion will start from the synthesis and characterization of $Co_{1+\delta}Te$ nanostructures. Characterization involves complete analyses of morphological, structural, magnetic characterizations. We will explain in detail how the excess Co will alter the crystal phase of the nanostructures. Additionally, we will explain electrical and magneto transport properties from single $Co_{1+\delta}Te$ nanostructure device fabricated using e-beam lithography.

Chapter 7 will discuss the characterization and transport properties of topological crystalline insulating tin telluride SnTe nanoribbons. The general discussion will start from the synthesis and characterization of SnTe nanoribbons. Characterization involves complete analysis of morphological and structural characterizations. Additionally, we will explain electrical transport properties form single SnTe nanoribbon field effect transistor FET.

Bibliography

[1] R.P. Feynman, There's Plenty of Room at the Bottom, American Physical Society Meeting, Caltech, December 1957

[2] K.E. Drexler, Molecular engineering: An approach to the development of general capabilities for molecular manipulation, Proceeding of the National Academy of Science USA Vol. 78, No. 9, PP. 5275-5278, September 1981

[3] Klaus D., Handbook Nanophysics: Nanoparticles and Quantum Dots, CRC Press, PP 2-1, ISBN 9781420075458

[4] D. Fanfair, S. Desai, and C. Kelty, The early history of nanotechnology, Connexions module: m14504

[5] Firdos Alam Khan, Biotechnology Fundamentals (2012), CRC Press, P 328, ISBN 9781439820094

[6] P. Drude, Elektronentheoric der Metalle, Ann. Der Physik, 37, 576 (1989)

[7] D. S. Bethune, C. H. Klang, M. S. De Vries, G. Gorman, R. Savoy, J. Vazquez, and R. Beyers, "Cobalt-catalysed growth of carbon nanotubes with single-atomic-layer walls," *Nature*, 1993

[8] S. Iijima and T. Ichihashi, "Single-shell carbon nanotubes of 1-nm diameter," *Nature*, 1993

[9] C. M. Knoedler, "Helium-ion damage and nanowire fabrication in GaAs/AlGaAs heterostructures," *J. Appl. Phys.*, vol. 68, no. 3, pp. 1129–1137, 1990

[10] A. Y. Cho, and J. R. Arthur, Molecualr Beam Epitaxy, progress in solid-state chemistry, vol. 10 part 3, pp 157-191, printed in Great Britain

[11] N.W. Ashcroft, N. D. Mermin, Solid State Physics, Holt Rinehartand Winston, Philadelphia (1976); M. S. Dresselhaus, G. Chen, M. Y. Tang, R. Yang, H. Lee, D. Wang, Z. Ren, J. P. Fleurial, and P. Gogna, New Directions for Low-Dimensional Thermoelectric Materials, Adv. Mater., 19, 1, (2007)

[12] M. N. Baibich, J. M. Broto, A. Fert, F. N. Van Dau, F. Petroff, L. De Physique, U. U. Paris-sud, and F.- Orsay, "Giant Magnetoresistance of (001)Fe/(001)Cr Magnetic Superlattices," *Phys. Rev. Lett.*, vol. 61, no. 21, pp. 2472–2475, Nov. 1988.

[13] S. X. Zhang, R. D. McDonald, A. Shekhter, Z. X. Li, Q. X. Jia, & S. T. Picraux, " Magntro-reisitance up to 60 Tesla in topological insulator Bi_2Te_3 thon films", Appl. Phys. Lett. 101, 202403, August 2012

[14] R. Xu., A. Husmann, T. F. Rosenbaum, M. –L. Saboungit, J. E. Enderby, & P. B. Littlewood, "large magnetoresistance in non- magnetic silver chalcogenides, Nature, Vol. 309, Nov 1997

[15] T.J. Seebeck "Magnetische Polarisation der Metalle und Erze Durch Temperatur-Differenz"1822-23 in Ostwald's Klassiker der Exakten Wissenshaften Nr. 70 (1895). Seebeck Biography 1. Seebeck Biography 2http://www.kirj.ee/public/Engineering/2007/issue_4/eng-2007-4-2.pdf

[16] X. Tang, W. Xie, H. Li, W. Zhao, Q. Zhang, "Preparation and thermoelectric transport properties of high-performance ptype Bi2Te3 with layered nanostructure", Appl. Phys. Lett. 90, 012102, Jan. 2007.

[17] X. Li, B. Zhang, T. M. Tritt, J. W. Kolis, A. Kumbhar, "Solution-Chemical Syntheses of Nano-Structured Bi_2Te_3 and PbTe Thermoelectric Materials" Journal of Electronic Materials, Vol. 36, no. 7, Jun. 2007

[18] D. J. Thouless, M. Kohmoto, M. P. Nightingle, and M. den Nijs, "Quantization Hall Conductance in a Two- Dimensional Periodic Potential", Physical Review Letters, Vol. 49, Number 6, August 1982.

[19] X. Gang, Topological Orders and edge excitations in fractional quantum hall states, Advances in physics, Volume 44, Issue 5, pp 405-473, October 1995

[20] L. Fu, C. L. Kane, and E. J. Male, "Topological Insulators in Three Dimensions", Physics Review Letters, Vol. 98, PP 106803, March 2007.

[21] J. E. Moore, and L. Balents, "Topological invariants of time-reversal –invariant band structures", Physical review B, Vol. 75 PP. 121306(R), March 2007

[22] G. Grosso and Giuseppee Pastori Parravicini, *Solid State Physics*, Second. Academic Press, 2003.

[23] J. Sun, and J. Kosel, "Extraordinary Magnetoresistance in Semiconductor/Metal Hybrids: A Review", Materials 2013, 6, 500-516.

[24] I. A. Cambell, and A. Fert, "Transport properties of ferromagnets" in ferromagnetic materials, ed. E.P. Wohlafarth, North-Holland, Amsterdam, Vol. 3, P. 747(1982).

[25] G. Binasch, P. Grunberg, F. Saurenbach, and W. Zinn, "Enhanced magnetoresistance in layered magnetic structure with antiferromagnetic interlayers exchange", Phys. Rev. B. 39, 4828 (1989)

[26] M. N. Baibich, J. M. Broto, A. Fert, F. Nguyen , van Dau, F. Petroff, P. Eitenne, G. Creuzet, A. Friederich, and J. Chazelas, "Gaint Magnetoresistance of (001)Fe/(001)Cr Magnetic sublattices, Phys. Rev. Lett. 61, 2472 (1988)

[27] T. R. McGuire, & R. I. Potter, Anisotropic Magnetoresistance in Ferromagnetic 3d Alloys, IEEE Transactions on Magnetics, Vol. MAG-11, no. 4, July 1975.

[28] W. Thomson, “On the electro-dynamic qualities of metals: Effects of magnetization on the electric conductivity of nickel and iron,” Proc. Roy. SOC., vol. 8, pp. 546-550,1857.

[29] L. Chang, M. Wang, L. Liu , S. Luo , P. Xiao, “A brief introduction to giant magnetoresistance” arXiv:1412.7691, Dec. 2014

[30] T. YuFeng, and Y. ShiShen, “Giant magnetoresistance: history, development and beyond”, Sci. China-Phys. Mech. Aston., vol 56, No. 1, Jan. 2013.

[31] M. McCormack, S. Jin, T. H. Tiefel, R. M. Fleming, and J. M. Phillips, and R. Ramesh “Very large magnetoresistance In perovskite-like La-Ca-Mn-O thin films” Appl. Phys. Lett. 64, May 1994.

Chapter 2: Topological Insulator

2.1 Introduction

2.1.1 Topology

Topology is a branch of mathematics concerned with geometric properties that are insensitive to smooth deformation. This is described in **figure 2.1.** A smooth sphere can be deformed into many shapes; such as the surface of a disc or a bowl, but a surface of a sphere cannot be smoothly deformed into a surface of a doughnut. A surface of a sphere and a surface of a doughnut are distinguished by an integer of topological invariant called genus g, which is essentially the number of holes. For a sphere g=0 while for a doughnut g=1. Surface with different g cannot be deformed into one another and called topologically distinct while the surfaces with same g are known to be topologically equivalent [1]. Gauss- Bonnet theorem, states that the integer of the Gaussian

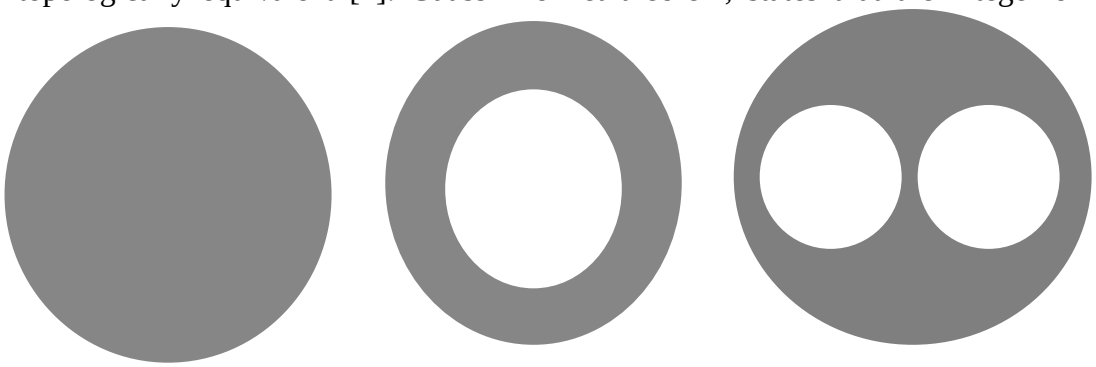

Figure 2. 1: Surface of sphere (g=0), doughnut (g=1) and surface with g=2.

curvature, K over a surface defines an integer topological invariant called the Euler characterization [2].

$$\chi(S) = \frac{1}{2\pi}\int_S KdA \qquad 2.1.1$$

For a sphere of radius R, χ =2, where $K = 1/R2$. Euler Characteristic is quantized and related to the genus by $\chi = 2 - 2g$.

2.1.2 Band Theory:

An insulator is a material that has an energy gap for electronic excitations, which separates the ground states form all excited states. Two insulators are topologically equivalent if one can be continuously changed into the other following the adiabatic transformation (*Adiabatic Transformation: Rapidly changing conditions or perturbations don't prevent the system from adopting its configuration, hence the probability density function is modified during the process)* such that the system always remains on the same ground state. In other words, insulators are topologically equivalent if there exists an adiabatic path connecting them along with the energy gap remains finite. For topologically inequivalent insulators, band gap vanishes during the phase transformation [1].

A topological insulator (TI) has an ordinary bulk energy gap separating the highest occupied electronic band from the lowest empty band; however, it has gapless surface states that are protected by time reversal symmetry (T-symmetry). (*T-symmetry; In condensed matter systems it is represented as a unitary matrix times complex conjugation. A simple system that follows T-symmetry would be a system described by a real Hamiltonian)* In simple words, it has electronically insulating bulk while conducting along the boundary (conducting edges in 2D materials and conducting surfaces on 3D materials). The existing metallic boundaries are very robust, since they are protected by time reversal symmetry.

2.2 Theoretical Background:

2.2.1 Quantum Hall Effect

Topological insulating phenomenon in condensed-matter physics is the consequence of the

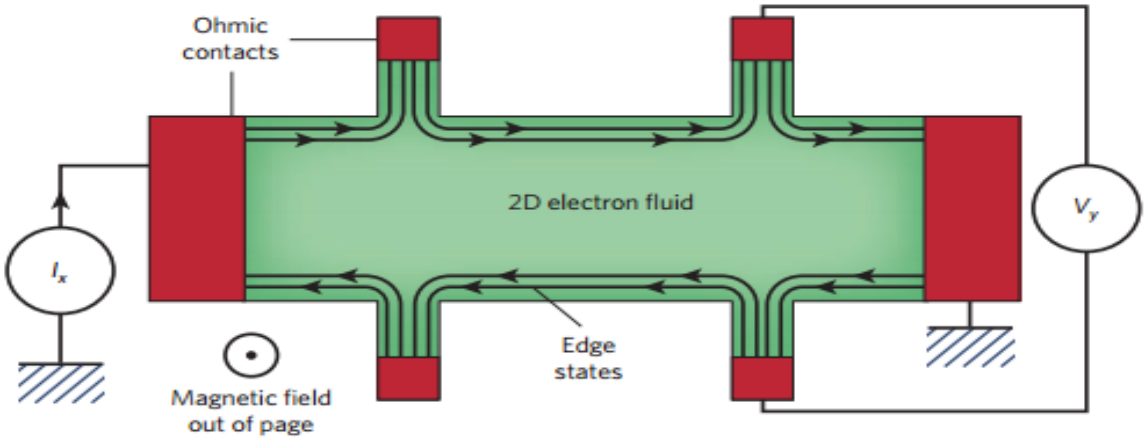

Figure 2. 3: Experimental set- up for measuring the Quantum Hall Effect [4].

Quantum Hall Effect (QHE). QHE phenomenon is the quantum version of Hall Effect, which describes the quantization of Hall conductance in 2-dimensional materials. Klitzing and his co-workers first experimentally observed QHE. The approach was based on the fact that degenerate electron gas in the inversion layer of a metal-oxide-semiconductor field effect transistor

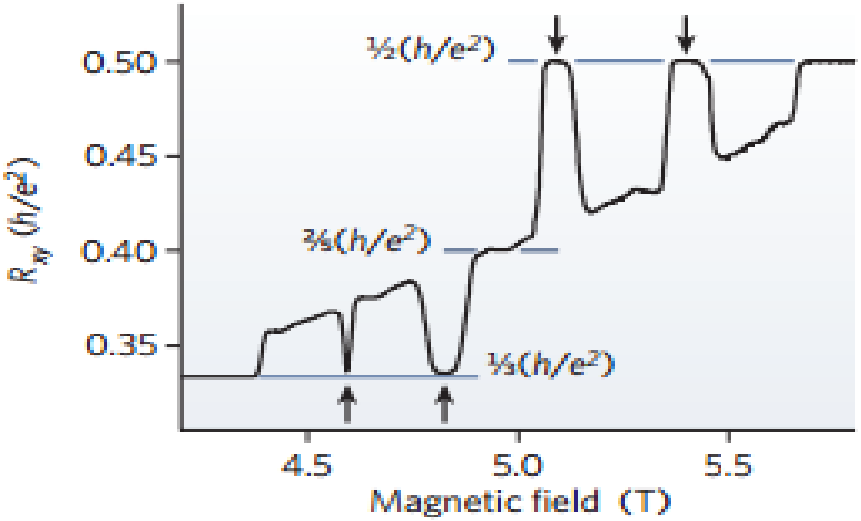

Figure 2. 2: Quantization of Hall Resistance.

(MOSFET) was fully quantized when the FET was operated at liquid helium temperature and in a strong magnetic field (15 T) [3]. They have shown experimentally, the Hall conductivity of an inversion layer is quantized to an integer multiple of (e^2/ħ). Experimental set-up for QHE in **figure 2.2** shows two dimensional electronic systems subject to strong magnetic field at liquid helium temperature. Hall resistance (The ratio of voltage V_y to the current I_x) is expressed as h/e^2v. Here,

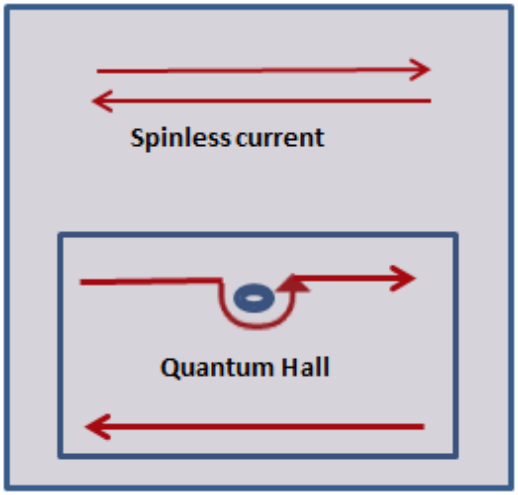

Figure 2.4: A spinless quantum Hall states. The upper edge contains only forward path while the lower edge follows the backward flow of electrons. For the presence of impurities, electron go around without having scattering [5].

$v = \frac{n\phi_0}{B}$ is a dimensionaless number with ϕ_0 is the flux and n is the electron density. The quantization of conductance or fractional QHE is summarized in **figure 2.3** . The quantum Hall state provided the first example of a quantum state that has no spontaneously broken symmetry. This behavior does not depend on its geometry but depends only on its topology. This is the reason that the discovery of QHE is considered as a birth of totally new state of topologically insulating systems. The quantum Hall effect occurs when a strong magnetic field is applied to a 2D gas of electrons in a semiconductor. At low temperature and high magnetic field, electrons flow only through the edge of the semiconducting material and counter flows of electrons are separated into different lanes located at the different edges of the material. When an electron strikes with the

impurities on its path, it will take a detour instead of striking back (**figure 2.4).** This is the reason, why the topological surface is robust. This dissipationless transport phenomenon is the most useful asset of quantum Hall states for nanoelectronics

2.2.2 Spin Quantum Hall Effect and Z_2 Phase

In regard to spin Hall Effect, generation of transverse spin current in response to the longitudinal electric filed was proposed theoretically in 1970s [6] but experimentally it was only verified in 2004 by Kato *et al.* [7]. Later it was verified that spin currents cannot produce in the absence of electrons at the Fermi level, but this idea leads to the proposals for the Quantum Spin Hall Effect (SQH) insulator by Kane and Male in 2005 followed by the independent proposal by Bernevig and Zhang [8,9,10]. The QSH insulator has two parts of QHE. First, the chiral edge state is spin polarized and then secondly, two states form a time reversal symmetry (TRS). Kane and Mele provide a graphene model to analyze the SQH without having the magnetic field. They explained, it is the spin-orbit-coupling (SOC) that plays the role of the magnetic field in SQH insulator. They further identified that QSH insulator is characterized by Z_2 index (Z_2 expresses whether the number of times the 1D edge state crosses the Fermi level between 0 and π/a, here a is the lattice constant). The SOC in graphene is very weak, which causes difficulty to detect an experimental QSH effect proposed by Kane et. al [11]. Hence, Bernevig, Hughes, and Zhang proposed topological insulating behavior in a 2D model of HgTe sandwiched between CdTe [12]. It was verified experimentally by Kong in 2007 and showed that the conductance, σ_{xx} to be quantized to

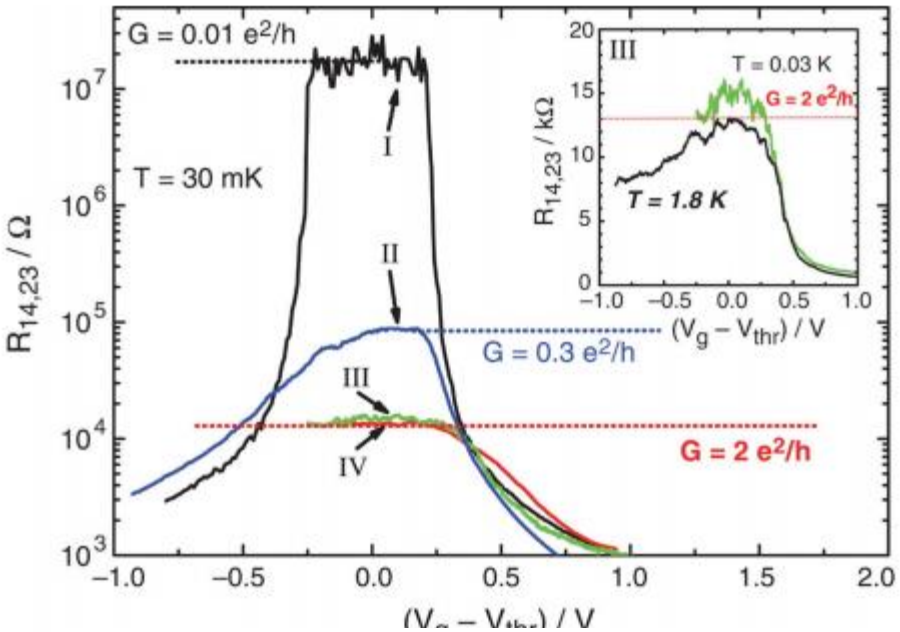

Figure 2.5: Four -terminal resistance of various CdTe/HgTe/CdTe quantum well as a function of gate voltage measured in zero magnetic field [12].

$2e^2/h$ in zero magnetic fields as described in the **figure 2.5**. This was the first experimental confirmation of a topological insulator characterized by Z_2 topology.

Before experimental verification of Z_2 topology in 2D, a TI system for 3D material was proposed by Moore *et al*. In fact, they were the first to coin the name "Topological Insulator" [13]. Fu, and Kane in 2006 made a strong prediction for 3D $Bi_{1-x}Sb_x$.The proposed theory was experimentally verified by Hsieh *et al.* in 2008 [14].

2.2.3 Basics of Topology in Topological Insulator

2.2.3.1 Berry Phase

Let $\boldsymbol{R}(t)$ be time dependent parameter a, the Hamiltonian $H[\boldsymbol{R}(t)]$ specified by the parameter $\boldsymbol{R}(t)$ and its nth eigenstates $|n, \boldsymbol{R}(t)\rangle$. Schrödinger equation of the system can be expressed as

$$H[\boldsymbol{R}(t)] \left| n, \boldsymbol{R}(t)\right\rangle = E_n[\boldsymbol{R}(t)] \left| n, \boldsymbol{R}(t)\right\rangle. \quad 2.2.1$$

Here, R changes adiabatically from t=0 value $\mathbf{R_0}$. The time evolution becomes as follows

$$H[\boldsymbol{R}(t) \left| n, t\right\rangle = i\hbar \frac{\partial}{\partial t} \left| n, t\right\rangle \quad 2.2.2$$

and the state at time t is given by

$$\left| n, t\right\rangle = \exp\left(\frac{i}{\hbar}\int_0^t dt' L_n[\boldsymbol{R}(t)\right) \left| n, t\right\rangle \quad 2.2.3$$

where,

$$L_n\ [\boldsymbol{R}(t) = i\hbar\dot{\boldsymbol{R}}(t).\langle n, |\boldsymbol{R}(t)|\nabla_R|n, \boldsymbol{R}(t)\rangle - E_n[\boldsymbol{R}(t)] \quad 2.2.4$$

When $\boldsymbol{R}$ moves on a closed loop C from t =0 and returns to the original at t = T, $\mathbf{R}(t) = \boldsymbol{R_0}$, the Berry phase γ_n[C] for this loop C is defined as

$$\gamma_n[C] \equiv \int_0^T dt\boldsymbol{R}(\dot{\boldsymbol{t}}).\ i\langle n, \boldsymbol{R}(t)|\nabla_R|n, \boldsymbol{R}(t)\rangle \quad 2.2.5$$

Solving this we can obtain the expression

$$\gamma_n[C] = -\int_S dS.B_n(\boldsymbol{R}) \quad 2.2.6$$

$$\boldsymbol{B_n}(\boldsymbol{R}) = \nabla_R \times \boldsymbol{A_n}(\boldsymbol{R}) \quad 2.2.7$$

Here, $\boldsymbol{B_n}(\boldsymbol{R})$ is the Berry curvature with

$$\boldsymbol{A_n}(\boldsymbol{R}) = -i\langle n, \boldsymbol{R}|\nabla_R|n, \boldsymbol{R}\rangle \quad 2.2.8$$

Equation (2.2.6) is in the form of Stoke's theorem. Berry Phase means the accumulated phase factor of a quantum mechanical system after completing a closed path [15].

2.2.3.2 Time-Reversal Operator

The time reversal **TR** operator Θ for a spin ½ particles takes the form $\Theta = -iS_y\boldsymbol{K}$,

Where K, is the complex conjugate operator and $S_\mu(\mu = x, y, z)$ denotes the spin operator given by Pauli matrices. **TR** operator has a property

$$\Theta^2 = -1 \qquad 2.2.9$$

Taking the eigenstates of S_z as the basis set$\{\langle\sigma\rangle\}$, we will get

$$\langle\psi|\sigma|\varphi\rangle = \sum_{\sigma,\sigma'}\langle\psi|\sigma\rangle\langle\sigma|(-is_Y|\sigma'\rangle\langle\sigma'|\varphi^*\rangle$$

$$= -\sum\langle\psi|\sigma^*\rangle\langle\sigma^*|iS_y|\sigma'\rangle\langle\varphi|(\sigma')^*\rangle$$

$$= -\sum\langle\sigma|\psi^*\rangle\left\langle(\sigma')^*\left|(iS_y)^+\right|\sigma\right\rangle\langle\varphi|(\sigma')^*\rangle$$

$$= -\sum\langle\varphi|(\sigma')^*\rangle\left\langle(\sigma')^*\left|(-iS_y)^+\right|\sigma\right\rangle\langle\varphi|(\psi^*)\rangle$$

$$= -\langle\varphi|\Theta|\psi\rangle \qquad 2.2.10$$

Similarly, we can show

$$\langle\Theta\psi|\Theta\varphi\rangle=\langle\varphi|\psi\rangle \qquad 2.2.11$$

2.2.4 Topological Crystalline Insulator

We already knew that Z_2 invariance TI materials from valance band Bloch wave function is based on time reversal symmetry TRS. It has recently discovered that it is not only the possible topological classification of band structures, but also possible to explain the band structures based on topologically protected by point-group symmetries. Those TI materials in which symmetry is protected by point-group symmetry are called Topological Crystalline Insulators (TCIs). TCI behavior is predicted for materials possessing four fold (C_4) or six fold (C_6) rotational symmetry and also with the systems having mirror symmetry. Tin telluride (SnTe) has gained significance interests as it was identified as a mirror symmetry protected topological crystalline insulator by Hsieh *et al.* [17].

Some of the research topics based on current topological insulator are listed below:

- Topological crystalline insulator
- Topological superconductivity
- Topological semimetals
- Topological defects

This thesis will describe in detail in a later chapter about the topological crystalline insulator.

2.3 Application of Topological Insulating States

The discovery of a topological insulator phase promises new opportunities for the next generation electronic devices. A unique property of TI materials is that electrons can flow at the surface without dissipation while the bulk can serve as an insulator ideal for semiconducting materials.

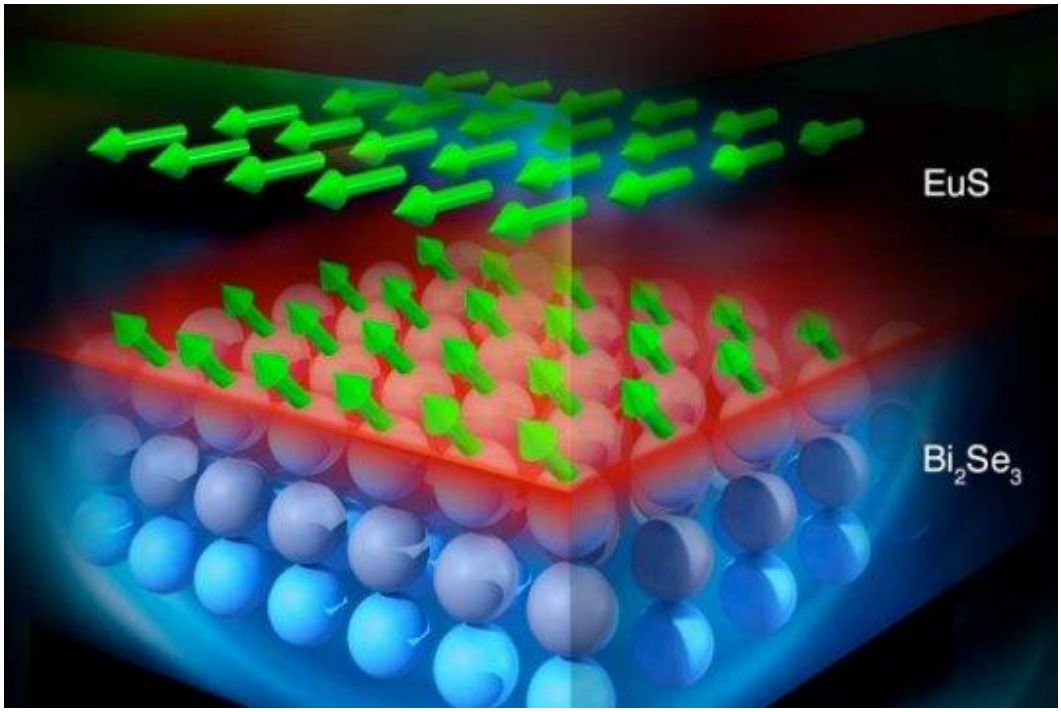

Figure 2.6: Cartoon showing Bi2Se3- EuS bilayer films.

The 3D TI material has a thickness independent electric resistance, which is a very important practical potential property. It was experimentally discovered that the conduction of electrons were topologically protected in these materials, which means their surfaces are guaranteed to be robust conductors. In the experiments, it was found that slice off thin layers from the surface of the material and after each thinning of the material, the surface maintained its conductance without the slightest change**.** This conduction on the surface of topological insulators is important for spintronic devices**.** We can also use them in real world applications, by introducing the magnetic layers. To introduce magnetism in TIs/TCIs two ideas have proposed: first by doping impurities in which magnetic atoms are incorporated and the second is by introducing an insulating magnetic layer over the TI/TCI surface. The latter idea can serve clean atomic sharp interface with crystalline orientation between TI/TCI and insulating magnetic layers. This discovery is first studied by Katmis *et al.* by introducing hetrostructures of TI, Bi_2Se_3 with a ferromagnetic EuS layer at the

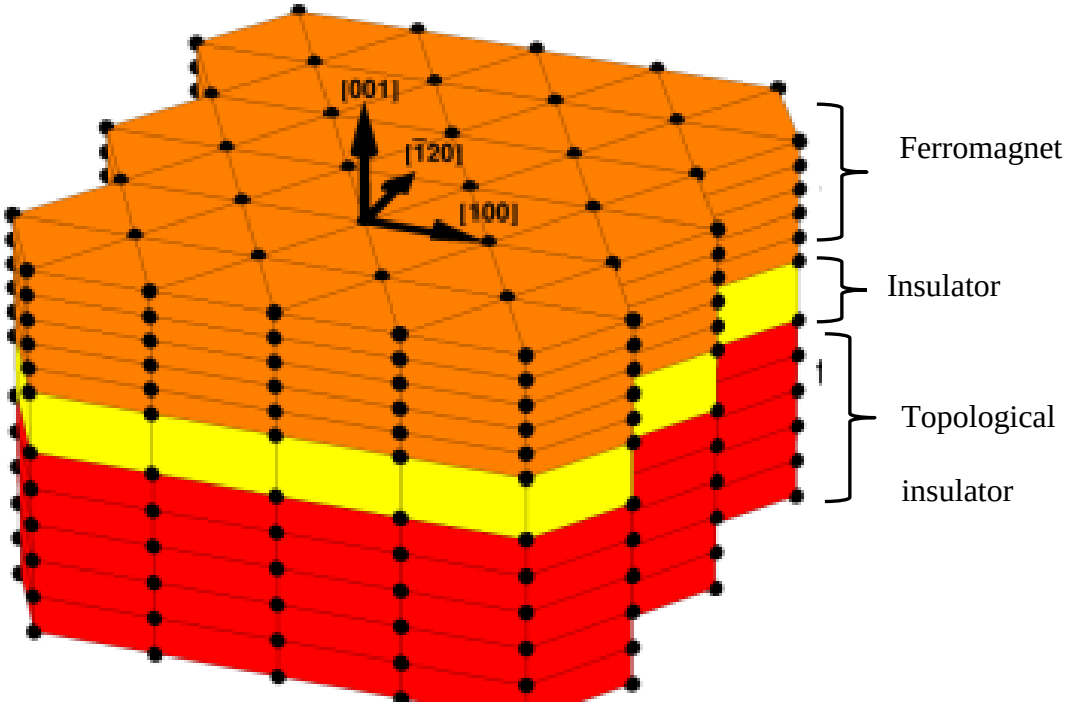

Figure 2.7: Schematic of a set up to describe a TMR device.

surface as shown in **figure 2.6** [17]. The specific spin directions of the ferromagnetic insulator in proximity to the TI enable dissipation-free, spin-polarized (i.e. magnetic) electron flow in a thin layer close to the interface. They observed magnetic behavior has survived well above the Curie temperature. The Curie temperature of EuS is 17 K but they found a magnetic signal can exist up to room temperature. This discovery could open door for designing spintronic devices to a new level. One recent research on tunneling magnetoresistance coupled via tunnel barrier to a topological insulator has shown some interesting results [18]. In contrast to conventional TMR junctions, it does not need a second ferromagnetic layer, because the spin locking in the topological insulator already provides an intrinsic magnetic reference. Additionally, the device can be used to probe the spin-locked surface states in the TI and the maximum TMR ratio can be obtained from the material properties of TI. This is another aspect of TI materials useful in future electronic devices.

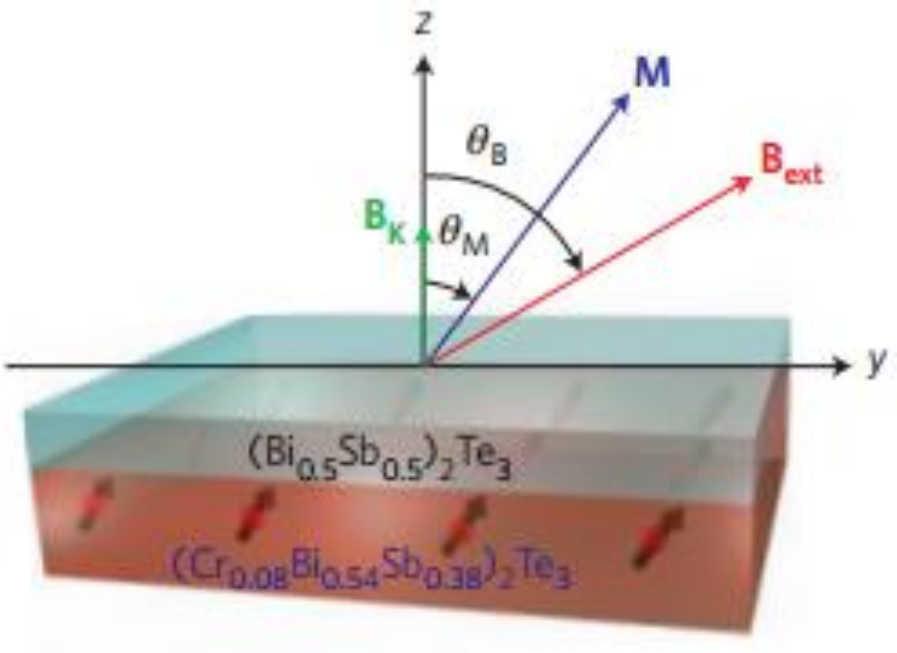

Figure 2. 8:Three-dimensional schematic of thebilayer heterostructure. The top layer (light blue) shows the 3 quintuple layers $(Bi_{0.5}Sb_{0.5})_2Te_3$ and the bottom layer (light red) presents the 6 quintuple layers $(Cr_{0.08}Bi_{0.54}Sb_{0.38})_2Te_3$. B_{ext} (red arrow) represents the external magnetic field and M (blue arrow) denotes the magnetization of the bottom $(Cr_{0.08}Bi_{0.54}Sb_{0.38})_2Te_3$ layer. BK (green arrow) is the out-of-plane anisotropy field [20].

Fan et al. introduced new topological insulator devices in which one of the two layers is magnetized as shown in **figure 2.8**. The interiors of a topological insulator prevent the flow of electric current, but their surfaces permit the electron transport of spin-polarized current without having “scattering” of electrons that protects energy to be dissipated and wasted [20]. They have shown TI can be used electronically “switched” to make energy-efficient and found surprisingly that it used 1000 times less energy to switch polarity than the current devices. This can lead to the development of much energy efficient big-data processing system with very low-power-consumption.

2.4 Topological Insulating Materials

Several materials have already been found to be exhibiting topological insulating behavior. CdTe/HgTe/CdTe was the first identified quantum well, which had shown TR-invariant topological insulating behavior. Recently another 2D TI system AlSb/InAS/GaSb/AlSb quantum well was theoretically predicted [19]. There are special families of compounds having higher spin-orbit coupling, which have shown TI and TCI behaviors. Some of these families are Bi_2Se_3 and its related materials, $TlBiSe_2$ (Tl=Thallium) family, $LaBiTe_3$ family, $PbBi_2Se_4$ family, HgTe, $Bi_{1-x}Sb_{1-x}$ and related compounds, PbTe, SnTe and their related compounds. The following table gives a summary of the TI and TCI materials which have been experimentally identified as a TI material so far.

Table 2.1: List of materials showing TI behaviors

Material	**Band Gap**	**Bulk Transport**
CdTe/HgTe/CdTe	<10 meV	insulating
AlSb/InAs/GaSb/AlSb	~ 4meV	weakly insulating
$Bi_{1-x}Sb_x$	<30 meV	weakly insulating
Sb	semimetal	metallic
Bi_2Te_3	0.17 eV	metallic
Bi_2Se_3	0.3 eV	metallic
Bi_2Te_2Se	~ 0.2 eV	reasonably insulating

$(Bi,Sb)_2Te_3$	< 0.2 eV	moderately insulating
$Bi_{2-x}Sb_xTe_{3-y}Se_y$	< 0.3 eV	reasonably insulating
$Bi_2Te_{1.6}S_{1.4}$	0.2 eV	metallic
$Bi_{1.1}Sb_{0.9}Te_2S$	0.2 eV	moderately insulating
Sb_2Te_2Se	…….	metallic
$Bi_2(Te,Se)_2(Se,S)$	0.3 eV	Semi-metallic
$TlBiSe_2$	~0.35 eV	metallic
$TlBiTe_2$	~0.2 eV	metallic
$TlBi(S,Se)_2$	< 0.35 eV	metallic
$PbBi_2Te_4$	~ 0.2 eV	metallic
$PbSb_2Te_4$	……	metallic
$GeBi_2Te_4$	0.18 eV	metallic
$PbBi_4Te_7$	0.2 eV	metallic
$GeBi_{4-x}Sb_xTe_7$	0.1-0.2 eV	metallic
$(PbSe)_5(Bi_2Se_3)_6$	0.5 eV	metallic
$(Bi_2)(Bi_2Se_{2.6}S_{0.4})$	semimetal	metallic

$(Bi_2)(Bi_2Te_3)_2$	……	……..
Ag_2Te	……	…….
SmB_6	20 meV	insulating
$Bi_{14}Rh_3I_9$	0.27 eV	metallic
RBiPt (R = Lu, Dy, Gd)	zero gap	metallic
$Nd_2(Ir_{1-x}Rh_x)_2O_7$	zero gap	metallic
*SnTe	0.3 eV	metallic
*$Pb_{1-x}Sn_xTe$	< 0.3 eV	metallic
*$Pb_{0.77}Sn_{0.23}Se$	Invert with T	metallic
Bi bilayer	~0.1 eV	metallic

***Topological crystalline insulating materials: surface state is protected by crystal symmetry**

Bibliography

[1] M. Franz, and L. Molenkamp, “Contemporary concepts of condensed matter science, Topological insulator”, volume 6, ISBN-13: 978-0444633149

[2] Nakahara M. Geometry, topology and physics, Bristol: Adam Hilger; 1990.

[3] A. Stern, “Non-Abelian states of matter”, Nature, Vol. 464, Mar. 2010.

[4] K. V. Klitzing, G. Dorda, and M. Pepper, “New method for High-Accuracy Determination of the Fine--Structure Constant Based on Quantized Hall Resistance” Physical Review Letters, Vol. 45, No. 6, Aug 1980.

[5] X. - L. Qi, and S. –C. Zhang, “The quantum spin Hall effect and topological insulators”, American Institute of Physics, S-0031-9228-020-3.

[6] M. I. D’yakonov and V. I. Perel’: JETP Lett. 13, 467 (1971).

[7] Y. K. Kato, R. C. Myers, A. C. Gossard, and D. D. Awschalom: Science 306, 1910 (2004)

[8] C. L. Kane, and E. J. Mele: Phys. Rev. Lett. 95, 226801 (2005).

[9] C. L. Kane, and E. J. Mele: Phys. Rev. Lett. 95 146802 (2005).

[10] B. A. Bernevig, and S. C. Zhang: Phys Rev. Lett 96, 106802 (2006).

[11] A. K. Geim, and K. S. Novoselov: Nature Materials 6,183 (2007).

[12] B. A. Bernevig, T. L. Hughes, and S. –C. Zhang: Science 314, 1757(2006).

[13] L. Fu, C. L. Kane, and E. J. Mele: Phys. Lett. 98, 106803 (2007).

[14] D. Hsieh, D. Qian, L. Wray, Y. Xia, Y. S. Hor, R. J. Cava, and M. Z. Hasan: Nature 452, 970(2008).

[15] Y. Ando, J. Phys. Soc. Jpn. 82, 10, 102001(2013).

[16] T. H. Hsieh, H. Lin, J. Liu, W. Duan, A. Bansil, and L. Fu. : Nature Commum. 3, 982 (2012).

[17] F. Katmis, V. Lauter, F. S. Nogureira, B. A. Assaf, M. E. Jamer, P. Wei, B. Satpati, J. W. Freeland, I. Eremin, D. Heiman, P. J- Herrero, and J. S. Moodera, A high-temperature ferromagnetic topological insulating phase by proximity coupling, Nat, **000**, (2016).

[18] M. Gotte, T. Paananen, G. Reiss, and T. Dahm, Tunneling magnetoresistance devices based on topological insulators: Ferromagnet/insulator/topological-insulator junctions employing Bi2Se3, Phys. Rev. Appl. **2**, 054010 (2014).

[19] C. Liu, T. L. Hughes, X.-L. Qi, K. Wang, and S.-C. Zhang, Quantum Spin Hall Effect in Inverted Type-II Semiconductors, Phys. Rev. Lett. 100 (2008) 236601.

[20] Y. Fan, P. Upadhyaya, X. Kou, M. Lang , S. Takei , Z. Wang, J. Tang , L. He, L.-T. Chang, M. Montazeri, G. Yu, W. Jiang, T. Nie , R. N. Schwartz, Y. Tserkovnyak and K. L. Wang, Magnetization switching through giant spin–orbit torque in a magnetically doped topological insulator heterostructure, Nature Mater. **13**, (2014).

Chapter 3: Nanostructures Synthesis and Characterization Techniques

This chapter will discuss the chemical and physical synthesis techniques adopted for the fabrication of nanostructured materials. There is a myriad of possible techniques to characterize nanostructures after the growth. They include X-ray diffraction (XRD), Scanning Electron Microscopy (SEM), Transmission Electron Microscopy (TEM), Electron Dispersive X-ray (EDX) analysis. Magnetic properties were studied using Vibrating Sample Magnetometer (VSM). Electrical and magneto-transport properties were measured from a nanoscale device fabricated using e-beam lithography. The actual measurements were carried out using a Physical Property Measurement System (PPMS), Agilent semiconducting parametric analyzer and with Keithley current source. We will not go into detail concerning the methods used, but, rather, only outline the basic principles and provide examples of a few of the techniques that have been used successfully and provide references for further inquiry.

3.1 Nanostructure Synthesis

There are several techniques available for the synthesis of nanostructures. Some of them are listed below:

- Electrospinning
- Chemical Vapor deposition
- E-beam lithography
- Template based electrodeposition

- Hydrothermal
- Solvothermal
- Wet-chemical

This thesis will discuss the hydrothermal, solvothermal and the wet-chemical syntheses, since I have used these methods for the synthesis of the nanostructures.

3.2 Hydrothermal

The term **hydrothermal** refers to a heterogeneous reaction in the presence of aqueous solvents under high pressure and temperature conditions to dissolve and recrystallize materials that are relatively insoluble under ordinary conditions. Based on the literatures, researchers have wide varieties of methods of defining hydrothermal techniques. Laudise suggested, hydrothermal growth means growth from aqueous solution at ambient or nearly ambient condition [1]. Lobbachey defined it as a method in which crystallization was carried out from a suspended aqueous solution at high pressure [2]. According to Rabenau, hydrothermal synthesis is a heterogeneous reaction in aqueous media above 100 ^{0}C at 1bar pressure [3]. Nowadays this method is mostly in use for the synthesis of single crystal that depends upon the solubility of minerals in hot water under high pressure.

The term hydrothermal has a geological origin. The term hydro means water and thermal means heat. It was first found to be used by a British geologist, Sir Roderick Murchison (1972-1871) to describe the action of water at elevated temperature and pressure in the earth's crust leading to the formation of rocks and minerals [4].

3.2.1 Water as a Reaction Medium

Water is used as a solvent for the hydrothermal synthesis. Benefits of using water as a solvent are that it is the cheapest solvent, it is thermodynamically stable and nontoxic. It can be used as a

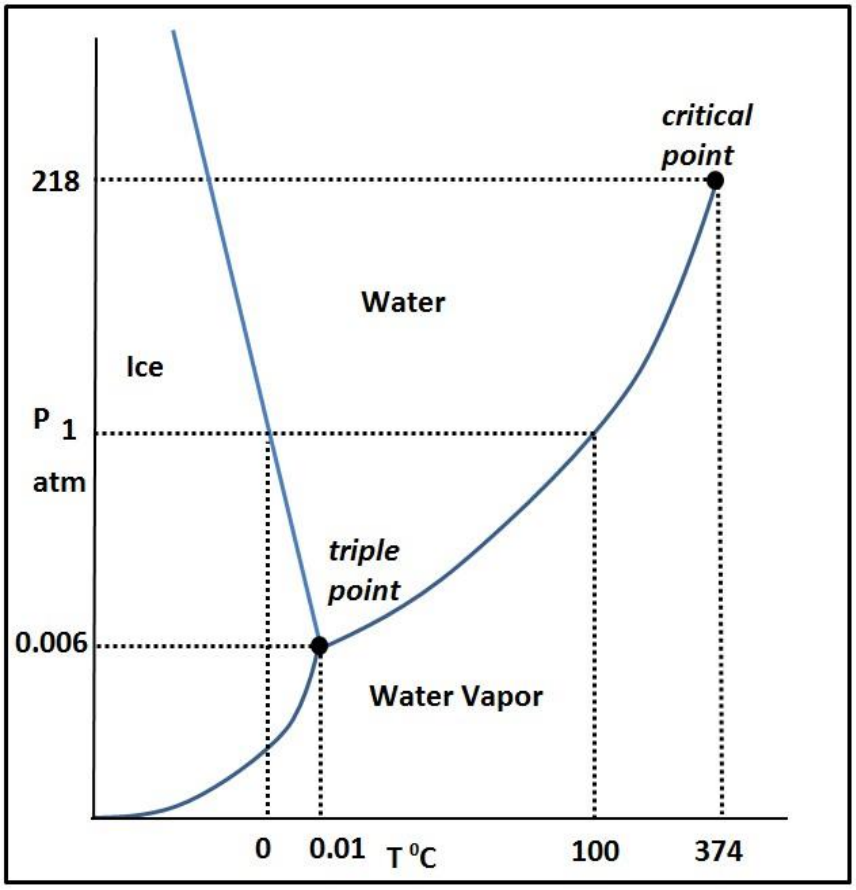

Figure 3.1: Phase diagram of water.

catalyst for the formation of desired materials with tuning temperature different properties at above 100 ^{0}C and above 1 atm, which is described on the basis of the phase diagram shown in **figure 3.1**. The phase boundary between liquid and gas does not continue after a critical point. It means, liquid and gas phases are indistinguishable and water becomes a supercritical fluid above the critical point. Critical point occurs at the critical temperature (T_c) at 373.946 ^{0}C and at critical pressure (P_c) 217.75 atm. Supercritical phase has higher diffusivity with a lower viscosity than ordinary water that can dissolve and migrate more rapidly. The other important properties of hydrothermal

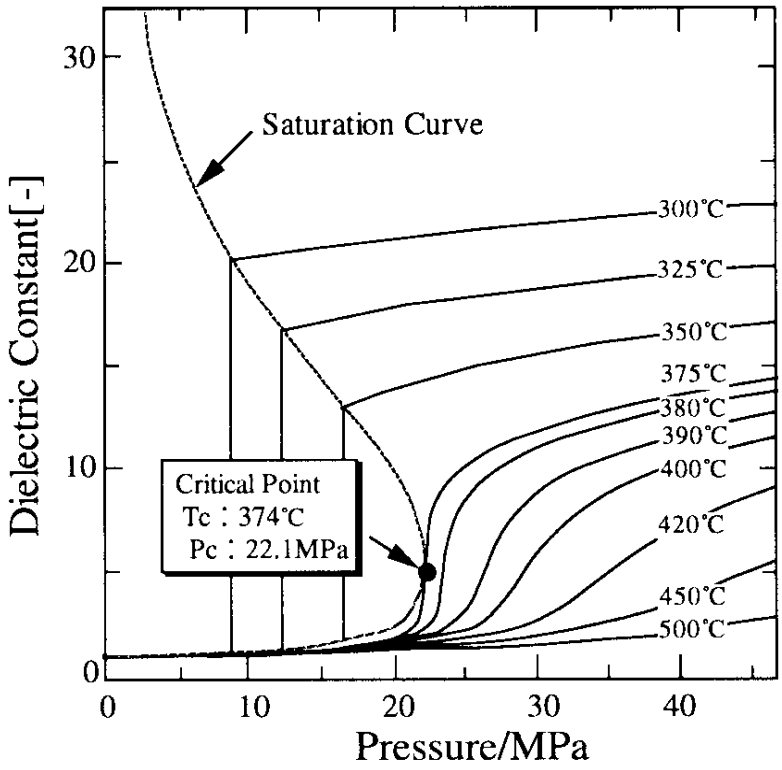

Figure 3.2: Variation of dielectric constant of water solvent with temperature and pressure.

synthesis are dielectric properties which are described in **figure 3.2**. Interestingly, it is found that the dielectric constant of water can be controlled by controlling temperature and pressure. The physical and chemical properties of water and aqueous solution, in the temperature and pressure range, necessary for hydrothermal synthesis has been studied in numerous review articles. The Pressure -Volume-Term (PVT) data for water up to 100 ^{0}C and 10 kbar are known accurately [5]. Water is a polar solvent and its polarity can be controlled by controlling the temperature and pressure, which will be an additional advantage of using water as a solvent. Additionally, hydrothermal synthesis can be hybridized with other process like electrochemistry, ultrasound, microwave, optical radiation hot-processing to gain advantages in the ability of making new materials. Hydrothermal methods have been extensively used to fabricate single and polycrystalline compounds of different morphologies.

3.2.2 Autoclave for hydrothermal

Figure 3.3: Autoclave for hydrotthermal synthesis.

Material synthesis using a hydrothermal route requires a special reaction vessel known as *autoclave* shown in **figure 3.3**. An autoclave must be capable of holding high temperature and pressure for a longer time with corrosive salt and minerals inside the vessel. In general autoclaves are made with corrosion resistant materials, high strength alloys, such as 316 series stainless steel, iron, nickel, cobalt- based super alloys, and titanium and its alloys. To avoid corrosion of autoclave material it should have another inner container of non-reactive material lined up with autoclave called Teflon. These autoclaves have many advantages over other reaction vessels. For instance, they are completely inert to aqueous base and fluorides. They are inexpensive and easy to operate, require no specific knowledge and crystal can grow research as well as industrial levels. The only limitation of using autoclaves for hydrothermal is the maximum operating temperature and pressure for autoclave cannot exceed 300 ^{0}C and 1800 psi respectively.

3.2.3 Synthesis Mechanism

Hydrothermal is a solution based synthesis and the advantages of solution based techniques are they permit crystal growth at low temperature well below the melting point and the isothermal growth conditions gives the slow material growth rate which provides a high quality crystal growth [6]. Hydrothermal reactions are carried out above the boiling point of the solvent. Also the high pressure affords to increase the solubility for the better crystallization of the materials. For nanostructure synthesis, several hydrothermal synthesis techniques have been proposed; some of them are temperature difference method, temperature reduction method and metastable phase method [6]. In the *temperature difference* method, the autoclave is heated from the lower part to create temperature gradient inside the solution. The hot saturated solution at the lower part rises to the upper part by convention and transforms into a supersaturated solution by cooling as a result crystallizes in nutrient of the solution. In temperature reduction technique, the autoclave is heated uniformly to a supersaturated solution which crystallizes the materials. The metastable phase method is based on the difference in solubility between the phase to be grown and that serving as the starting materials. The nutrient consists of compounds that are thermodynamically unstable under high pressure and temperature. This technique is generally combined with one of the other two techniques described above.

3.3 Solvothermal

Solvothermal synthesis is a method of producing chemical compounds similar to the hydrothermal techniques, the only difference is that the precursor solution is not aqueous but most of the times these are polar organic solvents, with conditions similar to those used in hydrothermal regimen. For solvothermal, the choice of solvent is the most important for the synthesis of target compounds.

A different choice of solvents always leads to different results. Some solvothermal synthesis consists of a mix-solvents and it becomes more complicated to analyze than the single solvent synthesis. Some studies have shown that products with special morphologies or special properties could be obtained from mix-solvents [7]. Some of the commonly used solvents in the solvothermal synthesis along with their physical properties are listed in table 3.1. Due to the large varieties of solvents or mix-solvents, solvothermal process likely to be more important for developing materials for research as well as for industrial applications in mild temperature and pressure conditions [8], [9].

Solvent	formula	MW	boiling point (°C)	melting point (°C)	density (g/mL)	solubility in water (g/100g)	Dielectric Constant[3,4]	flash point (°C)
acetic acid	$C_2H_4O_2$	60.05	118	16.6	1.049	Miscible	6.15	39
acetone	C_3H_6O	58.08	56.2	-94.3	0.786	Miscible	20.7(25)	-18
acetonitrile	C_2H_3N	41.05	81.6	-46	0.786	Miscible	37.5	6
benzene	C_6H_6	78.11	80.1	5.5	0.879	0.18	2.28	-11
1-butanol	$C_4H_{10}O$	74.12	117.6	-89.5	0.81	6.3	17.8	35
2-butanol	$C_4H_{10}O$	74.12	98	-115	0.808	15	15.8(25)	26
2-butanone	C_4H_8O	72.11	79.6	-86.3	0.805	25.6	18.5	-7
t-butyl alcohol	$C_4H_{10}O$	74.12	82.2	25.5	0.786	Miscible	12.5	11
carbon tetrachloride	CCl_4	153.82	76.7	-22.4	1.594	0.08	2.24	--
chlorobenzene	C_6H_5Cl	112.56	131.7	-45.6	1.1066	0.05	2.71	29
chloroform	$CHCl_3$	119.38	61.7	-63.7	1.498	0.795	4.81	--
cyclohexane	C_6H_{12}	84.16	80.7	6.6	0.779	<0.1	2.02	-20
1,2-dichloroethane	$C_2H_4Cl_2$	98.96	83.5	-35.3	1.245	0.861	10.42	13
diethyl ether	$C_4H_{10}O$	74.12	34.6	-116.3	0.713	7.5	4.34	-45
diethylene glycol	$C_4H_{10}O_3$	106.12	245	-10	1.118	10	31.7	143
diglyme (diethylene glycol dimethyl ether)	$C_6H_{14}O_3$	134.17	162	-68	0.943	Miscible	7.23	67
1,2-dimethoxy-ethane (glyme, DME)	$C_4H_{10}O_2$	90.12	85	-58	0.868	Miscible	7.2	-6
dimethylether	C_2H_6O	46.07	-22	-138.5	NA	NA	NA	-41
dimethyl-formamide (DMF)	C_3H_7NO	73.09	153	-61	0.944	Miscible	36.7	58
dimethyl sulfoxide (DMSO)	C_2H_6OS	78.13	189	18.4	1.092	25.3	47	95
dioxane	$C_4H_8O_2$	88.11	101.1	11.8	1.033	Miscible	2.21(25)	12
ethanol	C_2H_6O	46.07	78.5	-114.1	0.789	Miscible	24.6	13
ethyl acetate	$C_4H_8O_2$	88.11	77	-83.6	0.895	8.7	6(25)	-4
ethylene glycol	$C_2H_6O_2$	62.07	195	-13	1.115	Miscible	37.7	111
glycerin	$C_3H_8O_3$	92.09	290	17.8	1.261	Miscible	42.5	160
heptane	C_7H_{16}	100.20	98	-90.6	0.684	0.01	1.92	-4
Hexamethylphosphoramide (HMPA)	$C_6H_{18}N_3OP$	179.20	232.5	7.2	1.03	Miscible	31.3	105

Solvent	formula	MW	boiling point (°C)	melting point (°C)	density (g/mL)	solubility in water (g/100g)	Dielectric Constant[3,4]	flash point (°C)
Hexamethylphosphorous triamide (HMPT)	$C_6H_{18}N_3P$	163.20	150	-44	0.898	Miscible	??	26
hexane	C_6H_{14}	86.18	69	-95	0.659	0.014	1.89	-22
methanol	CH_4O	32.04	64.6	-98	0.791	Miscible	32.6(25)	12
methyl *t*-butyl ether (MTBE)	$C_5H_{12}O$	88.15	55.2	-109	0.741	5.1	??	-28
methylene chloride	CH_2Cl_2	84.93	39.8	-96.7	1.326	1.32	9.08	1.6
N-methyl-2-pyrrolidinone (NMP)	CH_5H_9NO	99.13	202	-24	1.033	10	32	91
nitromethane	CH_3NO_2	61.04	101.2	-29	1.382	9.50	35.9	35
pentane	C_5H_{12}	72.15	36.1	-129.7	0.626	0.04	1.84	-49
Petroleum ether (ligroine)	--	--	30-60	-40	0.656	--	--	-30
1-propanol	C_3H_8O	88.15	97	-126	0.803	Miscible	20.1(25)	15
2-propanol	C_3H_8O	88.15	82.4	-88.5	0.785	Miscible	18.3(25)	12
pyridine	C_5H_5N	79.10	115.2	-41.6	0.982	Miscible	12.3(25)	17
tetrahydrofuran (THF)	C_4H_8O	72.11	66	-108.4	0.886	30	7.6	-21
toluene	C_7H_8	92.14	110.6	-93	0.867	0.05	2.38(25)	4
triethyl amine	$C_6H_{15}N$	101.19	88.9	-114.7	0.728	0.02	2.4	-11
water	H_2O	18.02	100.00	0.00	0.998	--	78.54	--
water, heavy	D_2O	20.03	101.3	4	1.107	Miscible	??	--
o-xylene	C_8H_{10}	106.17	144	-25.2	0.897	Insoluble	2.57	32
m-xylene	C_8H_{10}	106.17	139.1	-47.8	0.868	Insoluble	2.37	27
p-xylene	C_8H_{10}	106.17	138.4	13.3	0.861	Insoluble	2.27	27

Table 3.1: Solvents used in solvothermal synthesis with their properties.

3.4 Wet- chemical synthesis

Wet-chemistry is considered as an old-fashioned chemical science which includes precipitation, extraction, distillation, and qualitative analysis by color, melting point etc. [10]. A wet-chemical synthesis is a bottom up approach, which employs colloidal chemistry. Wet-chemical synthesis is used to produce relatively uniform nanocrystals with controlled size. In contrast, some of the techniques require high vacuum and expensive instruments; wet –chemistry synthesis is cheaper and needs only specific knowledge of chemistry. For wet -chemical methods, different reaction parameters such as precursor, surfactant, shape-direction agent, and reaction temperature can be manipulated independently. Various forms of nanocrystals like nanoparticles, nanowires, nanotubes, nanodisks, nanorods, etc., can be produced using wet-chemistry by varying the reaction conditions. Some of the most common wet chemistry techniques evolved over the decades for the synthesis of metallic and intermetallic nanostructures have been listed below:

- Chemical Reduction and Thermal Decomposition
- Microwave Method
- Radiolytic and Photochemical Method
- Electrochemical Method
- Sonochemical Method
- Reversed Michelle Method
- Multiphase Process
- Template-based Synthesis

3.5 Characterization Techniques

The synthesized nanostructures are morphologically characterized by scanning electron microscope and transmission electron microscope, structurally by using x-ray diffractometer and magnetically by using vibrating sample magnetometer.

3.5.1 Scanning Electron Microscope

The scanning electron microscope uses electrons for imaging, much as a light microscope uses visible light. The advantages of SEM over light microscopy include much higher magnification (>100,000X) and greater depth of field up to 100 times that of optical microscopy. In an SEM, fine probe of electrons having energies up to 40 keV is focused on a specimen, and scanned along the pattern of parallel line [11]. History of SEM starts with the development of electron optics in 1926 by Busch [11]. Knoll built a first "scanning microscope" in 1935 but it was not used demagnifying lenses to produce a fine beam. As a result the limit of resolution was around 100 μm. In 1938, Von Ardenne developed a theory underlying a scanning microscope, as we know it today [11]. The

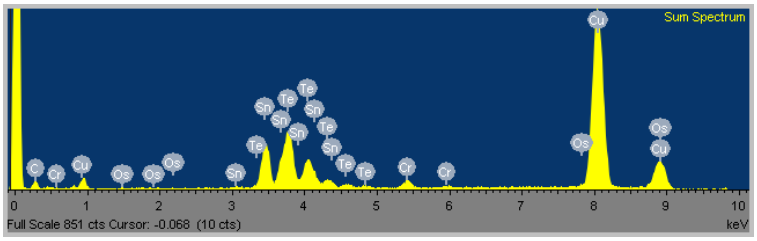

Figure 3.4: EDX Spectrum of SnTe Sheets.

first complete SEM was designed in 1942 by Zworykin, which showed that secondary electrons

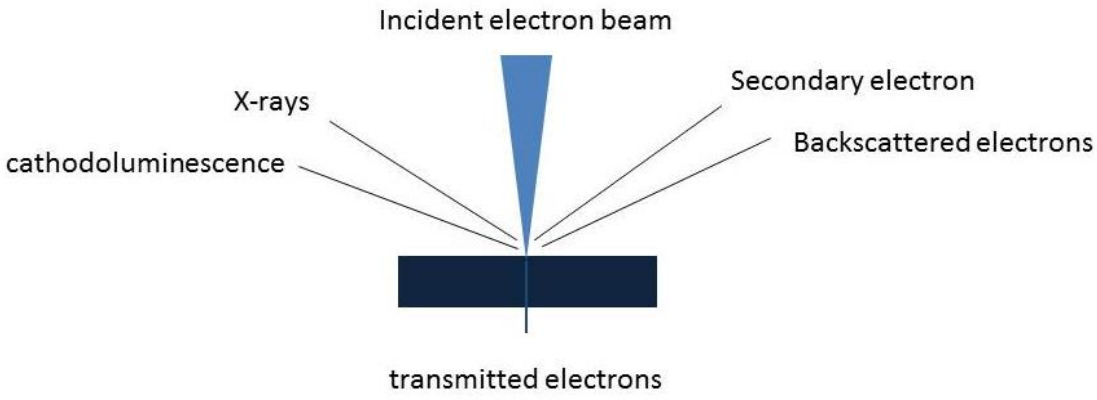

Figure 3.5: Example of some of the different types of signals produced when high-energy electron impinges on a material.

provided a topographical contrast by biasing the collector positively. Qualitative and quantitative chemical analysis information are also obtained using energy dispersive x-ray (EDX) spectrometer

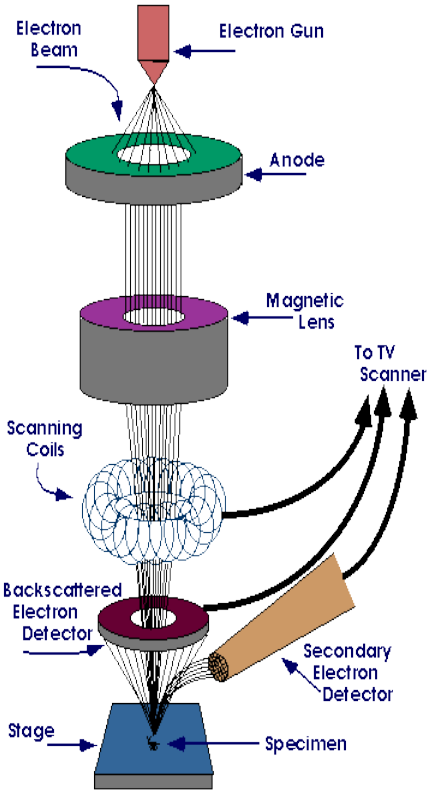

Figure 3.6: Schematic of a scanning electron microscope.

with SEM. EDX is a chemical microanalysis technique used in conjunction with scanning electron

microscopy. The EDX technique detects x-rays emitted from the sample during bombardment by an electron beam to characterize the elemental composition of the analyzed volume. Features or phase as small as 1µm or less can be analyzed. When the sample is bombarded by the SEM's electron beam, electrons are ejected from the atoms comprising the sample's surface. The resulting electron vacancies are filled by electrons from a higher state, and an x-ray is emitted to balance the energy difference between the two electrons' states. The x-ray energy is characteristic of the element from which it was emitted. The scanning electron microscope scans a beam of electrons over a specimen to produce a magnified image of an object.

3.5.2 Transmission Electron microscope

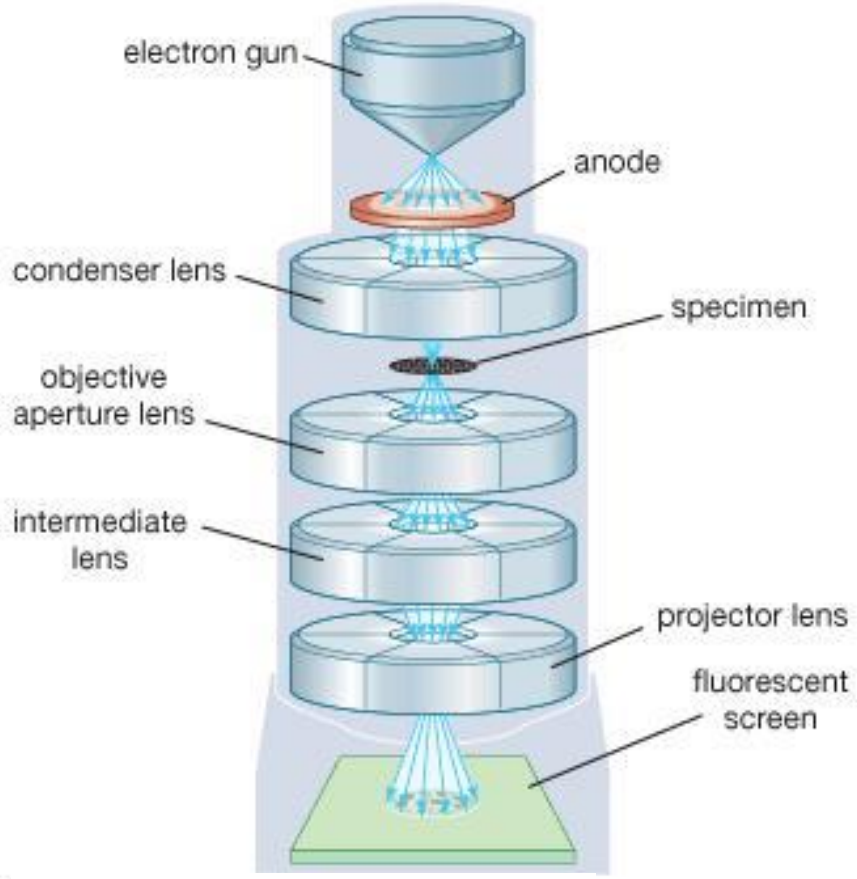

Figure 3.7: Schematic of transmission electron microscope.

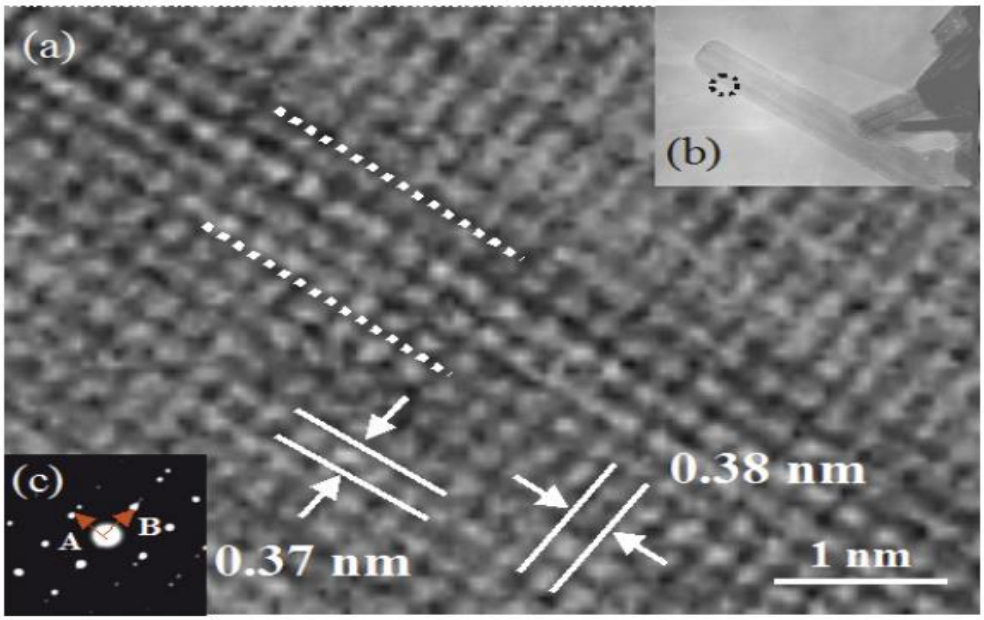

Figure 3.8: HRTEM images of a tungsten oxide nanorod.

Transmission electron microscope is a microscopy technique in which an electron beam is transmitted through an ultra- thin specimen interacting with the specimen as it passes through. An image is formed from the interaction of the electrons transmitted through the sample. TEMs are capable of imaging at a significantly higher resolution than light microscopy because of small de Broglie wavelengths of electrons. A smaller magnification of TEM image contrast is due to the absorption of electrons in the material and higher magnification is due to the complex wave interactions which modulate the intensity of the image. Based on TEM imaging crystal orientation, electronic structure, chemical identification, electronic phase shift and regular absorption can be analyzed. Max Knoll and Ernst Ruska build first TEM in 1931 which had a resolution higher than the optical microscope. Ruska was awarded Nobel prize in 1986 for the development of TEM [11]. With improved technology, currently, TEM can analyze to the order of a few angstrom (10^{-10} m). A "filament the top of the microscope emits the electron that travels through the vacuum in the column of the microscope. Instead of glass lenses focousing the light in the light microscope, the TEM uses electromagnetic lenses to focus the electrons into a very thin beam as shown in

figure 3.7. The electron beam, then travels through the specimen which we want to study. Depending on the density of the material present, some of the electrons are scattered and disappear from the beam. At the bottom of the microscope the unscattered electrons hit a fluorescent screen, which gives rise to a "shadow image" of the specimen with its different parts dispalyed in varied darkness according to their density. The image can be studied directly by the operator or photographed with a camera. High-resolution transmission electron microscope (HRTEM) has allowed the imaging of samples with a resolution below 0.5 $\dot{A}$ (with a magnification more than 50 million times). Therefore, HRTEM can determine the atomic position and defects of the sample, and the location of the atoms and the grain boundaries (**figure 3.8**) [12].

3.5.3 X-ray Diffractometer

X-ray is a form of electromagnetic radiation having wavelengths ranging from 0.01 to10 nm. X-rays with photon energies above 5-10 keV (below 0.2- 0.1 nm wavelength) are called hard X-rays, while those with lower energy are called soft X-rays. Due to their high penetrating ability, hard X-rays are only used for the diffraction purpose. X-ray diffraction (XRD) is one of the most important non-destructive tools to analyze all kinds of matter - ranging from fluids, to powders and crystals. From research to production and engineering, XRD is an indispensable method for structural materials characterization and quality control which make use of the Debye-Scherrer method. This technique uses X-ray (or neutron) diffraction on powder or microcrystalline samples, where ideally every possible crystalline orientation is represented equally. The resulting orientation averaging causes the three dimensional reciprocal space that is studied in single crystal diffraction to be projected onto a single dimension.

X-rays are mostly produced by X-ray tubes in the laboratory instruments. X-rays are generated when highly focused electron beams are accelerated by high voltage and bombards on a stationary or rotating solid target. When electrons collide with atoms in the target and slow down, a continuous spectrum of X-rays is emitted, which are known as Bremsstrahlung radiation. The high energy electrons also eject inner shell electrons in atoms through the ionization process. When a free electron fills the shell, an x-ray photon with energy characteristic of the target material is emitted. Common targets used in x-ray tubes include Cu and Mo, which emits 8 keV and 14 keV, x-rays with corresponding wavelengths of 1.54 Å and 0.8 Å, respectively.

3.5.3.1 Lattice Plane and Bragg's law

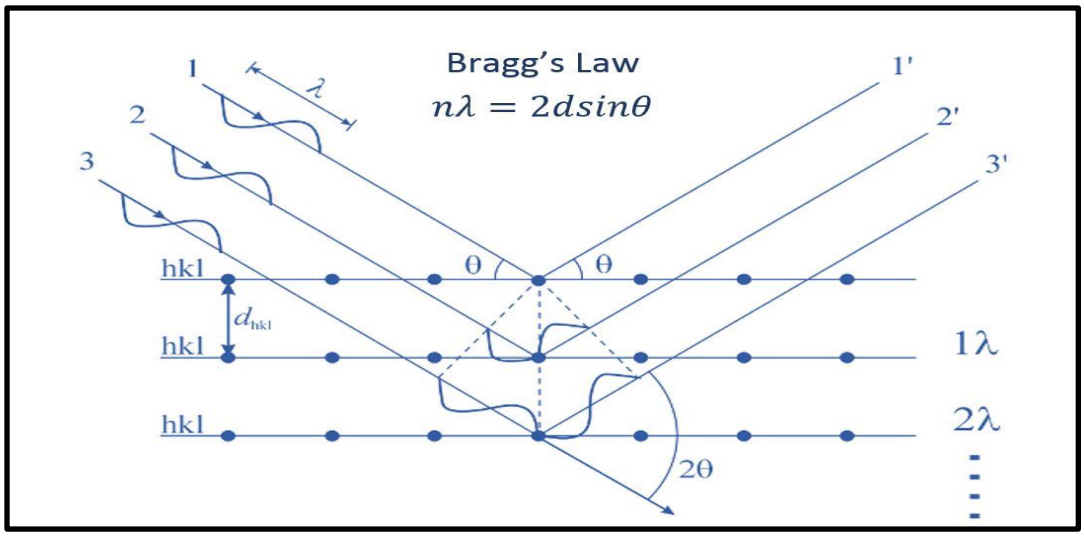

Figure 3.9: X-ray diffraction & Bragg's law.

When X-rays collide with the electrons of the sample, some photons are deflected from the original direction. If the wavelength of the scattered X-rays is same as the incident beam of X-rays then it is an elastic scattering or commonly known as Thompson Scattering. These scattered X-rays carry the electronic distribution more specifically the crystal structure of the sample materials. Diffracted

waves from different atoms can interfere with each other and the resultant intensity distribution is strongly modulated by this interaction. If the atoms are arranged in a periodic fashion, as in crystals, the diffracted waves will consist of sharp interference maxima (peaks) with the same symmetry as in the distribution of atoms. Measuring the diffraction pattern therefore allows us to deduce the distribution of atoms in a material. For a given set of lattice plane with an inter-plane distance of d, the condition for a diffraction (peak) to occur can be simply written as

$$2dsin\theta = n\lambda \qquad 3.5.1$$

Here, $\boldsymbol{\lambda}$ is wavelength of X-ray, θ is scattering angle; d is lattice spacing and n is an integer representing the order of diffraction peak.

In the Vitreous State Laboratory, we use Thermo ARL X-ray diffractometer with Cu-$K\alpha$ radiation, where λ=1.541 $\dot{A}$.

3.5.4 Vibrating Sample Magnetometer

Vibrating Sample Magnetometer is a measurement technique that allows determining the magnetic moment of a sample as a function of magnetic field, temperature and time with very high accuracy. VSM is ideally suited for research and development, production testing, quality and process control. VSM is based on Faraday's law which states that an electromagnetic force is generated in a coil when there is a change in flux through the coil [13]. Measurement setup for VSM measurement is shown in **figure 3.10**. The oscillator provides a sinusoidal signal which is transferred by the transducer assembly into a vertical vibration. The sample attached to the sample rod vibrates (generally with frequency and amplitude 60 to 80 Hz and 1 mm, respectively). The

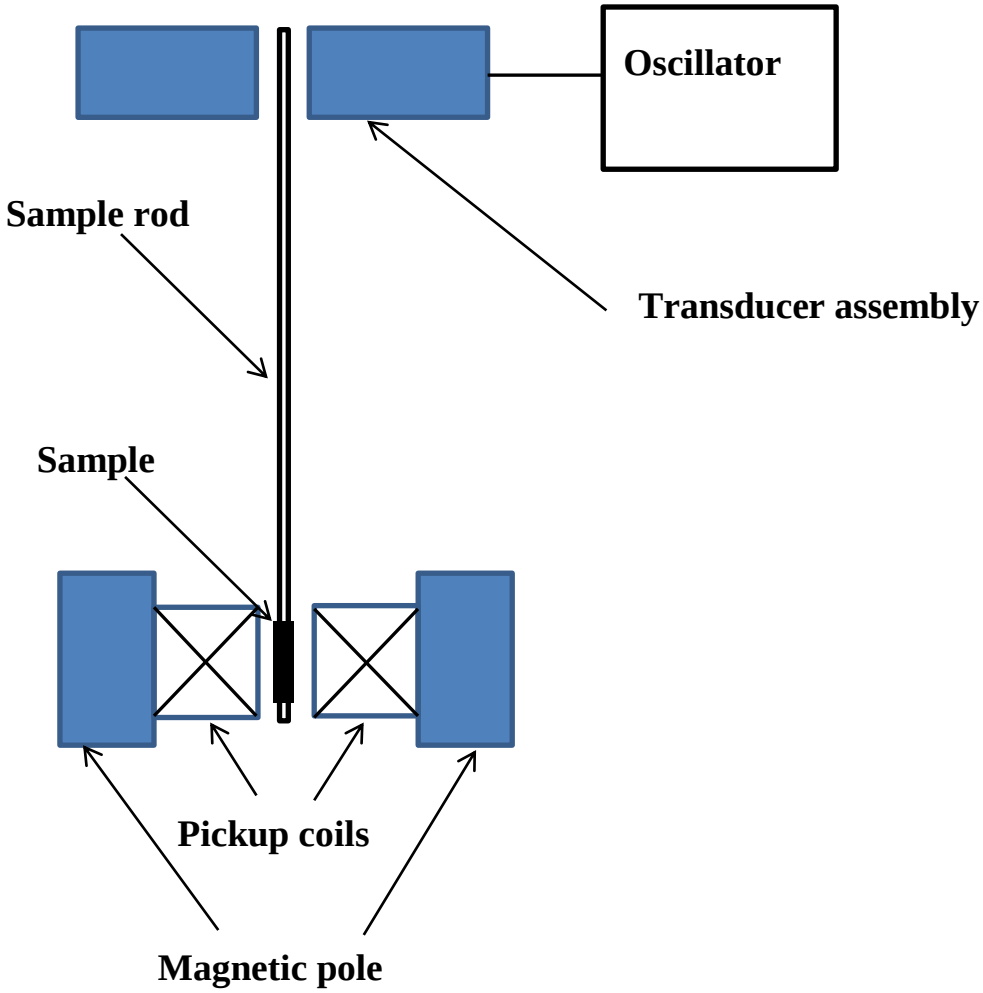

Figure 3.10: Schematic representation of a VSM.

sample is centered between two pole pieces of an electromagnet that generates a uniform magnetic field. The magnetic field may be generated by an electromagnet, or a superconducting magnet. Variable temperatures from cryogenic to high temperature are achieved using either cryostats or furnace assemblies. While a VSM measures magnetic moment m, the quantity of interest is the material's magnetization M. The magnetization M (in cgs units) can be expressed in terms of the mass (emu/g) or volume magnetization (emu/cc), and is the moment m divided by the sample mass or volume, respectively. A VSM is most commonly used to measure a material's hysteresis or M-H loop. In some cases, it is preferred to present the magnetization data in terms of the magnetic

induction B, whose CGS unit is the Gauss (G). The relation between M and B is: $B(G) = H + 4\pi M$ where M is the volume magnetization (emu/cc). In our laboratory, Quantum Design Physical Property measurement system (PPMS) (**figure 3.11**) is used to measure the electrical and magnetic properties of the materials. PPMS is facilitated with several options. It can provide a wide range of temperature ranging from 1.7 to 1000 K and magnetic field can be raised up to 9 tesla. The PPMS is equipped with superconducting solenoid immersed in liquid helium. The system is

Figure 3.11: PPMS equipped with VSM .

operated with a 40 Hz frequency and capable to detect the magnetic signal, less than 10^{-6} emu [14]

Bibliography

[1] R. A. Laudise, The growth of single crystal. Prentice- Hall, Englewood Cliffs, NJ 1970.

[2] A. N. Lobachev, Crystallization process under hydrothermal conditions, Consultants Bureau, Ney York 1973.

[3] A. Rabenau, The role of hydrothermal synthesis in preparative chemistry, Angew Chem. Int. Eng. Ed., **24**, 1985, 1026-1040.

[4] K. Byrappa and M. Yoshimura, *Handbook of Hydrothermal technology. William Andrew*, 2001.

[5] S. D. Haman, "Properties of electrolyte solutions at higher pressure and temperatures", Physics and chemistry of earth, 13/14, 89 1981.

[6] K. Byrappa and M. Yoshimura, *Handbook of hydrothermal synthesis*, William Andrew, 2001.

[7] Y. He, Y. Zhu, and N. Wu, Mixed Solvents: a key in solvothermal synthesis of $KTaO_3$, J solid state chem. **177**, 2985-90 2004.

[8] T. Miyazawa, S. Ohtsu, Y. Funazukuri, solvothermal treatment of starch for the production of glucose and maltooligosaccharides, J. Matter. Sci. **41** 1489 2006.

[9] S. Otles, V. H. Ozyurt, Classical wet chemistry methods, handbook of food chemistry Springer- Verlag Berlin Heidelberg 2014.

[10] "The Nobel Prize in Physics 4986, Perspectives- Life through a lens, nobelprize.org

[11] A. Bogner, P. –H. Jouneau, G. Thollet, B. Basset, and C. Gauthier, A history of scanning electron microscopy developments: Towards "wet-STEM" imaging, micron **38**, 390-401 2007**.**

[12] T Tokunaga, T. Kawamoto, K. Tanka, N. Nakamura, Y. Hayashi, K. Saski, K. Kuroda, and T. Yamamoto, Nanoscale Research Letter **7**, 85 2012

[13] K. H. J. Buschow and F. R. de Boer. Physics of Magnetism and Magnetic Materials. Kluwer Academic/ Plenum Publishers, 2003.

[14] Quantum Design, "Vibrating Sample Magnetometer (VSM) Option User's manual," in *Vibrating Sample Magnetometer (VSM*) Option, no. 1096, 2009.

Chapter 4: Nanoscale Device Fabrication and Measurement

Several nanolithography techniques have been developed for nanoscale device fabrication. Some of the commonly used are optical lithography, electron–beam lithography, nanoimprint lithography, multiphoton lithography, scanning probe lithography, etc. In this chapter, we will discuss in detail aboute-beam lithography, used for nanoscale device fabrication, and measurement techniques.

4.1 Electron-beam lithography

Electron-beam lithography often called e-beam lithography is the scanning of a focused beam of electrons to draw a desired pattern on a substrate covered with electron-sensitive films called resist. The exposed beam changes the solubility of the resist, enabling removal of either exposed or non-exposed region of the resist (depending upon the positive or negative type resists) during the development (immersing of substrate on a particular solvent). Important advantages of e-beam lithography over the other lithography techniques are that it does not require a mask and can draw a custom pattern with sub-10 nm resolution. Disadvantages of e-beam lithography are time consuming and need a high cost equipment. The evolution of e-beam lithography is found

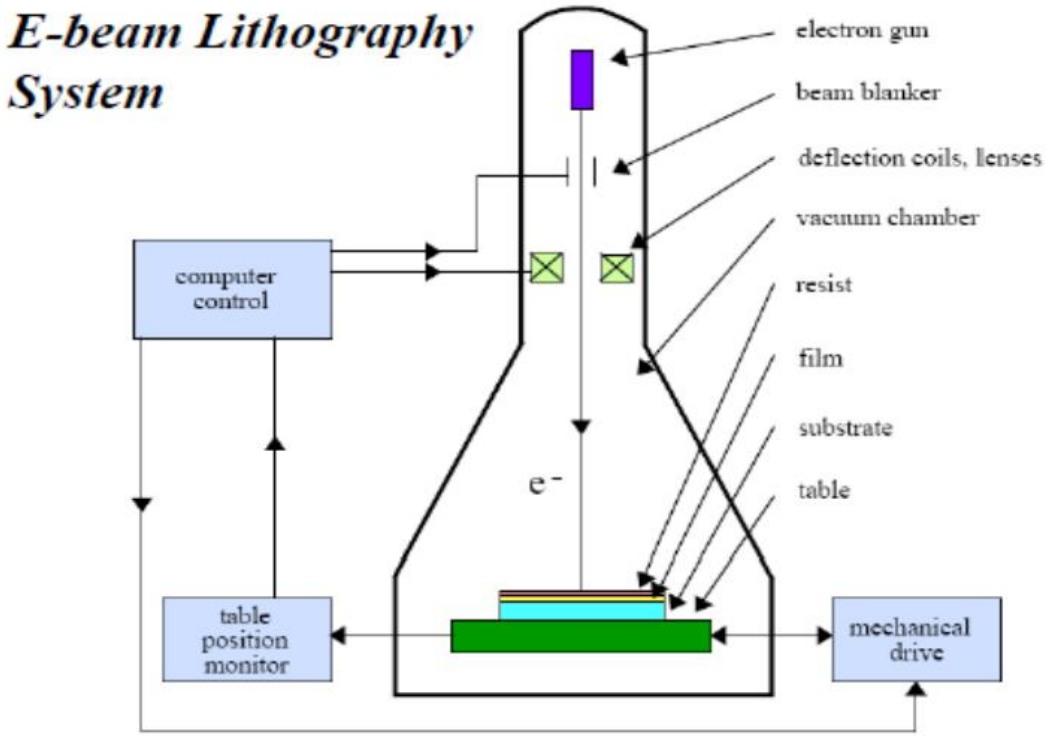

Figure 4.1: Schematic view of e-beam lithography system.

to be started in the 1960s with SEM-type Gaussian beam writing one pixel at a time directly on a wafer [1]. IBM in 1970s pioneered the concept of shaped beam containing multiple pixels which led to higher throughput and an early success of e-beam direct writing in large scale during the manufacturing of semiconductor [1]. After that quality of e-beam printing keeps on enhancing with time. Electron-beam lithography systems set up designed for commercial process are very expensive (>$ 1M) but for research application, it is very common to convert electron microscope into an electron beam lithography system using relatively low cost (<$100K). In this work, we used Nanometer Pattern Generation System (NPGS) synchronized with a scanning electron microscope. NPGS uses a true vector model with a maximum writing speed of 100 kHz [2]. A schematic view of e-beam lithography is shown in **figure 4.1.**

Fabrication of nanoscale devices using e-beam lithography takes long time and involves a number of steps. Based on particular types of nanoscale devices, some steps may vary. This thesis will explain all the necessary steps involved to complete e-beam lithography.

- ## Substrate cleaning:

Cleaning of the substrate is the first and essential step. We used Si (100) with a 500 nm of SiO_2 layer as a substrate for e-beam lithography. Substrates are cleaned several times with acetone, isopropyl alcohol (IPA) and deionized water followed by drying the substrate by baking.

- ## Traferring nanostructure on to the substrtate

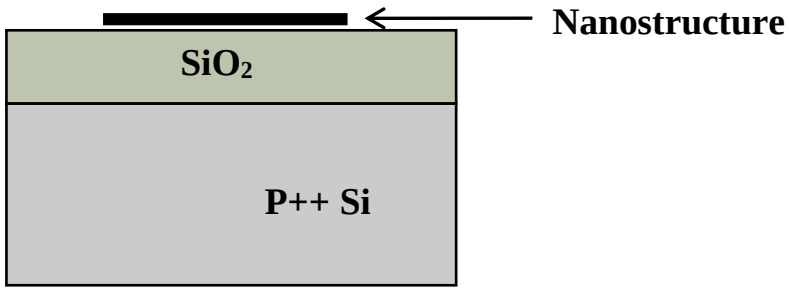

Figure 4.2: Substrate with a nanostructure transferred.

Nanostructure transfer processes are different based on the material synthesis techniques. Here nanostructure refers to nanowires, nanotubes and nanoribbons. To make single nanostructure devices, nanostructures are transferred to a cleaned Si/SiO_2 substrate. Before transferring, nanostructures are cleaned properly and dispersed in IPA solution. The nanostructures in IPA solution are dispersed on the substrate. A cartoon of nanostructure transferred to the substrate is shown in **figure 4.2.**

- **Resist Deposition**

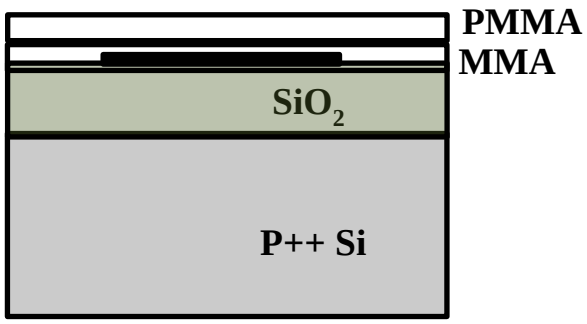

Figure 4.3: Resist deposited over the substrate.

After transferring nanostructures on the substrate, the next step is resist deposition. The resist coating can be single layer polymethyl methacrylate (PMMA) or double layers of PMMA or double layers of PMMA and methacrylate (MMA) depending on the nature of the nanostructures. PMMA and MMA are commonly used positive resists (unexposed *positive resists* have high solubility and become insoluble in developer and becomes insoluble by exposure to energetic electron-beam while *negative resist* will behave exactly opposite manner[3]) polymers containing long carbon chain. For a PMMA and MMA bi-layer, higher molecular weight PMMA form upper layer and MMA form the bottom layer. A typical thickness of MMA, PMMA is 450 nm and 100 nm respectively is applied during the spin coating. Thickness of resist coating can be controlled by different parameters like, by adjusting revolution per minute (RPM) of spun coating, and the viscosity of polymers. The spin coating of the wafer with polymers is followed by baking of the wafer at 150 ^{0}C for 5 minutes for MMA and 180 ^{0}C for PMMA for 10 minutes. The unbaked resist does not have the desired dissolution property during the development process. A cartoon of the polymer deposited on a substrate is shown in **figure 4.3**.

- **Pattern writing over the substrate (Exposure)**

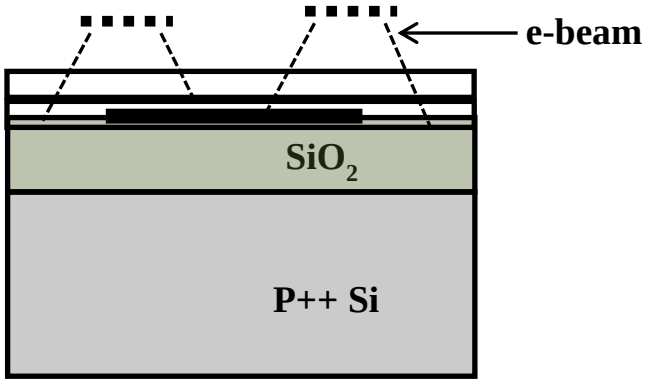

Figure 4.4: Pattern writing over the resist.

The next step in the device fabrication process after resist deposition is writing the desired pattern over the substrate. Electron - beam lithography is a specialized technique for creating extremely small and fine patterns of few of nanometers. A fine and highly focused e-beam is scanned over the resist in a desired pattern. We have used design CAD software to design the pattern which is incorporated through NPGS to write using e-beam over the electron beam sensitive resist. There are so many critical parameters that can affect the patterns. Backscattered electrons can cause proximity effect and patterns should be properly designed to correct the proximity effect. SEM imaging parameters like focusing and astigmatism are sensitive for higher resolution pattern. In this work, we used the NPGS nanolithography system capable of imprinting patterns into resist materials with a maximum writing speed of 100 kHz [4]. A cartoon view of pattern writing over the e-beam sensitive resist is shown in **figure 4.4**.

- ## Developing the expose pattern

The development process is critical for controlling the fine patterns. It is paramount to carefully control the developing solution, temperature and time. The developing solution will be different for different resists. After developing, if we have used positive resist, the exposed portion of the

resist would completely wash out while negative resist would behave exactly the opposite way. A cartoon image of developed pattern with positive resist is shown in **figure 4.5**.

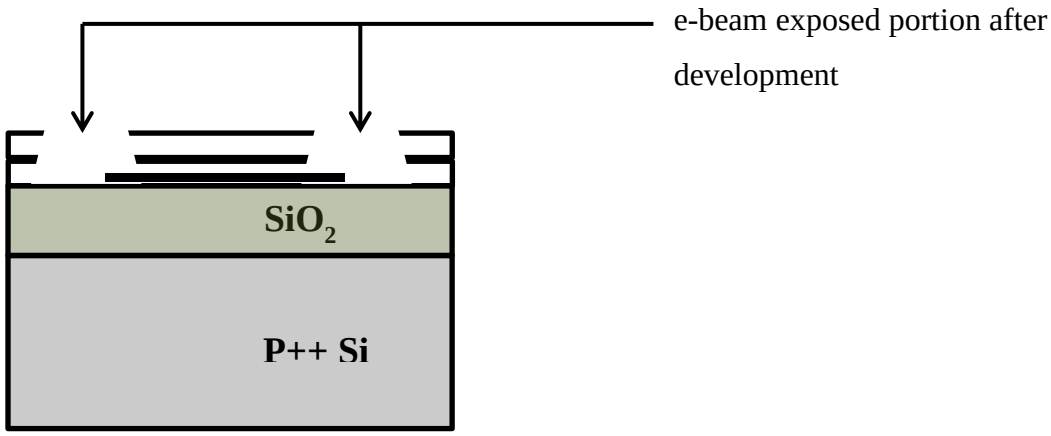

Figure 4.5: Development of the exposed pattern.

- **Etching**

Etching is the next step after the pattern is developed. It is the process of removing the uppermost layer of nanostructure, which is not protected by the photoresist. There are two different methods have used for etching, dry etching and chemical etching. Nanostructures, in general, have an oxide layer which is etched away by chemical etching. Depending upon the thickness of the oxide layer and the nanostructure, we have used hydrochloric acid (HCL), hydrofluoric acid (HF) and nitric acid (HNO_3) for etching oxide layer.

- **Electrode deposition**

Electrode deposition is the next step after development of the pattern. The lithographically patterned wafer is mounted on a substrate holder in an ultra-high vacuum (UHV) system for

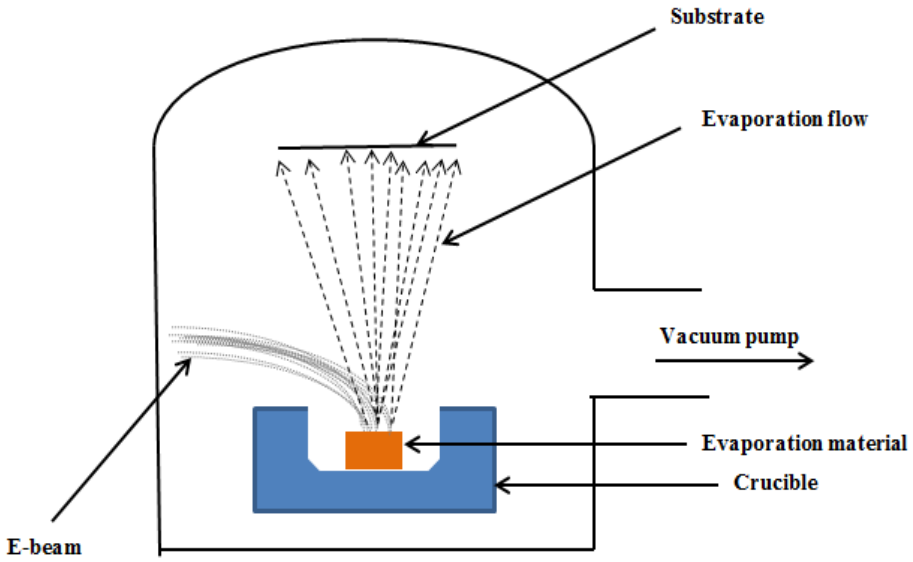

Figure 4.6: E-beam evaporation set up.

electrode deposition. Electrode deposition is performed by electron beam evaporation at a lowered pressure (~ 10^{-8} torr) pumped by means of a cryo pump. Typical e-beam evaporation set up inside the UHV system is shown in **figure 4.6.** In e-beam evaporation, the high energy electron beam is

Figure 4.7: UHV system for e-beam evaporation with a thickness monitor.

focused on the evaporant source. The electrons are emitted by a hot filament and then accelerated

by a DC voltage. The e-beam is focused on the target by a magnetic field typically bending through 270^0. The targets are placed in water-cooled copper hearths. During the e-beam evaporation, we can monitor and control the thickness of the high quality thin film deposited on the substrate. Thickness of the film is monitored using a quartz crystal which responds piezoelectrically according to the pressure produced by the deposited film. The e-beam evaporation system, we have used for electrode deposition is shown in **figure 4.7**.

- ## Liftoff

The next step after the electrode deposition is liftoff. Liftoff is done by immersing the deposited wafer into acetone. Liftoff time would vary with the type of material used for deposition and also

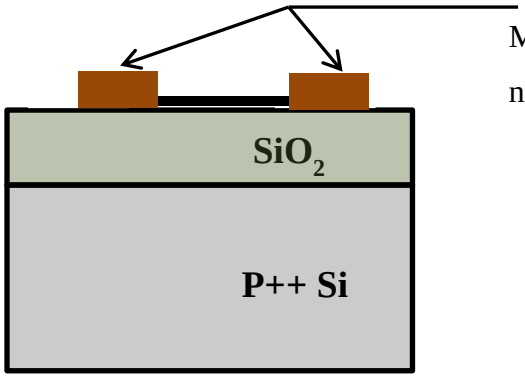

Figure 4.8: Device after liftoff (sideview).

with the thickness of thin films. Acetone dissolves MMA and PMMA during liftoff. As a result, all deposited thin film comes out except the thin film (electrodes) deposited in the lithographically designed channel. A carton of liftoff device after the deposition is shown in **figure 4.8.**

- ## Device Packing

After liftoff, the next and final step is device packaging before the measurement is carried out. Device packaging is done with a wire bonder, the device chip is connected to the device puck using

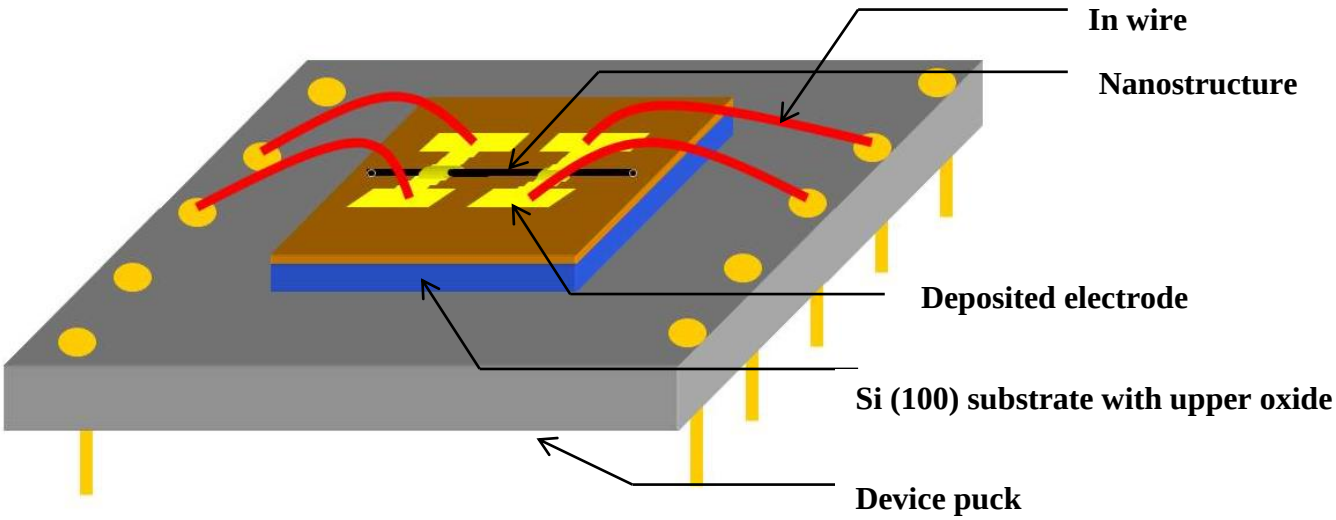

Figure 4.9: Wire-bonded nanoscale devices (top view).

gold wires. After wire bonding, the device puck is connected to the probe and placed inside the PPMS system, which can measure various properties of the nanostructures. The temperature can be varied from 1.7 K to 400 K and the magnetic field up to 9 Tesla. The cartoon of a nanodevice after wire bonding packing and just before the measurement is shown in **figure 4.9** and actual devices before measurement are shown in **figure 4.10.**

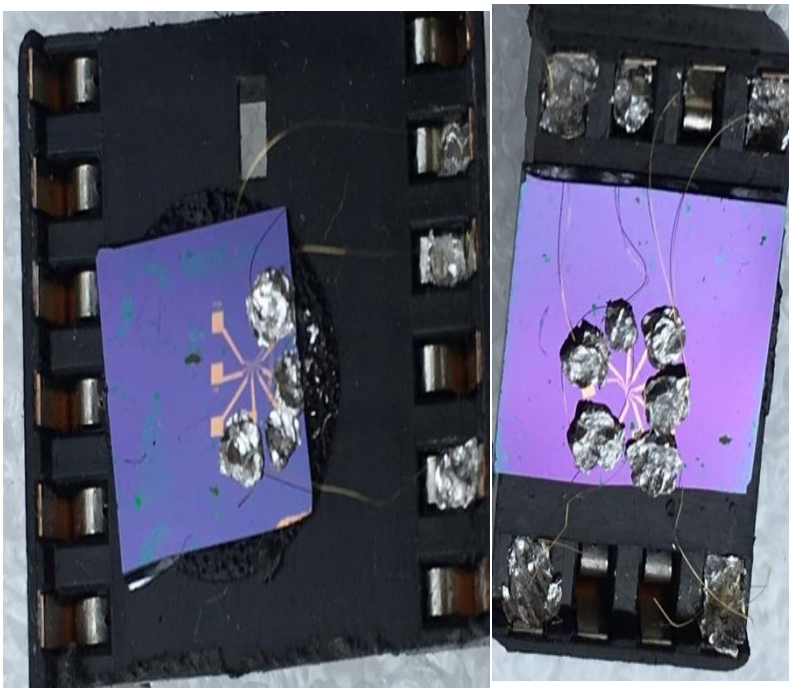

Figure 4.10: Nanodevices on measurement sockets.

4.2 Device measurements

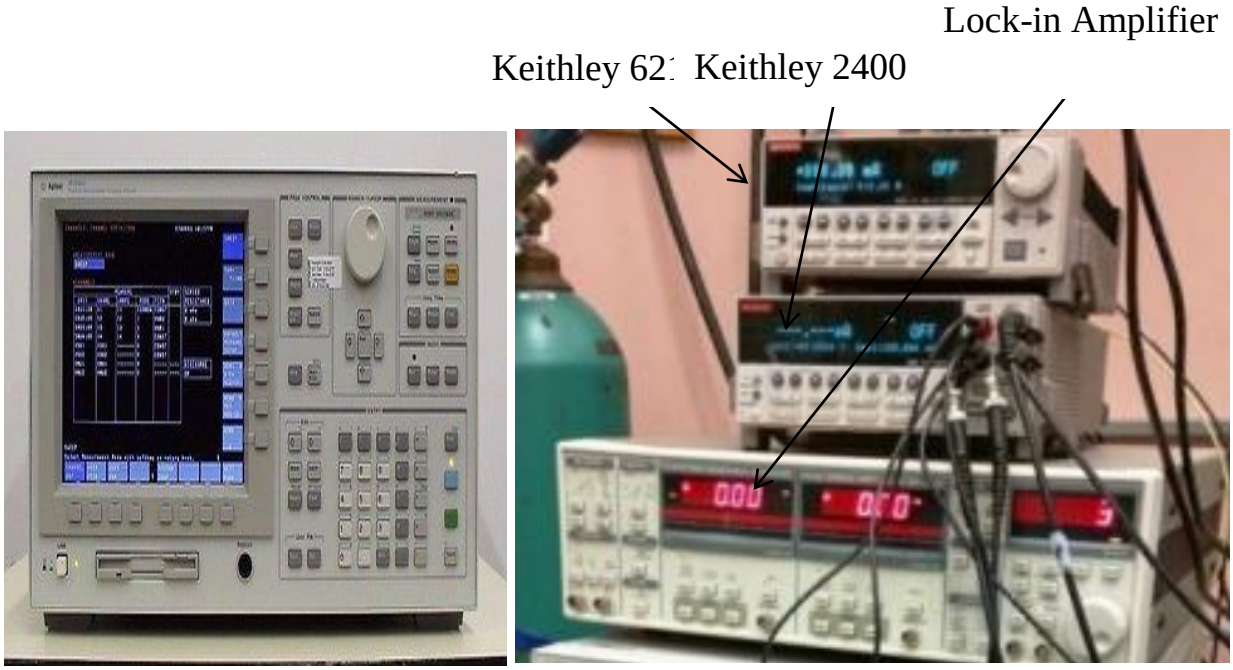

Figure 4.11: (a) Agilent 4156C Precision Semiconductor Parametric Analyzer (b) Keithley 621, 2400 and lock-in amplifier.

Device measurements are done by using a different set of measurement instruments based on the type of data we are looking for. We have used Semiconductor Parametric Analyzer (SPA), Lockin Amplifier SR830, Keithley 2400, Keithley 621, AC transport fitted with PPMS system. LabVIEW

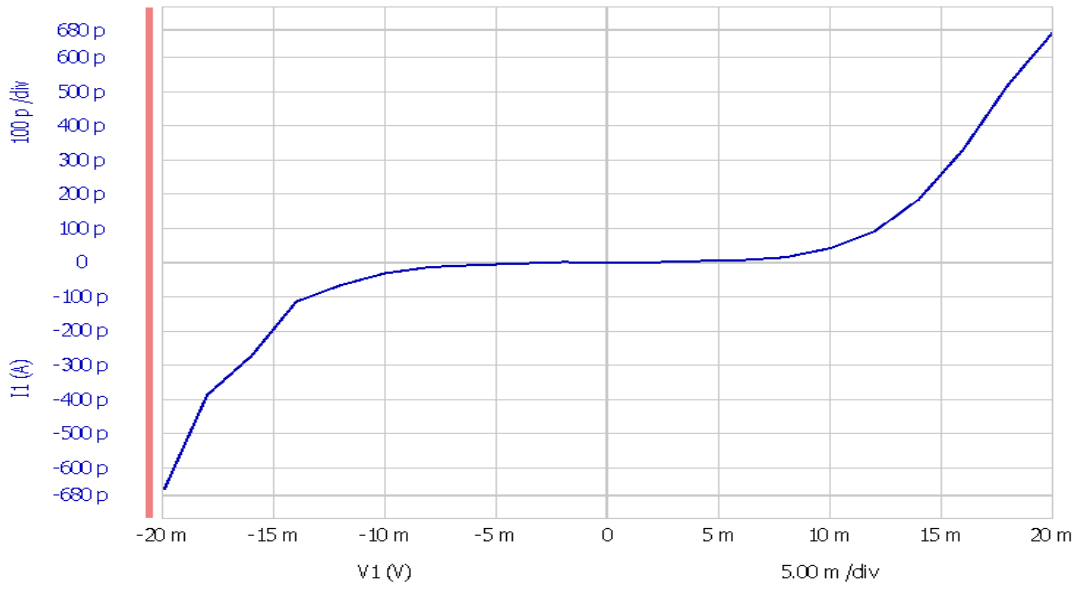

Figure 4.12: I-V characteristic of Te nanowire at room temperature measured using SPA.

software is used for interfacing all the measuring instruments to the PPMS. A SPA consists of voltage sources, current sources, voltage monitors, and current monitors, which can be programmed via a menu-driven user interface. A SPA is very useful for characterizing semiconducting devices. It can measure I-V characteristics and gate voltage (V_g) dependent measurements of nanoscale devices. In this project, we have used Agilent 4156C Precision SPA (shown in **figure 4.11**) which provides four source monitor units, two voltage sources, and two voltage monitors. I-V characteristic of a Te nanowire device is shown in **figure 4.12**. The other parameters like temperature and magnetic fields are controlled my PPMS. Keithley 2400 is used for four probe temperature dependence of conductivity measurements **(figure 4.13).**

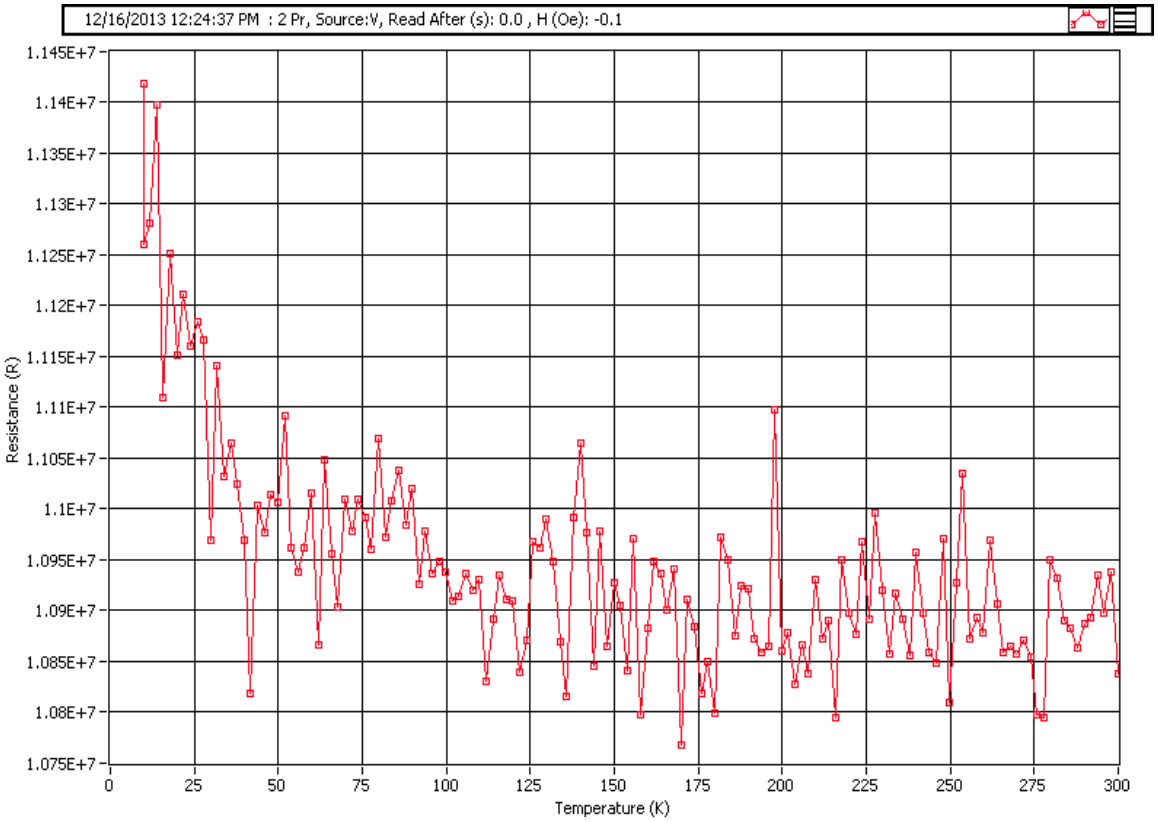

Figure 4.13: Temperature dependent conductivity of Te nanowire measured using a Keithley 2400.

Bibliography

[1] http://www.jcnabity.com

[2] D. M. Mattox, *Handbook of physical vapor deposition (PVD) processing*. William Andrew, 2010.

[3] B. Jugdersuren, *Growth and Characterization of Ferromagnetic Nanostructures for Device Application*. Phd thesis, The Catholic University of America, 2009.

[4] Agilent Technologies 4156C Semiconductor Parameter Analyzer Manual http://www.home.agilent.com/agilent/product.jspx?pn=4156C

Chapter 5: Transport Properties of Cobalt Telluride Nanostructures

In this chapter, we are going to describe the transport properties of cobalt telluride CoTe nanostructures. The discussion will start from the synthesis and characterization of the nanostructures. We have used wet-chemical synthesis to grow the nanostructures, followed by morphological, structural, magnetic and optical characterizations. We have measured the electrical and magneto-transport properties form single nanostructure nanodevices, fabricated using e-beam lithography.

5.1 Introduction

Recently, tellurium-based compounds have been extensively studied because of their unique and interesting properties, which are especially useful in thermoelectricity, spintronics, photonics and in topological insulators [1-5]. In tellurium compounds, cobalt tellurides are interesting because they exhibit both semiconducting and ferrimagnetic behavior [6]. The Curie temperature of nearly stoichiometric CoTe is reported to be around 1275 K [6-13]. Cobalt telluride crystallizes in the NiAs structure, where cobalt and tellurium each have octahedral and trigonal prismatic coordination, respectively. This structure is commonly subjected to non-stoichiometry. Thus, we can alter the Co and Te ratio and tune the semiconducting and magnetic properties. Uchida observed that the $CoTe_x$ with $x>1.2$ shows paramagnetic behavior. But for $1<x<1.2$, as x increases from 1, magnetization gradually decreases and becomes zero when $x = 1.2$. For $x>1.2$, it exhibits weak paramagnetism, which is independent of temperature. In bulk CoTe, it was observed that the

ferrimagnetism with near stoichiometry arises due to the presence of antiparallel alignment of cobalt spins in different layers of the crystal structure. The reported saturation magnetization was 0.25 Bohr magnetons per cobalt atom [6]. The recent report on CoTe nanostructures has shown that they exhibit magnetic hysteresis only below 2 K [9]. In this experiment we have followed a wet chemistry route for the growth of CoTe nanostructures and have shown that they exhibit ferrimagnetic and p-type semiconducting behavior. We also measured magneto-transport of CoTe nanostructures. Partially this work has published in a peer reviewed journal [14].

5.2 Experimental Methods and Materials

In a typical synthesis, 0.1 g of polyvinylpyrrolidone was dissolved in ethylene glycol (36 ml), followed by the addition of 0.24 g of α-TeO_2 powder, 0.3 ml of hydrazine, and 0.3 g of sodium hydroxide as a surfactant. All of the reagents used are of the highest purity available and were obtained from Alpha Aesar and Sigma Aldrich. The resulting solution was transferred to a three-necked flask fitted with a reflux condenser and a thermometer and de-aerated by N_2 bubbling at 5cc/s. The solution in the flask was heated to a temperature of 433 K for 1 h, forming tellurium nanostructures. After 1 h, the solution was cooled to room temperature and the required amount of cobalt nitrate precursor was added. The temperature was then raised to 523 K and maintained for 2 h to complete the reaction and to form CoTe nanostructures. In the second step, the cobalt ions diffuse into tellurium nanowires to form CoTe nanostructures. The mechanism of the growth was discussed by Zhang et al [15]. The synthesized products were collected by a high-speed centrifugation, washed several times with ethanol and acetone, and finally dried at 373 K for 10 h in an oven. The morphology of the nanostructures was analyzed using a scanning electron microscope (SEM) (JEOL JSM-5910V); the crystal structure was investigated by x-ray diffraction

(XRD) (Thermo/ARL X'TRA, Cu-K_α) and transmission electron microscope (JEM 2100 FEG TEM/STEM); the magnetic measurements were carried out using a vibrating sample magnetometer (VSM - Quantum Design); and the electrical transport properties were measured using a Quantum Design physical property measurement system. The UV-Visible spectrophotometry measurements were carried out using a Perkin Elmer spectrophotometer. For the measurement, CoTe nanowires were dispersed in isopropyl alcohol and were scanned with a variable wavelength (λ) source from UV to the visible region and the absorption coefficient was measured. 5.3 Results and Discussion

5.3.1 Morphology and Characterization

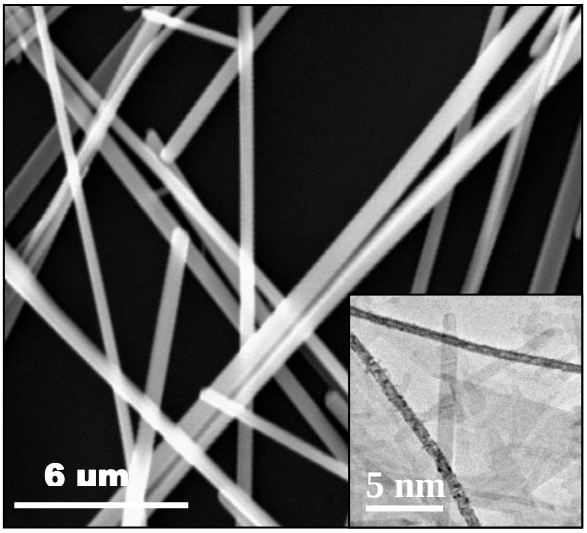

Figure 5.1: Scanning electron microscopy image of CoTe nanowires. The inset shows the TEM image of polycrystalline CoTe wires.

The scanning electron microscopy image in **figure 5.1** shows the formation of CoTe nanowires and nanoribbons during the growth. The diameter ranges from 50-300 nm and the length extends up to 50 µm. The inset of **figure 5.1** displays the morphology of CoTe nanostructures obtained

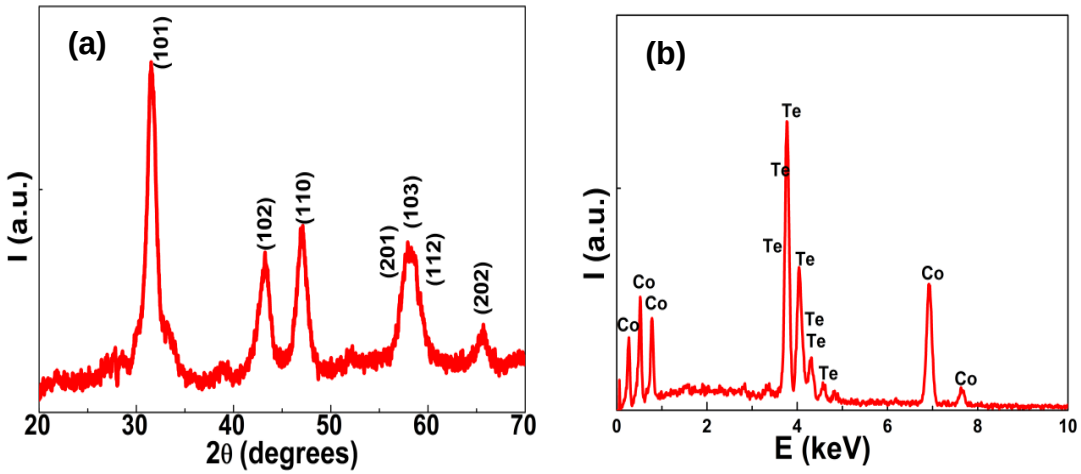

Figure 5. 2: (a) The XRD pattern and (b) EDX spectrum of CoTe nanostructures.

from transmission electron microscopy. The CoTe nanostructures are polycrystalline in nature. **Figure 5.2 (a)** shows the X-ray diffraction pattern of CoTe nanostructures. All of the peaks can be indexed with the NiAs hexagonal crystal structure with a space group of P63/mmc, and with lattice parameters *a*=3.893 Å and *c*= 5.375 Å [6]. The energy dispersive x-ray (EDX) spectrum (**figure 5.2** (**b)**) obtained using the scanning electron microscope shows that cobalt and tellurium are nearly in the ratio 1:1 in these nanostructures. **Figure 5.3 (a)** shows the high-resolution transmission electron microscopy lattice images of CoTe nanostructure. The observed lattice fringes correspond to (101) planes of the hexagonal crystal lattice. The selected area electron

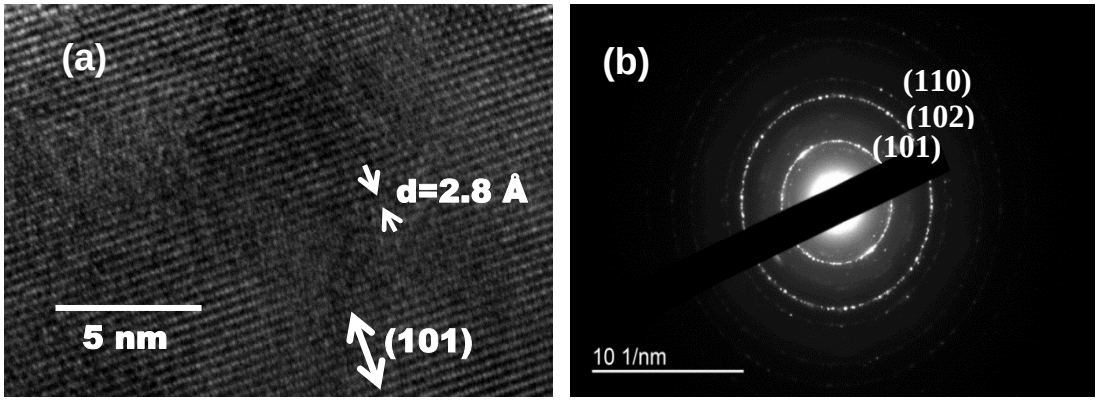

Figure 5.3: (a) High resolution TEM image displaying the lattice fringes. (b) Selected area electron diffraction pattern of CoTe nanostructures.

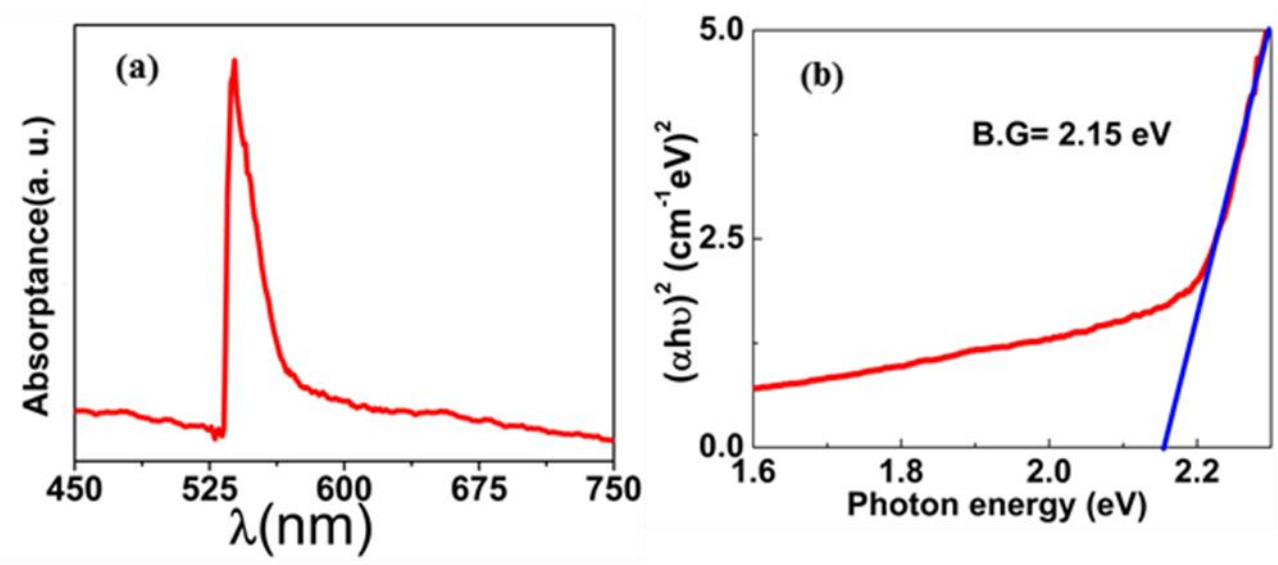

Figure 5.4: Optical measurement to calculate band gap.

diffraction pattern in Figure 5.3(b) displays the polycrystalline nature of CoTe nanostructure. The rings in the pattern can be indexed with (hkl) values (101), (102), and (110). In order to understand the optical properties of CoTe nanostructures, UV-Visible spectrophotometry measurements were carried out as shown in **figure 5.4 (a).** The Tauc model was used to extract the band gap from the absorption spectrum [16]. According to this model, a plot of $(\alpha h\nu)^2$ vs photon energy was generated as shown **figure 5.4 (b**). The α is the absorption coefficient and ν is the frequency of the photons and h is the Planck constant. A straight-line is fitted to the linear region of the curve and the x-intercept is used to calculate the band gap which is 2.15 eV.

5.3.2 Electrical and Magnetic Transport

In order to understand transport properties of the nanostructures, we have fabricated nanoscale CoTe devices using electron beam lithography [17]. We have used Si (100) substrates with a 50 nm SiO_2 layer as the substrates for the device fabrication. The fabrication procedure was presented

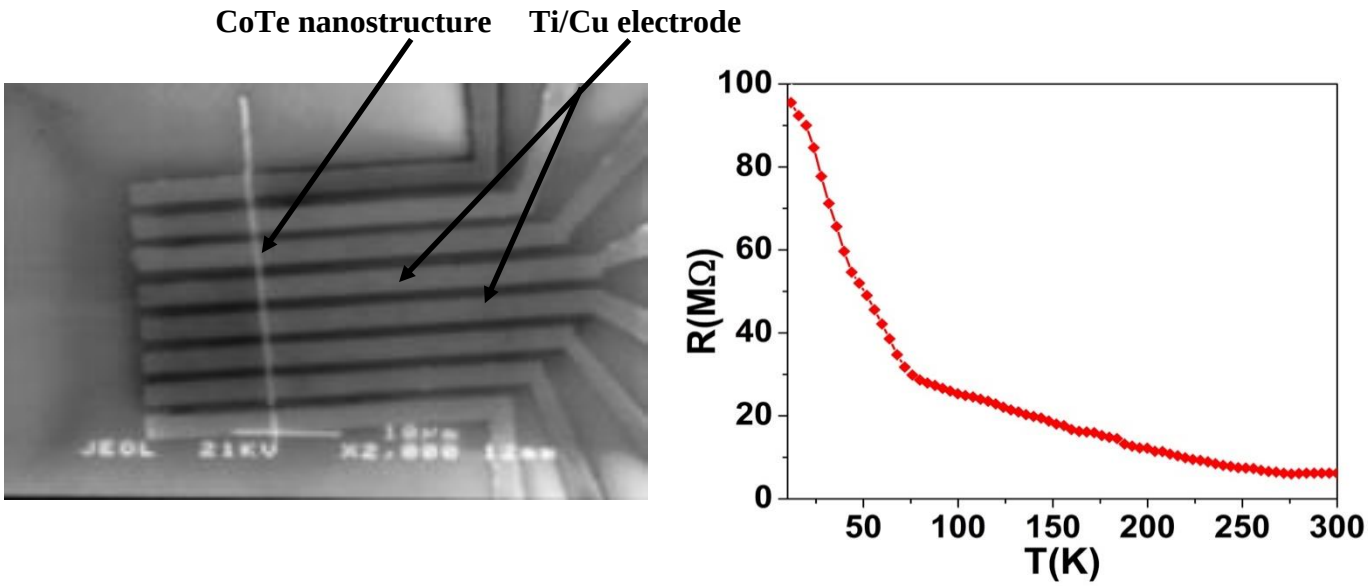

Figure 5.5: (a) SEM image of CoTe nanostructure (b) Temperature dependence of resistance of CoTe nanostructure.

in Ref. 17. We have deposited 80 nm of titanium (5 nm) and cobalt (75 nm) as electrodes using an ultra-high vacuum (base pressure $1x10^{-9}$ torr) deposition chamber. A typical image of a CoTe nanoscale device is shown in **figure 5.5 (a).** The electrical transport properties of the CoTe nanostructure are shown in **figures 5.5 (b**), **5.6 (a)** and **5.6 (b)**. Temperature dependence of resistance is shown in **figure 5.5 (b).** We can clearly observe non-metallic electrical properties of CoTe nanostructure from room temperature to 10 K. This non metallic behavior is because of semiconducting nature of the nanostructure which will be strongly supported by further

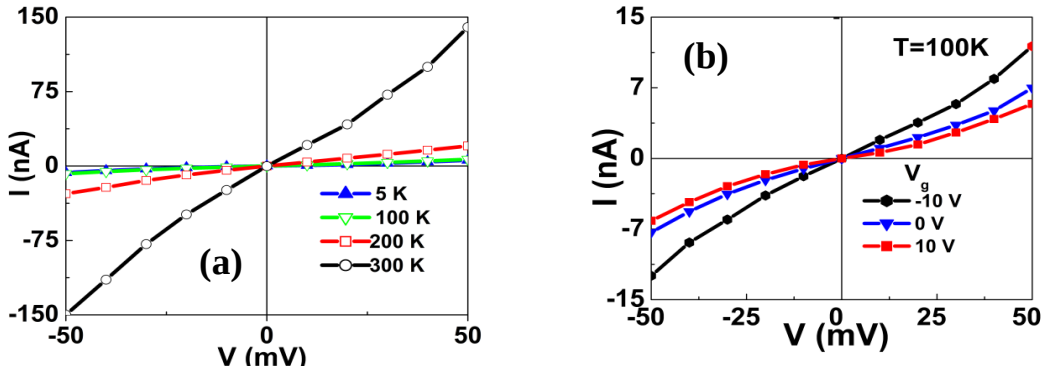

Figure 5.6: (a) Current-voltage characteristics of CoTe device at different temperatures. (b) The gate voltage dependence on the current-voltage characteristics at 100 K.

measurements. **figure 5.6 (a**) shows the typical current-voltage characteristics from room temperature to 5 K. The current decrease significantly as the temperature is lowered to 5 K and it is nonlinear as a function of the applied voltage. **figure 5.6 (b)** shows the current-voltage characteristics with varying gate voltages at 100 K. A back gate is used to apply the gate voltage. We have observed that for a particular bias voltage, V, the current increases with increasing negative gate voltage, which is the characteristics of a p-type semiconductor. Thus the CoTe nanostructures exhibit a p-type semiconducting behavior which also supports the optical band gap data presented earlier. Magnetic transport properties have shown in figure 5.7. Magnetoresistance (MR) is calculated with filed dependence I-V measured at different temperatures. We present MR at different temperatures with the expression

$$\%MR = \frac{[R(H) - R(0)]}{R(0)} x100 \qquad 5.1$$

Resistance is calculated at the biasing voltage 0.4 V. We have obtained MR only below 50 K temperature. More than 50% MR effect has noticed at 10 K. **Figure 5.7 (b**) shows %MR with temperature below 60 K.

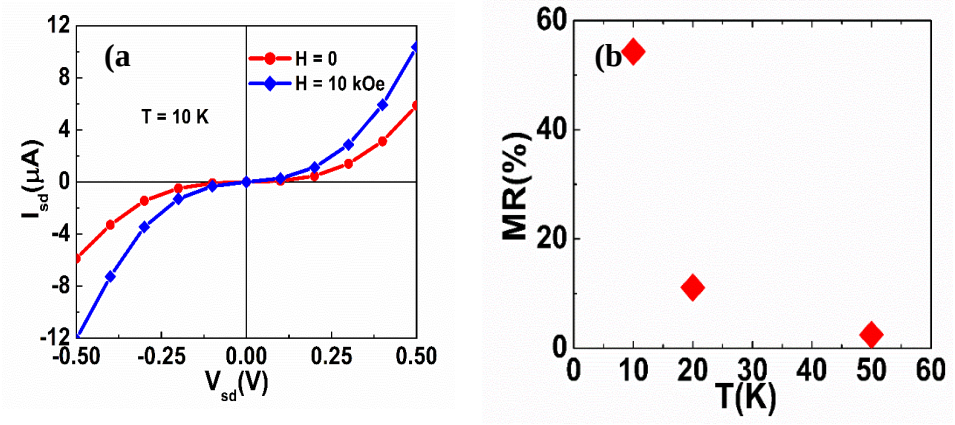

Figure 5.7: (a) Field dependent current –voltage measurement (b) Percentage MR with temperatures.

5.3.3 Magnetic Properties

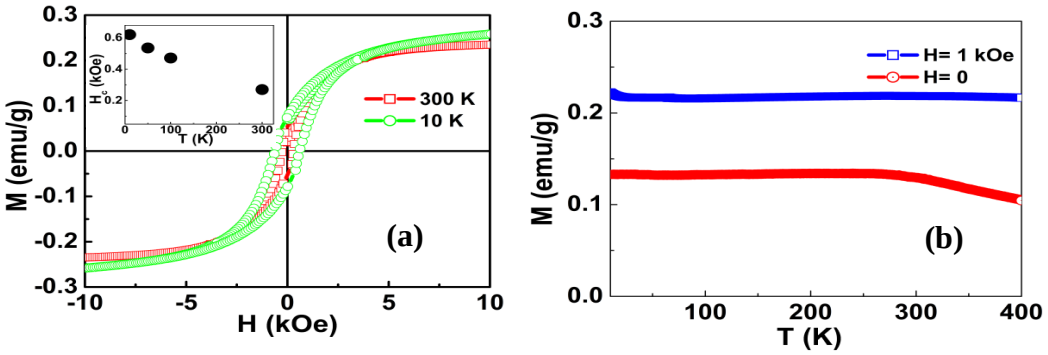

Figure 5.8: (a) M vs H curves of CoTe nanostructures at 10 and 300 K. (b) The magnetization as a function of temperature with zero field and with a field of 1 kOe.

For the magnetic characterization, CoTe nanostructures were dispersed on to a clean silicon (100) substrate. The external field was applied parallel to the plane of the substrate. The background was corrected for all magnetic measurements. **Figure 5.8 (a)** shows the M-H curves of CoTe nanostructures from temperatures 10 – 300 K. The coercivity increases with a decrease in temperature. The coercivity change from 10 to 300 K is shown in the upper inset of **figure 5.8 (a).** **Figure 5.8 (b)** shows the temperature dependence of magnetization of CoTe nanowires. The M-T curve shows that the Curie temperature of the system is much higher than 400 K consistent with the bulk behavior [6]. The calculated saturation moment of CoTe is $0.2\mu_B$/Co atom which is low if all of the the cobalt ions have +2 oxidation state [7] and they are ferromagnetically coupled in the lattice. In NiAs-type Fe_7S_8, it was shown that the observed magnetic moment is much lower than the expected moment. The magnetic behavior of Fe_7S_8 has been attributed to ferromagnetic alignment of cations within layers and antiferromagnetic coupling between adjacent layers of the NiAs structure with an uncompensated total moment, leading to ferrimagnetism [19]. The low saturation moment in CoTe may arise due to the fact that the cobalt moments in different layers of

the hexagonal structure are coupled antiparallel, without completely cancelling the moment yielding a net moment of 0.2 μ_B/Co atom.

5.4 Conclusions

We have grown CoTe nanostructures using a wet chemical method. They are crystalline in NiAs hexagonal crystal structure. We have completely analyzed magnetic behaviors and found that they show ferrimagnetic nature well above room temperature, as reported on bulk CoTe. We have analyzed electrical and magnetic transport properties from single nanostructure nanodevice fabricated using e-beam lithography. We have found that CoTe possessed p-type semiconducting nature which is supported by multiple measurements. We noticed ordinary magnetoresistance below 50 K and found more than 50% MR effect is at 10 K.

Bibliography

[1] E. E. Foos, R. M. Stroud, and Alan D. Berry, Synthesis and characterizartion of nanocrystalline bismuth telluride, Nano Lett. **1**, 693 (2001).

[2] M. B. Kanoun, W. Sekkal, H. Aourage, G. Merad, Molecular-dynamics study of the structural, elastic and thermodynamic properties of cadmium telluride, Phys. Lett. A **272,** 113 (2000).

[3] B. Q. Liang, X. Chen, Y. J. Wang, and Y. J. Tang, Abnormal magnetoresistance effect in self-doped $Ag_{2+}\delta Te$ thin films($\delta < \sim 0.25$), Phys. Rev. B **61**, 3239 (2000).

[4] H. S. Schnyders, M. –L. Saboungi, and T. F. Rosenbaum, Magnetoresistance in n-and p-type Ag_2Te: Mechnisms and applications, Appl. Phys. Lett. **76**, 1710 (2000).

[5] H. Zhang, C.-X Liu, X.- L Qi, X. Dai, Z. Fang, and S.- C. Zhang, Topologial insulators in Bi_2Te_3 and Sb_2Te_3 with a single Dirac cone on the surface, Nat. Phys. **5**, 438 (2009).

[6] E. Uchida, Magnetic properties of cobalt telluride, J. Phys. Soc. Jpn. **10**, 517 (1955).

[7] H. Fan, Y. Zhang, M. Zhang, X. Wang, and Y. Qian, Glucose-assisted synthesis of CoTe nanotubes in situ templated by Te nanorods, Cryst. Growth Des. **8**, 2838 (2008).

[8] Q. Peng, Y. Dong, and Y. Li,Synthesis of uniform CoTe and NiTe semiconductor nanocluster wires through a novel coreduction method, Inorg. Chem. **42**, 2174 (2003).

[9] R. Shi, X. Liu, Y. Shi, R. Ma, B. Jia, H. Zhang, and G. Qiu, Selective synthesis and magnetic properties of uniform CoTe and $CoTe_2$ nanotubes, J. Mater. Chem. **20**, 7634(2010).

[10] N. Umeyama, M. Tokumoto, S. Yagi, M. Tomura, K. Tokiwa, T. Fujii, R. Toda, N. Miyakawa, and S.- I. Ikeda, Synthesis and magnetic properties of NiSe, NiTe, CoSe, and CoTe, Jpn. J. Appl. Phys. **51**, 053001 (2012).

[11] L. Jiang and Y.- J. Zhu, A general solvothermal route to the synthesis of CoTe, Ag_2Te/Ag, and CdTe nanostructures with varied morphologies, Eur. J. Inorg. Chem. **2010**, 1238 (2010).

[12] M. Muhler, W. Bensch, and M Schur, Prepration, crystal structures, experimental and theoretical electronic band structuresof cobalt telluride in the composition range, J. Phys. Condens. Mat. **10**, 2947 (1998).

[13] J. Guo, Y. Shi, Y. Chu, and T. Ma, Highly efficient telluride electrocatalysts for use as Pt-free counter electrodes in dye-sensitized solar cells, Chem. Commun. **49**, 10157 (2013).

[14] B. R. Dahal, R. P. Dulal, I. L Pegg, and J. Philip, Electrical Transport and magnetic properties of cobalt telluride nanostructures, J. Vac. Technol, B **34**, 051801 (2016).

[15] H. Zhang, D. Yang, Y. Ji, X. Ma, J. Xu, and D. Que, Selenium nanotubes synthesized by novel solution phase approach, J. Phys. Chem. B **108**, 1179 (2004).

[16] M. Meinert, and G. Reiss, Electronic structure and optical band gap determination of $NiFe_2O_4$, J. Phys: Cond -Mat. Sci **26**, 115503(2014).

[17] B. Jugdersuren, S. Kang, R. S. Dipietro, D. Heiman, D. Mckeown, I. L. Pegg, and J. Philip, Large low field magnetoresistance in $La_{0.67}Sr_{0.33}MnO_3$ nanowire devices, J. Appl. Phys. **109**, 016109(2011).

[18] A. V. Powell, P. Vaqueiro, K. S. Knight, L. C. Chapon, and R. D. Sanchez, Structure and magnetism in synthetic pyrrhotite Fe_7S_8: A powder neutron-diffraction study, Phys. Rev. B **70,** 014415(2004).

Chapter 6: Ferrimagnetic $Co_{1+\delta}Te$ Nanostructures

In previous chapter, we have discussed the crystal structure, magnetic properties, electrical and magneto transport properties of nearly stoichiometric CoTe nanostructures synthesized using wet-chemistry method. In this chapter, we describe the growth structural magnetic and transport properties of Co excess CoTe nanostructures synthesized using the solvothermal method. We have observed that the excess Co alters the crystal structure, magnetic behavior and transport properties. This work has been partially published in Material Research Express journal [1].

6.1 Introduction

Cobalt tellurides are interesting compounds because of their variable crystal phases, unusual magnetic properties and semiconducting behaviors [2-9]. The nearly stoichiometric CoTe crystallizes in hexagonal NiAs-type crystal structure with a ferrimagnetic behavior [10], [11]. The saturation magnetic moment is 0.25 μ_B/Co and with a high curie temperature 1275 K. Compounds with excess tellurium as in $CoTe_x$, with $1<x<1.2$ maintain the same NiAs-type hexagonal crystal structure [10]. But with $x>1.2$, the crystal structure changes to CdI_2-type crystal structure and exhibit paramagnetism. Muhler et. al; have shown the crystal transformation as x varies from x= 1.3 to x= 2, unstable trigonal CdI_2 crystal structure changes to orthorhombic structure with the lattice being more stable but the ferrimagnetic behavior changes to paramagnetic phase [5]. These $CoTe_2$ compounds are also a center of interest for research because of their efficient and robust catalytic approach for hydrogen evolution [12]. We have recently reported the magnetic and

electric properties of nearly stoichiometric CoTe nanostructures [11]. We have found CoTe nanostructures show p-type semiconducting behavior and they are ferrimagnetic with a saturation magnetization of 0.2μ_B/Co atom. Here we report the growth and characterization of $Co_{1+\delta}Te$ (δ = 0.27) nanostructures for the first time. The excess Co in CoTe transforms the NiAs-type crystal structure to filled NiAs type crystal phase commonly known as hexagonal Ni_2In type crystal structure but belonging to the same space group, p63/mmc. The additional Co atoms in $Co_{1+\delta}Te$ fills the holes above and below the tellurium sites in a unit cell. We have investigated the electrical and magnetic properties of these nanostructures.

6.2 Experimental Methods and Materials

$Co_{1+\delta}Te$ nanostructures were grown using solvothermal synthesis route. In a typical synthesis, 0.5 g of high-purity polyvinylpyrrolidone (PVP was dissolved in deionized water (20 ml), followed by 0.083 g of Na_2TeO_3 powder, 0.6 ml of hydrazine, and 0.5 ml of NH_4OH as a surfactant. All of the reagents used are of the highest purity available and were obtained from Alpha Aesar and Sigma Aldrich. The resulting solution was transferred to an autoclave and stirred for 12 h to make a homogeneous solution and then it was heated at 450 K for 12 h to obtain Te nanostructures. Then Co precursor, $Co(NO_3)_2.6H_2O$ is injected to the grown Te nanostructures and heated for another 6 h at 450 K on the same autoclave. The synthesized products were collected by a high-speed centrifugation, washed several times with ethanol, and finally dried at 373 K for 10 h in an oven in argon ambient. The morphology of the nanostructures was analyzed using a scanning electron microscope (SEM) (JEOL JSM-5910V); the crystal structure was investigated by x-ray diffraction (XRD) (Thermo/ARL X'TRA, Cu-K_α) and transmission electron microscope (JEM 2100 FEG TEM/STEM); the magnetic measurements were carried out using a vibrating sample

magnetometer (VSM - Quantum Design); and the electrical transport properties were measured using a Quantum Design physical property measurement system (PPMS).

6.3 Result and Discussions

6.3.1 Morphology and Structural Characterization

The scanning electron microscopy image in **figure 6.1** shows the morphology of the $Co_{1+\delta}Te$

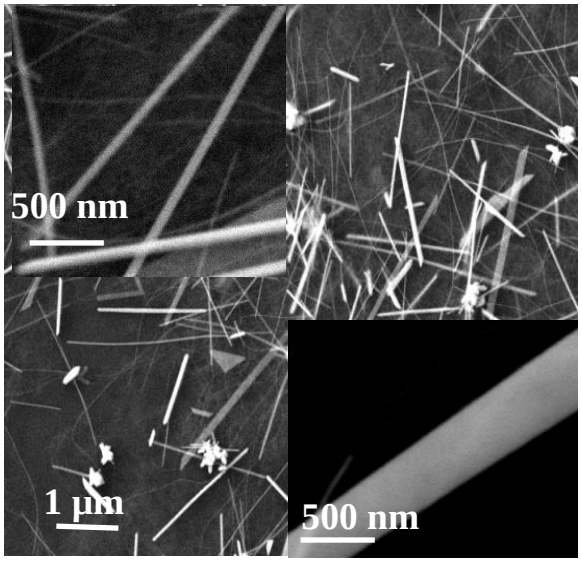

Figure 6.2: The SEM images of $Co_{1+\delta}Te$ nanostructures.

nanostructures. We have observed a large variation in the width of the nanostructures, which

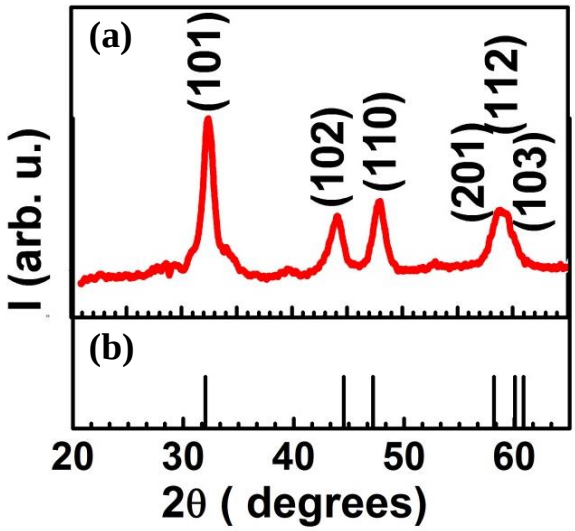

Figure 6.1: (a) XRD pattern of $Co1_{+\delta}Te$ nanostructures (b) Calculated pattern for Ni2In type Co1+δTe structure.

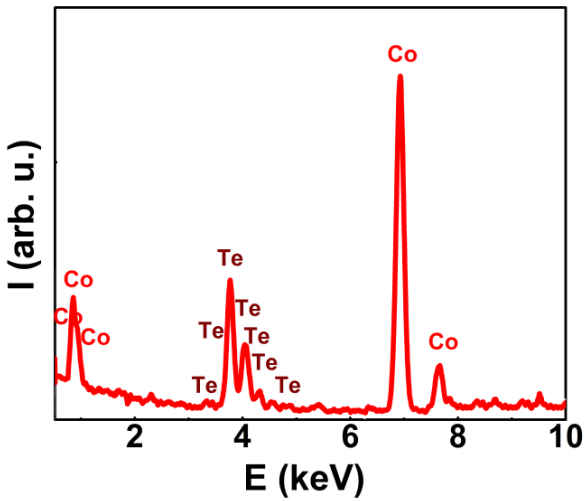

Figure 6.3: EDX spectrum of $Co_{1+\delta}Te$ nanostructures.

varies from 50 - 500 nm and the length varies from 50 - 100 µm. The lower inset shows the wider nanostructures and the upper inset shows nanostructures with width less than 150 nm. The X-ray diffraction pattern of $Co_{1+\delta}Te$ nanostructures is shown in **figure 6.2.** All of the peaks can be indexed with hexagonal Ni_2In crystal structure with the space group P63/mmc and with lattice parameters $a = b$=3.85 *Å*, and c = 5.131 *Å*. The c/a is nearly 1.3 which corresponds to a cobalt rich CoTe system [12]. The excess Co atoms are responsible for the crystal transformation from NiAs-type to Ni_2In type crystal structure. Atomic positions in NiAs- and Ni_2In-types CoTe crystal structure is shown in **figure 6.3**. The additional Co atoms fills the holes above one of the arsenic sites and below the other arsenic sites in a unit cell as shown in **figure 6.3** [13]. Qualitative elemental analysis was performed using Energy Dispersive X-ray Spectroscopy (EDX) using JEM 2100 FEG TEM/STEM. We did EDX analyses (**figure 6.4**) on different batch of samples and obtained consistent results. Based on several EDX analyses, we have confirmed that the cobalt telluride nanostructures obtained from hydrothermal synthesis have Co and Te in the ratio 56:44

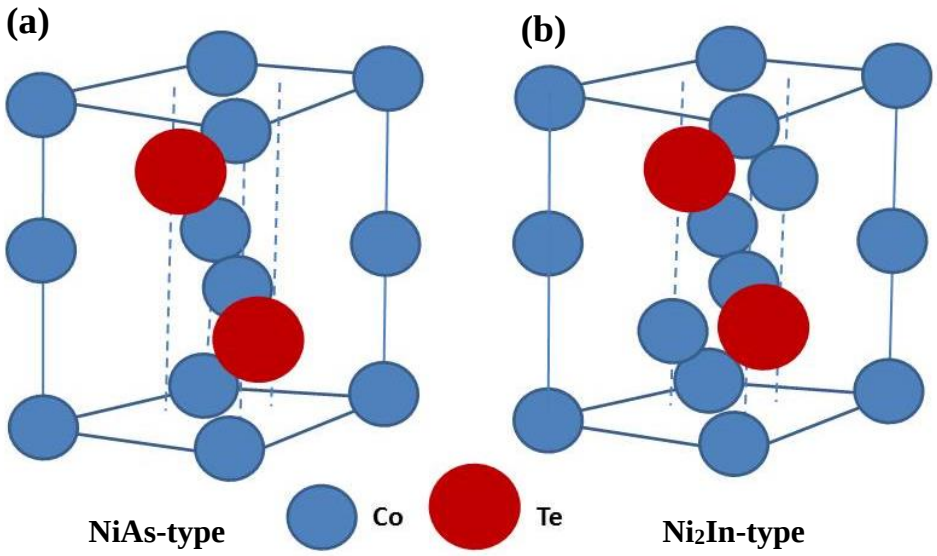

Figure 6.4: (a) NiAs-type and (b) Ni2In-type crystal structures.

uniformly across the nanostructures. Therefore, $Co_{1+\delta}Te$ nanostructures have formed with δ = 0.27.

6.3.2 Magnetic Properties

Magnetic properties of $Co_{1+\delta}Te$ are displayed in **figure 6.5**. The background was corrected for all magnetic measurements. The hysteresis loops of $Co_{1+\delta}Te$ measured at 3-50 K from the same sample are shown in **Figure 6.5 (a)**. We have observed that a magnetic transition from paramagnetism to ferrimagnetism occurred at around 40 K. The calculated saturation moment of $Co_{1+\delta}Te$ is 0.6μ_B/Co atom at 3 K, which is higher than the stoichiometric CoTe nanostructures [11]. The coercivity, H_c of the system decreases exponentially with the increasing temperature from 3 - 50 K. The variation of the coercivity with temperature is found to follow an exponential relation: $H_c(T) = H_c(0)\, e^{-\beta T}$ where $H_c(0)$ is the coercivity at 0 K and β is a constant. From the fit of this equation to the experimental data (inset Figure. 5(b)) yields $H_c(0)$ = 5.53 kOe and the constant β as 0.008 K^{-1} [17]. At 3 K, H_c is 4.90 kOe with a saturation magnetization of 10.03

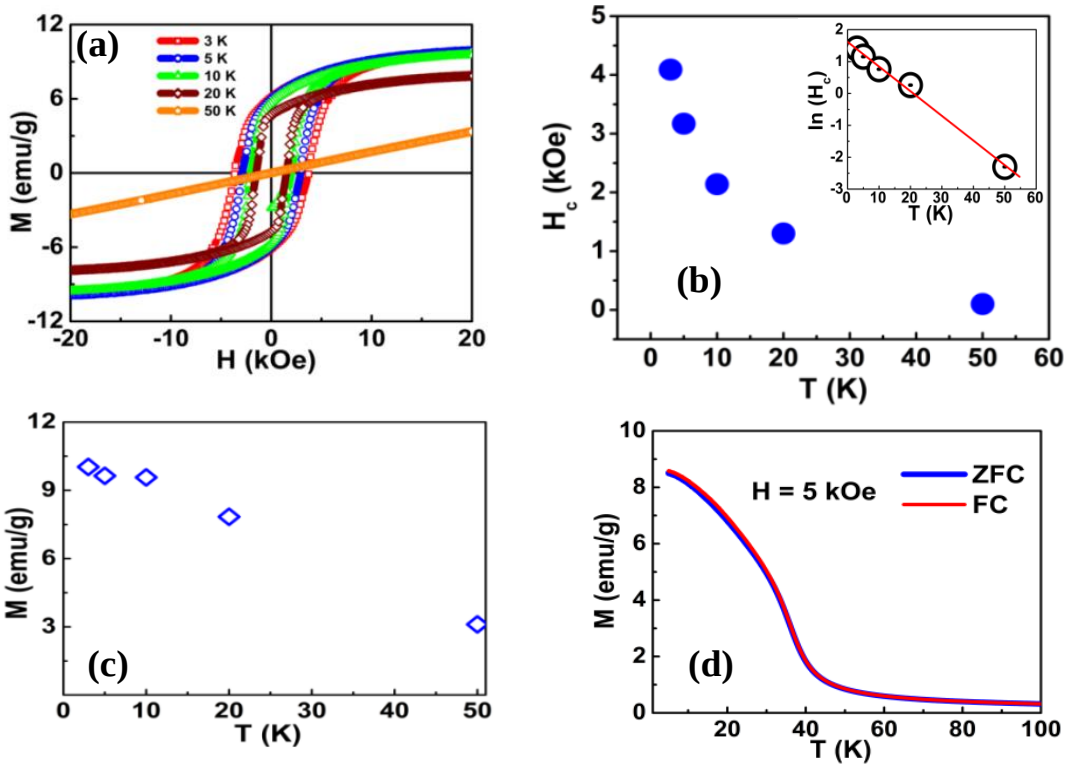

Figure 6.5: Magnetic measurements of $Co_{1+\delta}Te$ nanostructures (a) M-H curves at different temperatures, (b) temperature dependence of coercivity (inset shows the exponential fitting) (c) temperature dependence of saturation magnetizations and (d) temperature dependence of magnetization at ZFC and FC.

emu/g. There are two significant features observed in the coercivity of the $Co_{1+\delta}Te$ system. First, extremely high H_c values indicating hard ferrimagnetic behavior at low temperature as shown in **figure 6.5 (a)** and the second feature is the rapid variation of H_c with the decrease in temperature as shown in **figure 6.5 (b)**. We have calculated the remanence ratio (M_r/M_s) from M-H curves shown in **figure 6.5 (a)** at different temperatures. At 3 K, the remanence ratio is 0.56, which is approaching the critical boundary for single domain [18], [19]. With increasing temperature, the remanence ratio goes on increasing indicating the higher interaction on the domain walls, corresponding to the decreasing H_c until the transition temperature. Rapid variation of H_c with the temperature is attributed to the lower mean diameter of the nanostructures. Temperature dependence of magnetization of $Co_{1+\delta}Te$ nanostructures with zero field cooled (ZFC) and field

cooled (FC) are shown in **figure 6.5 (d)**. For an applied field 5 kOe, we have observed that both ZFC and FC curves coincide indicating a reversible magnetization behavior and absence of super paramagnetic phases. This reversible magnetization implies the formation of hard ferrimagnetic $Co_{1+\delta}Te$ nanostructures below the transition temperature. The ferrimagnetic transition temperature (T_c) is around 40 K, which agrees well with the M-H measurements as shown in Figure 6.5(a).

6.3.3 Electrical and magneto-transport properties

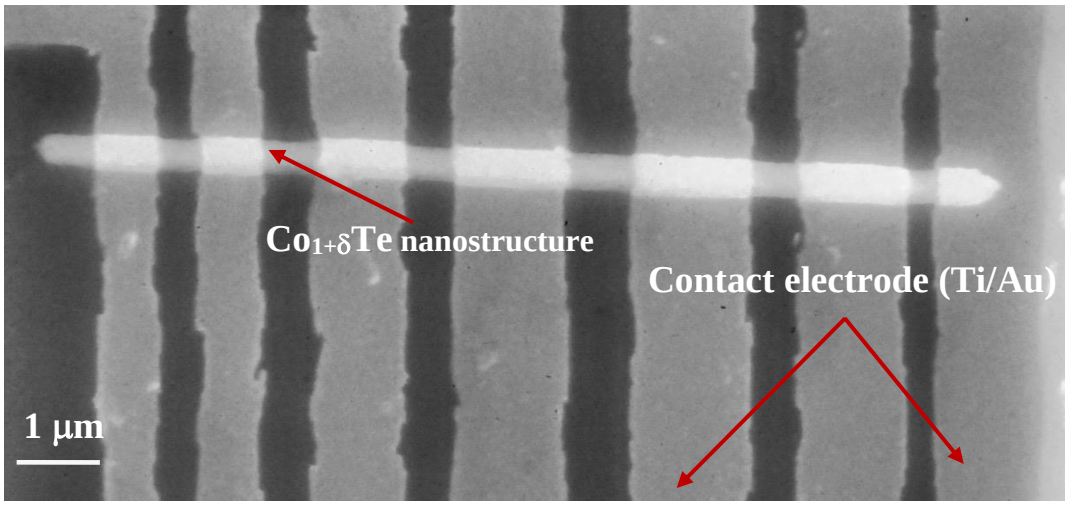

Figure 6.6: SEM image of $Co_{1+\delta}Te$ nanodevice.

We have used Si (100) with a 500 nm of SiO_2 layer as substrates for the device fabrication. We have deposited 80 nm thick electrodes of titanium (10 nm) and gold (70 nm) using an ultra -high vacuum (base pressure $1x10^{-9}$ torr) system [20]. SEM image of nanodevice is shown in **figure 6.6**. The fabrication procedure was presented in Ref. 20. Temperature dependence of electrical resistivity of the nanostructures in the temperature range 10-300 K is shown in **figure 6.7 (a)**. The nanostructure used to measure electric resistivity has a width 200 nm and length 50 μm. It is clear that the resistivity of the nanostructure decreases with an increasing temperature. However, no Arrhenius behavior is observed in the measured temperature range (inset **figure 6.6 (a)**) indicating

that the experimentally measured resistivity curve does not follow the expected thermal excitation behavior for a semiconductor [20]. The variation of the electric resistance with temperature is well-fitted by using Mott's three dimensional variable range hopping (VRH) model described by the expression, R

$$R(T) = R_0 \exp\left(\frac{T_0}{T}\right)^{1/4} \qquad 6.1$$

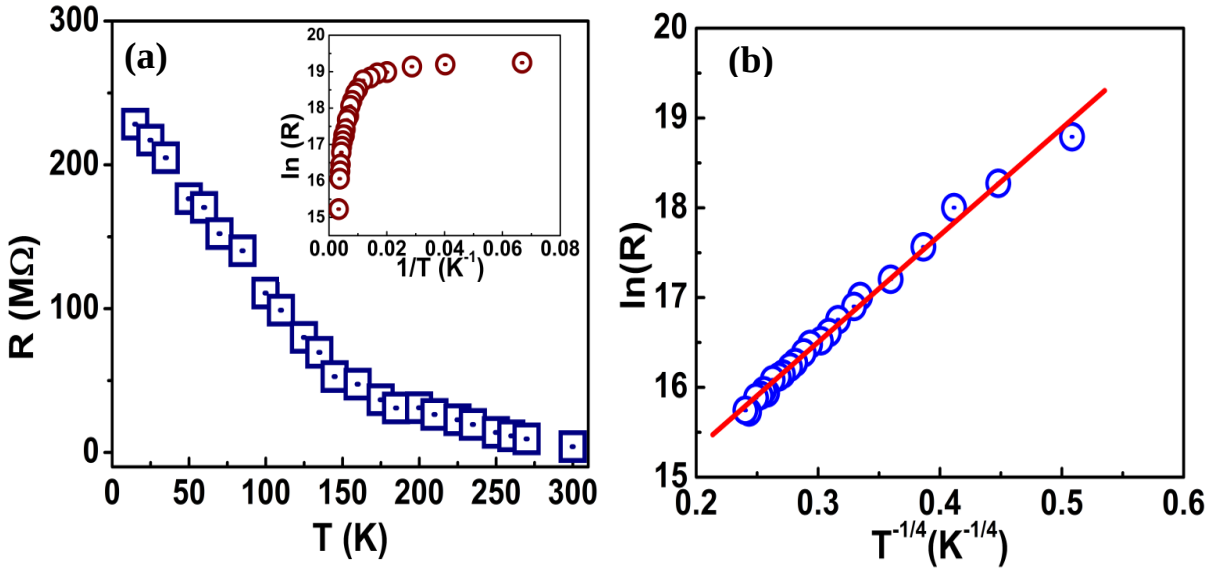

Figure 6.7: (a) Resistance of $Co_{1+\delta}Te$ as a function of temperature. The Inset shows the plot in terms of the thermal activation model (b) Resistance fitted (red solid line) to the Mott's three dimensional VRH model.

where, R_0 is the high temperature limit of resistance in Ω and T_0 is Mott's characteristic temperature in (Kelvin) [21-24]. Mott VHR hopping model suggests that $Co_{1+\delta}Te$ is a defect-rich system and also implies that the existence of localized states in the band gap and finite density of states at the Fermi energy. We have analyzed field dependence of resistance from the same nanodevice and calculated percentage magnetoresistance (MR) using equation (6.2) at various temperature. Maximum MR observed was 37% at the lowest measured temperature 10 K.

$$\%MR = \frac{R_0 - R_{H=5\ Oe}}{R_0} \times 100 \qquad 6.2$$

Here, we have noticed that, an application of H (say, 5k Oe) depresses the value of electric resistance, resulting a negative MR observed below 175 K, which is far above curie temperature ($T_c \approx$ 40 K,) as shown in **figure 6.5 (d)** [25].

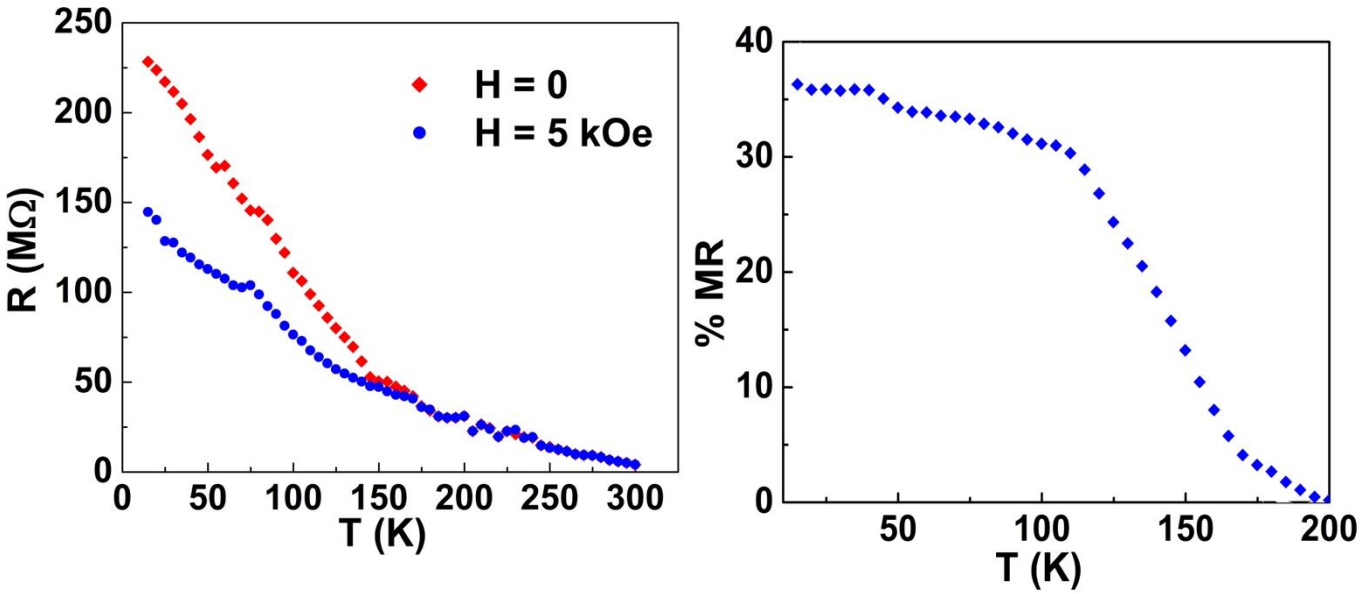

Figure 6.8: (a) Temperature dependence resistance at H= 0 and 5 Oe (b) Magnetoresistance measured at different temperatures.

6.4 Conclusions

We have grown $Co_{1+\delta}Te$ nanostructures for the first time using the solvothermal synthesis. They crystalize in a filled NiAs or Ni_2In-type hexagonal crystal structure. The nanostructures exhibit ferrimagnetic behavior with the saturation magnetization of 0.6 μ_B/Co atom. Interestingly, $Co_{1+\delta}Te$ nanostructures show the hard ferrimagnetic behavior below the transition temperature of 40 K. Both coercivity and saturation magnetization decrease with the increasing temperature and coercivity follows the exponential decay with increasing temperature. They exhibit

semiconducting behavior but do not follow the thermal excitation law for semiconductors. The variation of electric resistance with temperature is explained by Mott's three-dimensional variable range hopping model. We have observed negative magnetoresistance below 175 K but well above Curie temperature, which is as high as 37% at the lowest measured temperature of 10 K.

Bibliography

[1] B. R. Dahal, R. P. Dulal, I. L. Pegg, and J. Philip, Ferrimagnetic Co1+δTe nanostructures, Mater. Res. Express 3, 116101, 2016.

[2] Mills K C, Heat capacity of nickel and cobalt telluride, J. Chem. Soc., Faraday Trans. **70**, 2224-31, 1974.

[3] Peng Q, Dong Y, and Li Y, Synthesis of uniform CoTe and NiTe semiconductor nanocluster wires through a novel coeducation method, Inorg. Chem., **42,** 2174-75, 2003.

[4] Fan H, Zhang Y, Zhang M. Wang X, and Qian Y, Glucose- assisted of CoTe nanotubes in situ templated by Te nanorods, Cryst. Growth Des., **8,** 2838, 2008.

[5] Muhler M, Bensch W, and Schur M, preparation, Crystal structures, experimental and theoretical band structure of cobalt tellurides in the composition range $CoTe_{1.3}$-$CoTe_2$, J. Phys. Mater.,**10,** 2947-62, 1998.

[6] Xie Y, Li B, Su H, Liu X, and Qian Y, Solvothermal route to $CoTe_2$ nanorods Nanostruct. Mater. **11,** 539-44, 1999.

[7] Geffken R M, Komarek K L, and Miller E M, Thermodynamic properties of cobalt-telluride alloys, J. Solid State Chem., **4,** 153-62, 1972.

[8] Shi R, Liu X, Shai Y, Ma R, Jia B, Zhang H, And Qiu G, Selective synthesis and magnetic properties of uniform CoTe and $CoTe_2$ nanotubes, J. Mater. Chem., **20,** 7634-36, 2010.

[9] Khan M S, Ashiq M N, Ehsan M F, Controlled synthesis of cobalt telluride superstructures for the visible light photo-conversion of carbon dioxide into methane, Appl. Catal. A- Gen **487,** 202-9, 2014.

[10] Uchida E, Magnetic properties of cobalt telluride, J. Phys. Soc. Jpn. **10** 517, 1955.

[11] Dahal B R, Dulal R P, Pegg I L, and Philip J, Electrical transport and magnetic properties of cobalt telluride nanostructures, J. Vac. Sci. Technol. B, **34,** 5, 051801, 2016.

[12] Lu T-H, Chen C-J, Basu M, Ma C-G, and Liu R- S, The $CoTe_2$ nanostructures: an efficient and robust catalyst for hydrogen evolution, Chem. Commun., **51,** 17012, 2015.

[13] Lidin S, Larsson A K, A survey of superstructures in intermetallic NiAs-Ni2In- Type Phases, J. Solid State Chem. ,**118**, 313-22, 1995.

[14] Leineweber A, Oeckler O, Zachwieija U, Static atomic diplacements of Sn in disordered NiAs/Ni_2In type HT-$Ni_{1+\delta}$Sn, J So;id State Chem. **177,** 936-45, 2004.

[15] Ponten M E, Stenberg L, Larsson A K, Lidin S, and Stahl K, Three NiAs-Ni_2In type structures in Mn-Sn system, J Solid State Chem., **129** 231-41, 1997.

[16] Patterson A L, The Scherrer Formula for x-ray particle size determination, Phys Rev., **56,** 978-82, 1939.

[17] Karipoth P, Joseyphus R J, Magnetic properties of interacting CoPt, nanoparticles synthesized through polyol process, Mater. Chem. Phys. **154,** 53-59,2015.

[18] Xiao Q I, Thang P D, Bruck E, Boer F R, and Buschow H K J, *Effect of phase* transformation on remanence enhancement in bulk Fe–Pt magnets, Appl. Phys. Lett. **78,** 23, 3672-74, 2001.

[19] Sreeja V, Joy P A, Microwave–hydrothermal synthesis of γ-Fe2O3 nanoparticles and their magnetic properties Mater., Res. Bull. **42** 1570-76, 2007.

[20] Jugdersuren B, Kang S, Dipietro R S, Heiman D, Mckeown D, Pegg I L, and Philip J, Large low field magnetoresistance in $La_{0.67}Sr_{0.33}MnO_3$ nanowire devices, Appl. Phys. **109,** 016109, 2011.

[21] Yu P, and Cardona M, *Fundamentals of semiconductors*, Berlin: Springer, 1990.

[22] Li G, Zhang B, Rao J, Gonzalez D H, Blake G K, Groot R A, and. Palstra T T M, *Effect* of vacancies on magnetism, electrical transport, and thermoelectric performance of marcasite FeSe2−δ (δ = 0.05*)*, Chem. Mater. **27,** 8220-29, 2015.

[23] Paschoal W, Kumar S, Borschel C, Wu P, Canali C M, Ronning C, Samuelson L, and Pettersson H, Hopping conduction in Mn ion-implanted GaAs nanowires, Nano. Lett. **12**, 4838-42, 2012.

[24] Kundu A K, Seikh M M, Srivastava A, Maharjan S, Chatterjee R, Pralong V, and Raveau B, Incoherent effect of Fe and Ni substitutions in the ferromagnetic-insulator $La_{0.6}Bi_{0.4}MnO_{3+\delta}$, J. Appl. Phys. **110,** 073904, 2011.

[25] S. Majumdar, R. Malik, and E. V. Sampathkumaran, Magnetic behavior: Large negative magnetoresistance above the curie temperature, Phy. Rev. B, **60**, 9, 1999.

Chapter 7: Topological Crystalline Insulator SnTe Nanoribbons

In this chapter, we are going to discuss about synthesis and characterization of the topological crystalline insulating material Tin Telluride (SnTe). Topological crystalline insulators are systems in which a band inversion that is protected by crystalline mirror symmetry gives rise to nontrivial topological surface states. The SnTe is a topological crystalline insulator. It exhibits p-type conductivity due to Sn vacancies and Te antisites, which leads to high carrier density in the bulk. Thus growth of high quality SnTe is a prerequisite for understanding the topological crystalline insulating behavior. We have grown SnTe nanoribbons using a solution method. The width of the SnTe ribbons varies from 500 nm to 2 μm. They exhibit rock salt crystal structure with a lattice parameter of 6.32 Å. The solution method that we have adapted uses low temperature, so the Sn vacancies can be controlled. The solution grown SnTe nanoribbons exhibit strong semiconducting behavior with an activation energy of 240 meV. This activation energy matches with the recently calculated band gap for SnTe with a lattice parameter of 6.32 Å. This activation energy is higher than that reported for bulk SnTe. The higher activation energy makes the thermal excitation of bulk charges very difficult on the surface. As a result, the topological surfaces will be free from the disturbance caused by the thermal excitations. This work has been submitted for publication.

7.1 Introduction

SnTe is a group IV-VI semiconductor which crystallizes in rock salt crystal structure, and is reported to have a narrow direct band gap of 0.18 eV for bulk samples [1], [2]. SnTe is an

interesting material for several applications including infrared detector [3], thermoelectric generator [4], holographic recording [5], switching device [6], and for solar cell [7]. Recently it was shown that SnTe can be classified based on topologies protected by point group symmetries of the crystal lattice. Those insulators that have nontrivial topology protected by point-group symmetries are called topological crystalline insulators (TCIs) [8]. So far concrete topological invariants are elucidated for systems possessing four-fold or six-fold rotation symmetry and also for systems with mirror symmetry. In particular, the latter case gained significant attention after the prediction that SnTe is a TCI [8]. Tanka *et al*. experimentally confirmed the TCI behavior in SnTe; they observed surface state with the double Dirac cone structure [8], [9], [10]. The SnTe is particularly unique as a platform to study valley-degenerate topological systems [11]. However, the growth of high-quality SnTe is a prerequisite to study such degeneracy effects and is also important for future devices based on TCI. The growth of high quality SnTe is a limiting issue in understanding the topological effects of SnTe. Most of the growth techniques use high temperature that results in Sn vacancies and Te substituting for Sn which leads to p-type conductivity in SnTe. In case of thin films with small thicknesses, less than 1 μm, tend to be highly granular and rough, which can significantly reduce the carrier mobility [12], [17].

We have grown two-dimensional nanoribbons of SnTe having a high surface area using a solution method to investigate the topological insulating crystal behavior. We have fabricated nanoscale devices using e-beam lithography to understand the transport properties of these nanoribbons. Solution-grown SnTe nanoribbons exhibit a large bulk band gap of 240 meV. Shen et al. have grown SnTe nanoribbons and nanosheets using vapor-liquid-solid and vapor-solid mechanisms [10]. They have observed that the SnTe nanoribbons/sheets have higher bulk carrier density similar to that observed in bulk SnTe crystals due to Sn vacancies and Te substitution for Sn. In our

synthesis, the maximum temperature used is 523 K and we have not used any catalyst for the growth, so the nanoribbons are free of chemical doping.

7.2 Experiment Methods and Materials

Nanoribbons of SnTe were synthesized using a two-step solution method. The first step of the synthesis was the growth of Te nanostructures, and the next step was to inject Sn precursor into the grown Te nanostructures to form SnTe nanoribbons. In a typical synthesis, 0.3 g of high-purity polyvinylpyrrolidone was mixed with 0.24 g of α-TeO_2 powder, followed by 20 ml of ethylene glycol along with 0.6 ml of hydrazine, and 0.6 g of sodium hydroxide as the surfactant. The resulting solution was transferred to a three-necked flask fitted with a reflux condenser and a thermometer, and de-aerated by N_2 bubbling at 15cc/s. The solution in the flask was heated to a temperature of 433 K for 2 hours, forming tellurium nanostructures and brought to room temperature. In the second step we injected the required amount of $SnCl_2$ precursor and raised the temperature to 523 K for 3 hours. The resultant solution was washed several times with ethanol, and acetone followed by centrifuge at 3000 revolutions per minute and finally dried at 373 K for 10 h in an argon environment. High quality SnTe nanoribbons are obtained only when the synthesis was carried out with TeO_2 and $SnCl_2$ as precursors for Te and Sn at 523 K. At lower temperatures, we have obtained multiple phases of Sn and Te nanoribbons and nanoparticles. We have initially carried out the synthesis with TeO_2 and SnO_2 as precursors, but obtained both Sn deficient SnTe and Te nanowires, not nanoribbons. With the use of SnO_2 as a precursor for Sn, SnTe nanoribbons could not be formed even with various growth temperatures (453 – 523) K. This low temperature synthesis method helps reduce the Sn vacancies that are generally observed in high temperature growth techniques. The morphology of the nanoribbons was analyzed using a

scanning electron microscope (SEM) (JEOL JSM-5410V); the crystal structure was determined by x-ray diffraction (XRD) (Thermo/ARL X'TRA, Cu-K_α) and transmission electron microscopy (TEM). Electrical transport properties were measured from a SnTe single nanoribbon device using a Quantum Design physical property measurement system.

7.3 Result and discussions

7.3.1 Morphology and Structure

Figure 7.1 (a) and **(b)** show the scanning electron microscopy images of SnTe nanoribbons. The dimensions of the sheets vary to some extent, but the SEM image clearly indicates the formation

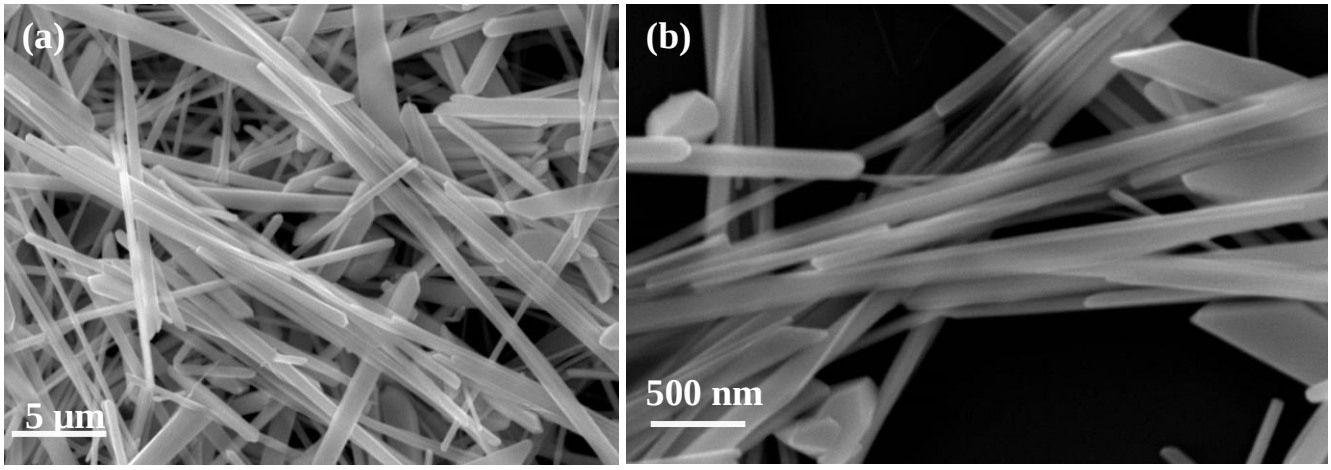

Figure 7.1: SEM images of SnTe nanostructures.

of nanoribbons with widths from 500 nm to 2 µm and lengths up to 50 µm. The width of the nanoribbons are nearly 5-8 times large compared to the CVD grown nanoribbons. **Figure 7. 2 (a)** shows the XRD pattern of SnTe nanostructures. It exhibits rock salt (cubic, space group $Fm\bar{3}m$) crystal structure with a lattice parameter of 6.32 Å. Energy dispersive X-ray (EDX) Spectroscopy analyses were carried out on nanoribbons synthesized in three different batches. A typical

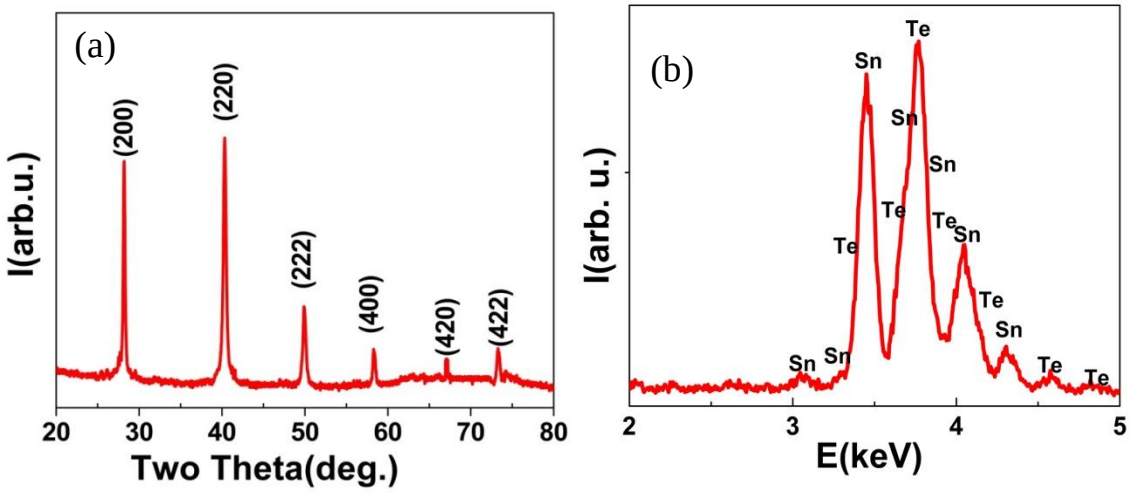

Figure 7.2: (a) The XRD pattern and (b) the EDX spectrum of SnTe ribbons.

spectrum is shown in **figure 7.2 (b**). The EDX analyses show that the SnTe nanoribbons have Sn and Te at a 1:1 ratio. High-resolution transmission electron microscopy studies of these ribbons have shown that they are single crystalline. The lattice planes observed in **figure 7.3 (a**) are (200) planes. **Figure 7.3 (b**) displays the selected area diffraction pattern of SnTe nanoribbons with beam oriented along [110] direction. The diffraction spots are indexed using the rock crystal structure. **figure 7.4** displays the TEM element mapping of the selected portion of SnTe ribbons, which

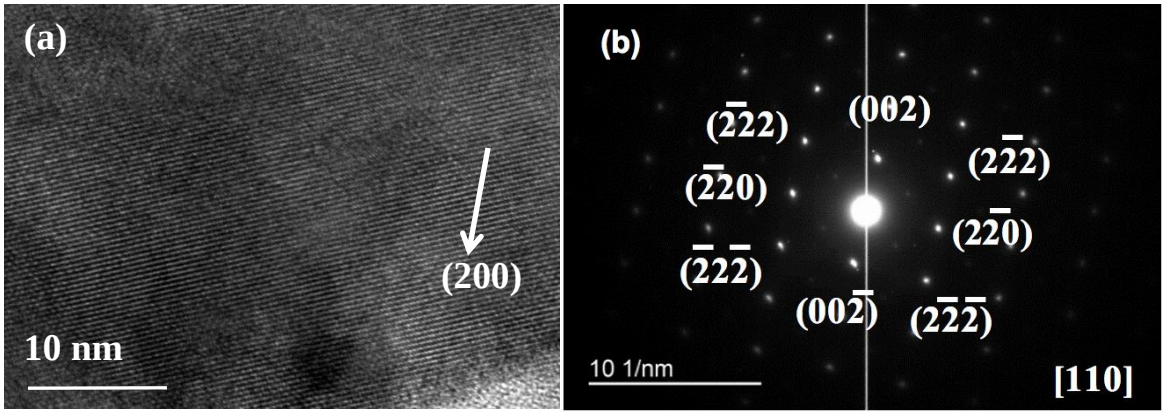

Figure 7.3: (a) High resolution TEM image displaying the lattice fringes. (b) Selected area electron diffraction of SnTe single crystalline ribbons.

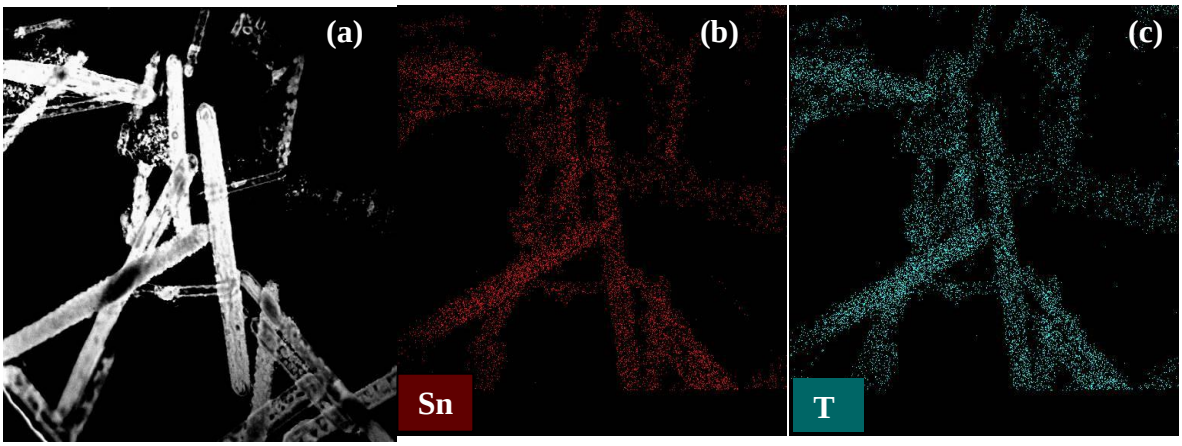

Figure 7.4: (a) TEM image of SnTe sheets (b) Sn (c) Te.

conforms the uniform distribution of Sn and Te elements everywhere on the ribbons representing Sn as a red and Te as blue colors.

7.3.2 Transport Properties

Nanoscale devices using ribbons were fabricated using the standard electron beam lithography technique to understand the electrical transport properties. We have deposited 150 nm of titanium

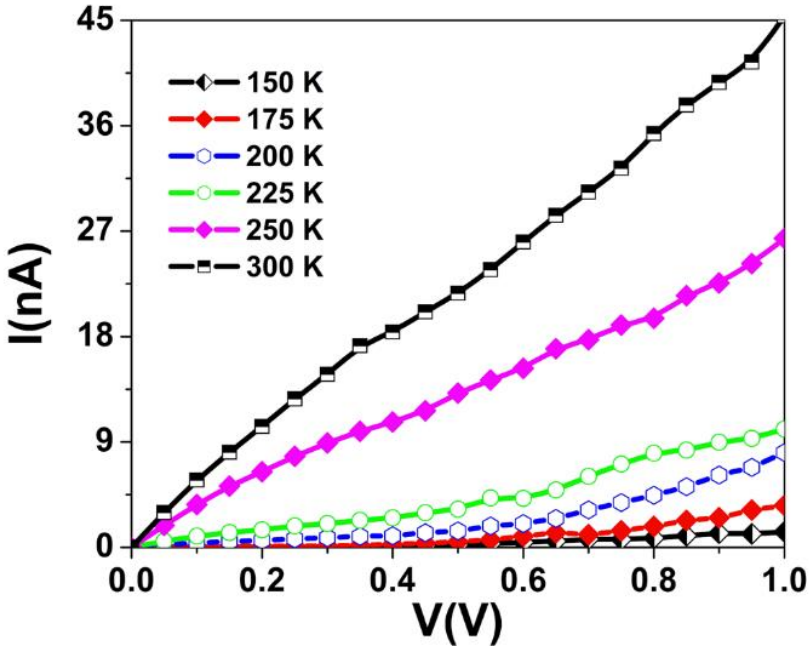

Figure 7.5: The Current-voltage characteristics of SnTe nanoribbon device.

(10 nm) and gold (140 nm) as electrodes using an ultra-high vacuum (base pressure $1x10^{-9}$ torr) evaporation chamber. Transport properties have shown in **figure 7.5**. and **figure 7.6.** Typical current-voltage (I-V) characteristics of the single nanoribbon device at different temperatures is shown in **figure 7.5** We have measured the I-V characteristics from room temperature to 150 K. There is a 97% change in the resistivity as the temperature is lowered from room temperature to 150 K at 1 V bias voltage. The nonlinear increase in resistivity with the decrease in temperature demonstrates that the SnTe nanoribbons display strong semiconducting behavior. **Figure 7.6 (a)** shows the temperature dependence of resistance from room temperature to 125 K measured with increasing temperature of the sample. The exponential decay shown in the curve illustrates the semiconducting behavior of SnTe ribbons. Resistance of a semiconductor is related to the temperature.

$$ln(R) = ln(R_0 + E_a/K_B T) \qquad 7.1$$

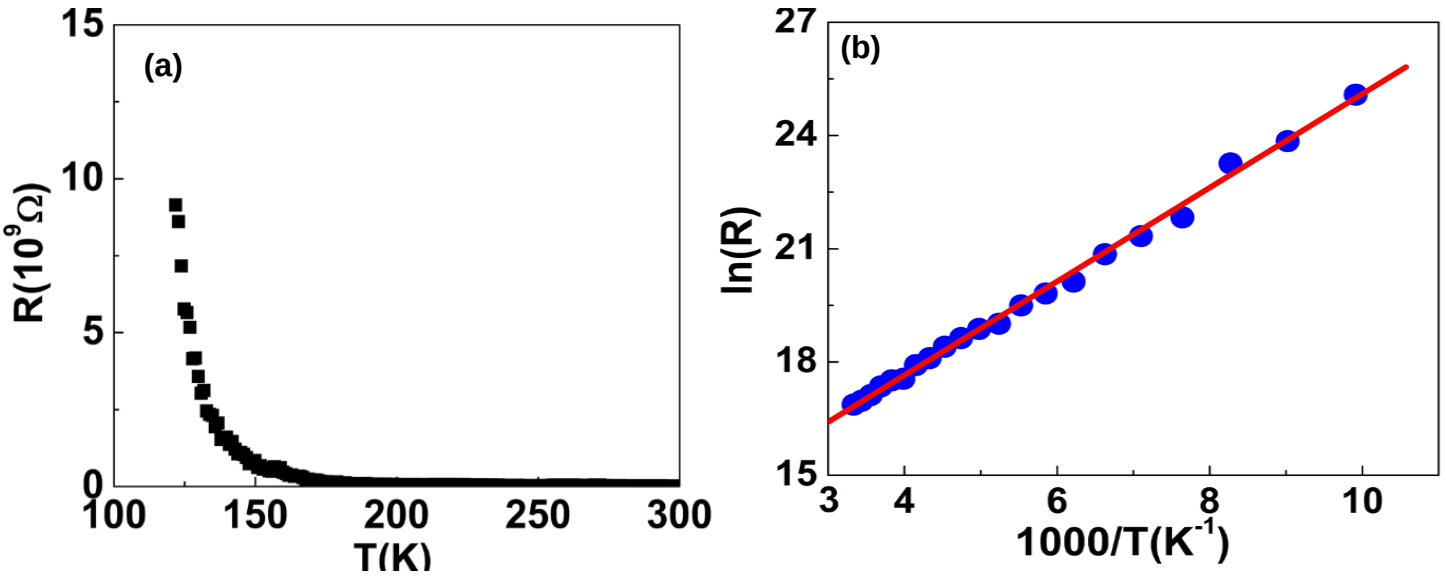

Figure 7.6: (a) Resistance as a function of temperature of a SnTe nanoribbon device. (b) The plot of lnR vs. 1/T displaying the linear characteristic of a semiconductor. The blue circles are experimental data and the line is a fit to the data.

Where, R represents the resistance at temperature T (K), R_0 represents resistance at 0 K, and K_B is the Boltzmann constant [19]. **Figure 7.6 (b**) is a plot of ln(R) vs 1000/T, which shows the expected linear behavior of a semiconductor. Activation energy E_a can be calculated from the well fitted experimental data in **figure 7.6 (b)** and the calculated activation energy is 240 meV. The activation energy value obtained matches with the calculated band gap value for SnTe with a lattice parameter 6.32 Å [8]. Hsieh et al. calculated the band gap of SnTe as a function of lattice parameter, the band gap decreases with decrease in lattice parameter [8]. This E_a value is much greater than the value observed in common topological insulators like Bi_2Te_3 and Sn-doped Bi_2Te_2Se having activation energy to be 2 meV and 125 meV respectively [20, 21]. The higher activation energy makes the thermal excitation of bulk charges very difficult on the surface of the topological crystalline insulator. As a result, the topological surfaces are free from the disturbance caused by the thermal excitations. Thus the SnTe nanoribbons grown using the solution method are very promising candidates for understanding the topological crystalline insulator behavior.

7.4 Conclusions

Single crystal SnTe nanoribbons have synthesized using solution chemistry at relatively low temperature. They exhibit rock salt cubic crystal structure. Inversion of band structure of rock salt possess mirror symmetry. Hence, SnTe are topological crystalline insulator which has no Z_2 topological order. Electric transport has been analyzed by making a field effect transistor FET of SnTe nanoribbons using e-beam lithography. Also the semiconducting behavior with an activation energy of 240 meV has been calculated.

Bibliography

[1] Y. W. Tung, and M. L. Cohen, "Relativistic Band Structure and Electronic Properties of SnTe, GeTe, and PbTe," Phys. Rev., Vol. 180, Iss. 3, PP. 823-826, 1969.

[2] J. Ning, K. Men, G. Xiao, B. Zou, L. Wang, Q. Dai, B. Liu, and G. Zou, "Synthesis of narrow band gap SnTe nanocrystals: nanoparticles and single crystal nanowires *via* oriented attachment," Cryst. Eng. Comn., Vol. 12, PP. 4275-4279, Aug. 2010.

[3] C. Boschetti, I. N. Banderia, H. Closs, A. Y. Ueta, P. H. O. Rappl, P. Motisuke, E. Abramof, "Molecular beam epitaxial growth of PbTe and PbSnTe on Si (1 0 0) substrates for heterojunction infrared detectors," Infrared Phys. Techn., Vol. 42, Iss. 2, PP. 91-99, Apr. 2001.

[4] G. Tan, L. –D. Zhao, F. Shi, J. W. Doak, S.- H. Lo, H. Sun, C. Wolverton, V. P Dravid, C. Uher, and M. G. Kanatzidis, "High Thermoelectric Performance of p-Type SnTe via a Synergistic Band Engineering and Nanostructuring Approach," J. Am. Chem. Soc., Vol. 136 (19), PP. 7006-7017, May 2014.

[5] R. K. Saini, R. Kumar, and G. Jain, "Optical studies of $SnTe_xSe_{1-x}$ sintered films," Optl. Mater., Vol. 32, Iss. 2, PP. 297- 301, Dec. 2009.

[6] K. A. Campbell, C. M. Anderson, "Phase-change memory devices with stacked Ge-chalcogenide/Sn-chalcogenide layers," Micro J., Vol. 38, Iss. 1, PP. 52-59, Jan. 2007.

[7] M. C. Beard, J. M. Luther, and A. J. Nozik, "The promise and challenge of nanostructured solar cells," Nat. Nanotechnol., Vol. 9, PP. 951-954, Dec. 2014.

[8] T. H. Hesieh, H. Lin, J. Liu, W. Duan, A. Bansil, and L. Fu, "Topological Crystalline

Insulatos in the SnTe Material Class," Nat. Commun., Vol. 3, Nom. 982, Jul. 2012.

[9] Y. Tanaka, T. Sato, K. Nakayama, S. Souma, T. Takahashi, Z. Ren, M. Novak, K. Segawa, and Y. Ando, "Tunability of the k-Space Location of the Dirac Cones in the Topological Crystalline Insulator $Pb_{1-x}Sn_xTe$," Phys. Rev. B, 87, Iss. 15, PP. 1-5 Apr. 2013.

[10] J. Shen, Y. Jung, A. S. Disa, F. J. Walker, C. H. Ahn, J. J. Cha, "Synthesis of SnTe Nanoplates with {100} and {111} Surfaces," Nano Lett., Vol. 14 (7), PP. 4183-4188, Jun. 2014.

[11] B. A. Assaf, F. Katmis, P. Wei, B. Satpati, Z. Zhang, S. P. Bennett,V. G. Harris, J. S. Moodera, and D. Heiman, "Quantum coherent transport in SnTe topological crystalline insulator thin films," Appl. Phys. Lett., Vol 105, 102108, Sep. 2014.

[12] A.P. Bakhtinov, V.N. Vodop'yanov, V.I. Ivanov, Z.K. Kovalyuk, and O.S. Lytvyn, Phys. of the Sol. Stat., Vol. 55, PP.181-195, Jan. 2013.

[13] A. Ishida, T. Yamada, T. Tsuchiya, Y. Inoue, S. Takaoka, and T. Kita, Appl. Phys. Lett., Vol. 95, PP. 122106, Sep. 2009.

[14] S. O. Ferreira, E. Abramof, P. H. O. Rappl, A.Y. Ueta, H. Closs, C. Boschetti, P. Motisuke, and I.N. Bandeira, J. Appl. Phys., Vol. 84, PP. 3650, Jul. 1998.

[15] E. Abramof, S.O. Ferreira, P.H.O. Rappl, H. Closs, and I.N. Bandeira, J. Appl. Phys., Vol. 82, PP. 2405-2410, Sep. 1997.

[16] U. A. Mengui, E. Abramof, P. H. O. Rappl, and A.Y. Ueta, Braz. J. Phys., Vol. 26, PP. 324-327, Jun. 2006.

[17] A. A. Taskin, F. Yang, S. Sasaki, K. Segawa, and Y. Ando, Phys. Rev. B, Vol. 89, 121302, Mar. 2014.